ADVANCED MULTIPLEXING TECHNIQUES IN SINGLE MOLECULE LOCALISATION MICROSCOPY

Dissertation
for the award of the degree
"Doctor of Philosophy" Ph.D.
Division of Mathematics and Natural Sciences
of the Georg-August-Universität Göttingen

within the doctoral program
Physics
of the Georg-August University School of Science (GAUSS)

submitted by
Nazar Oleksiievets
from Ternopil, Ukraine

Göttingen, 2021

THESIS ADVISORY COMMITTEE:
Prof. Dr. Jörg Enderlein
Third Institute of Physics – Biophysics
Georg-August-University, Göttingen

Prof. Dr. Marcus Müller
Institute for Theoretical Physics
Georg-August-University, Göttingen

Prof. Dr. Burkhard Geil
Institute of Physical Chemistry
Georg-August-University, Göttingen

MEMBERS OF THE EXAMINATION BOARD:
Prof. Dr. Jörg Enderlein **(Referee 1)**
Third Institute of Physics – Biophysics
Georg-August-University, Göttingen

Prof. Dr. Silvio Rizzoli **(Referee 2)**
Institute for Neuro-and Sensory Physiology
University Medical Center Göttingen

Prof. Dr. Marcus Müller
Institute for Theoretical Physics
Georg-August-University, Göttingen

Prof. Dr. Alexander Egner
Laser-Laboratorium Göttingen e.V.

Prof. Dr. Timo Betz
Third Institute of Physics – Biophysics
Georg-August-University, Göttingen

Prof. Dr. Stefan Luther
Max Planck Institute for Dynamics
and Self-Organization, Göttingen

Date of Oral Examination : 17.05.2021

ACKNOWLEDGMENTS

First, I want to thank my supervisor, Prof. Jörg Enderlein, who gave me an opportunity to work on this project, even it was not an initial plan. Thank you for sharing your knowledge, for giving me a lot of freedom in my research, and for always being a kind and supportive boss. I could not have hoped for a better supervisor.

I am very grateful to my colleague, co-author and friend, Roman Tsukanov, whose expertise and feedback brought my work to a higher level. I would like to express my deep gratitude to Oleksii Nevskyi, Anna Chizhik and Alexey Chizhik, my colleagues and friends, for their time and advices inside and outside the lab throughout my whole PhD. I thank my office mates Akshita and Hongje for great working atmosphere. I also thank Steffen, Aditya, Christoph, Tao, Arindam, Soheil, Sebastian, Narain, Daja, Niels and Subhabrata for professional and non-professional discussions and great time that we spent together. I want to thank in particular Ingo Gregor for sharing his expertise and always having a solution for every problem.

I thank all people I had the chance to collaborate with, especially Shama Sograte-Idrissi, Nikolaos Mougios and Felipe Opazo. I enjoyed our project and I am thankful for the chance to learn a bit about biology. Special thanks to Yelena Sargsyan and Sven Thoms for providing great samples and realizing excellent project.

A big thank to Thomas Geiling for his assistance with IT issues, Regina Wunderlich, Silke Bertram and Ursula Hahn-Woergoetter for their help with bureaucratic matters. I would also like to thank Dieter Hille and his team from the mechanical workshop for creating various parts for the optical setup.

I want to thank SFB 803 for the funding of my work and for organising great winter schools, that gave me more knowledge about lipid membranes. I would also like to thank Dana Sachs for always being very helpful and approachable for questions. I thank Prof. Marcus Müller and Prof. Burkhard Geil for their input and their time to discuss my work in the thesis committee meetings.

Finally, I would like to thank my family for their sympathetic ear and encouragement throughout my study. Especially my wife, Viktoriia, who are always there for me and provided cheerful distractions to rest my mind outside of my work. I am extremely grateful to my father, who passed away this year, for many hours spent together solving math exercises in the childhood, and for always supporting me and my life decisions.

Thank you all very much,
Nazar Oleksiievets
Gottingen, 2021

CONTENTS

Abstract ix

1 INTRODUCTION 1
- 1.1 Fluorescence microscopy 1
- 1.2 Fluorescence lifetime imaging 7
  - 1.2.1 Time correlated single photon counting 7
  - 1.2.2 Frequency-domain lifetime imaging 10
- 1.3 Super-resolution fluorescence microscopy 12
  - 1.3.1 Resolution limit of optical microscopy 12
  - 1.3.2 Enhanced resolution microscopy 13
  - 1.3.3 Super-resolution microscopy 16
- 1.4 Multiplexed single-molecule localisation microscopy 20
  - 1.4.1 Spectral splitting 20
  - 1.4.2 Exchange-based multiplexing 21
- 1.5 Axial localization of fluorophores 24
  - 1.5.1 Metal-induced energy transfer 26

2 NANOBODY DETECTION OF STANDARD FLUORESCENT PROTEINS ENABLES MULTI-TARGET DNA-PAINT WITH HIGH RESOLUTION AND MINIMAL DISPLACEMENT ERRORS 29
- 2.1 Multi-target DNA-PAINT 29

3 WIDE-FIELD FLUORESCENCE LIFETIME IMAGING OF SINGLE MOLECULES 53
- 3.1 Wide-field fluorescence lifetime imaging of single molecules 53

4 FLUORESCENCE LIFETIME-BASED DNA-PAINT FOR MULTIPLEXED SUPER-RESOLUTION IMAGING OF CELLS 79
- 4.1 Abstract 79
- 4.2 Introduction 79
- 4.3 Methods 81
  - 4.3.1 Preparation of COS-7 cells 81
  - 4.3.2 Preparation of HeLa cells 81
  - 4.3.3 Immunostaining 82
  - 4.3.4 Screening of fluorophores in the green spectral range suitable for FL-PAINT 82
  - 4.3.5 Data acquisition 83
  - 4.3.6 Data analysis 84
- 4.4 Results 85
  - 4.4.1 Wide-field FL-PAINT 85
  - 4.4.2 WF-FL-PAINT validation with Exchange-PAINT 89
  - 4.4.3 CLSM-based FL-PAINT 89
- 4.5 Conclusions 90
- 4.6 Appendix 92

5 DISCUSSION AND OUTLOOK 103

6 OTHER CONTRIBUTIONS 107
6.1 Confocal Laser-Scanning Fluorescence-Lifetime SMLM 107
6.2 Fluorescent Silicate Nanosheets 110

BIBLIOGRAPHY 113

LIST OF FIGURES

Figure 1.1 Jablonski diagram 2
Figure 1.2 The absorption and fluorescence emission spectra 3
Figure 1.3 Schematics of two types of fluorescence microscopes 6
Figure 1.4 TCSPC principle 9
Figure 1.5 Illustration of frequency-domain fluorescence lifetime measurement 10
Figure 1.6 Resolution of an optical microscope 13
Figure 1.7 Resolution enhancement by structured illumination 15
Figure 1.8 The underlying principle of STED microscopy 17
Figure 1.9 Principle of single molecule localization-based super-resolution microscopy 18
Figure 1.10 DNA-PAINT concept 19
Figure 1.11 Schematic of sequential Exchange-PAINT 23
Figure 1.12 Metal-induced energy transfer 26
Figure 4.1 Multiplexed FL-PAINT imaging of a fixed cell 86
Figure 4.2 Two- and three-target FL-PAINT of HeLa cells using wide-field FLIM 88
Figure 4.3 2D and 3D FL-PAINT using a CLSM 90
Figure 4.4 Experimental FLIM techniques compatible with FL-PAINT 94
Figure 4.5 FL-PAINT images of HeLa and COS-7 cells 97
Figure 4.6 Diffraction-limited wide-field imaging 98
Figure 4.7 Pattern matching analysis approach 100
Figure 4.8 Effect of emission photon detection count-rate on lifetime accuracy and localization precision 101
Figure 6.1 Confocal laser-scanning fluorescence-lifetime SMLM 109
Figure 6.2 Frequency-domain fluorescence lifetime imaging of near-infrared fluorescent silicate nanosheets 111

ACRONYMS

CLSM	Confocal Laser-Scanning Microscopy
DNA-PAINT	DNA points accumulation for imaging in nanoscale topography
FD-FLIM	Frequency-Domain Fluorescence Lifetime Imaging Microscopy

FLIM	Fluorescence Lifetime Imaging Microscopy
FL-PAINT	Fluorescence Lifetime PAINT
fm-SMLM	Frequency-Based Single-Molecule Localisation Microscopy
FRET	Förster Resonance Energy Transfer
GIET	Graphene-Induced Energy Transfer
HILO	Highly Inclined Thin Illumination
iPALM	Interferometric Photoactivated Localization Microscopy
ISM	Image Scanning Microscopy
masS3TORM	Multiplexed Automated Serial Staining Stochastic Optical Reconstruction Microscopy
MCPs	Micro-Channel Plates
MIET	Metal-Induced Energy Transfer
PALM	Photoactivated Localization Microscopy
p-MINFLUX	Pulsed-Interleaved MINFLUX
PAINT	Points Accumulation for Imaging in Nanoscale Topography
QDs	Quantum dots
SAF	Super-critical Angle Fluorescence
SIM	Structured Illumination Microscopy
SMLM	Single-Molecule Localisation Microscopy
smMIET	Single-Molecule Metal-Induced Energy Transfer
SPAD	Single-Photon Avalanche Diode
STED	Stimulated Emission Depletion
STORM	Stochastic Optical Reconstruction Microscopy
TCSPC	Time-Correlated Single-Photon Counting
TIR	Total Internal Reflection
TIRFM	Total Internal Reflection Microscopy
va-TIRFM	Variable Angle Total Internal Reflection Microscopy

ABSTRACT

Fluorescence microscopy has become a powerful and important bioimaging tool in modern science [1]. It is currently the most commonly used method for cellular imaging. The high sensitivity of fluorescence detection together with the high specificity of labelling allows for studying living and fixed cells both for resolving structure as well as dynamics. The spatial resolution of a fluorescence microscope is limited by the diffraction of light, making details smaller than roughly 200 nm unresolvable. However, many cellular structures are much smaller than this limit, being only a few dozen nanometers in size. Huge efforts have been invested into overcoming this limit. Eventually, it was finally broken with the invention of two super-resolution microscopy techniques: Stimulated Emission Depletion (STED) microscopy [2], and Single-Molecule Localization Microscopy (SMLM) [3] [4]. The first one exploits the phenomenon of stimulated emission of fluorophores, while the second relies on single-molecule imaging and the on/off switching behavior of fluorophores.

The field of super-resolution is growing rapidly, having made huge progress over the last decade. However, all methods so far have to find a compromise between spatial resolution and imaging speed. The acquisition speed of the method is important for high-throughput imaging, which aims towards the data collection efficiency optimisation [5]. Another important aspect of a super-resolution method is its technical complexity which is characterized by difficulty of alignment and maintenance required to keep the system in optimal function. Finally, the required equipment cost is a non-negligible aspect.

An important aspect of many microscopy modalities is their capability of observing many different structures and molecular species simultaneously. This so-called multi-target imaging provides a deeper understanding of the structural organization of cells and the interaction between different molecular species and organelles. There are many approaches to multi-target imaging, as I will discuss in detail in the next chapters. This thesis presents several novel techniques for multiplexed imaging, with the main focus on the super-resolution technique of DNA-points accumulation for imaging in nanoscale topography (DNA-PAINT) [6]. In Chapter 2, I demonstrate multiplexed imaging by using three different single-domain antibodies. These camelid single-domain antibodies are also called nanobodies. They have a three times smaller size than conventional antibodies, therefore reducing the distance between the target site and the fluorophore (also

known as "linkage error"). The used nanobodies have a high and specific binding affinity against three common fluorescent proteins: GFP, BFP and RFP. This allows me to use conventional fluorescent protein fusion for labelling cellular structures of interest, and then to use fluorescently labelled nanobodies as imager molecules in PAINT. For being able to image the three fusion-protein targets in the same cellular sample, I developed and optimized a versatile computer-controlled microfluidic setup designed particularly for multiplexed DNA-PAINT. As a proof of principle, I performed multiplexed super-resolution imaging of mitochondria, the Golgi apparatus, and chromatin inside COS-7 cells. In Chapter 3, I introduce a novel wide-field Time-Correlated Single Photon Counting (TCSPC) camera, that was successfully used for Fluorescence Lifetime Imaging (FLIM) with single-molecule sensitivity. I performed single-molecule FLIM of fluorophores of different types but within the same red spectral region, and then used the fluorescence lifetime for successfully distinguishing between them. As an additional application of Fluorescence-Lifetime Single-Molecule Localization Microscopy (FL-SMLM), I used FL-SMLM for single-molecule metal-induced energy transfer (smMIET) imaging which is a first step towards three-dimensional single-molecule localization microscopy (SMLM) with isotropic nanometer resolution. In Chapter 4, I develop a new technique for multiplexed DNA-PAINT imaging, based on the combination of DNA-PAINT with FLIM (FL-PAINT). The lifetime information allows for lifetime-based disentanglement of different targets in the same spectral range, completely avoiding the chromatic aberration, which is usually a big challenge for multi-target super-resolution microscopy with labels of different colour. Furthermore, FL-PAINT does not require solution exchange during image acquisition. I demonstrate FL-PAINT multiplexing with imaging two targets in COS-7 and HeLa cell. For realizing FL-SMLM, I employed two different FLIM techniques: wide-field FLIM, and confocal scanning laser microscopy (CSLM). With these techniques, I expand the toolbox of multiplexing in fluorescence microscopy and tackle the challenge of lengthy acquisition time, which is a main drawback of SMLM. Finally, Chapter 5 summarizes all findings and concludes the thesis.

1

INTRODUCTION

In this section, I provide the theoretical background for my thesis. I start with a general introduction into the basics of fluorescence and then explain the physics behind it. In Chapter 1.2, I introduce fluorescence lifetime imaging and present the two main approaches how to experimentally realize this: frequency-domain and time-domain Fluorescence Lifetime Imaging Microscopy (FLIM). Following this, I will discuss the resolution limit of classical optical microscope and will present an overview on super-resolution microscopy which overcomes this resolution limit. In the Chapter 1.3, I will specifically focus on Single-Molecule Localisation Microscopy (SMLM), and especially on DNA points accumulation for imaging in nanoscale topography (DNA-PAINT). In Chapter 1.4, I take a detailed look at different multiplexing approaches based for SMLM imaging. Finally, I provide an overview of SMLM methods for imaging in three dimensions and will introduce Metal-Induced Energy Transfer (MIET) imaging.

1.1 FLUORESCENCE MICROSCOPY

Fluorescence is the process of light emission from the substance that have absorbed light. Light is transmitted only in quantized energy units called photons. From a quantum mechanical point-of-view, a fluorescent emitter can be in three dimensions as an energetic multi-state system. Starting from its energetic ground state, such a system can be excited into a state of higher energy by the absorption of a photon. After a short time (typically a few nanoseconds), the system returns into its ground state, while the energy difference between excited and ground states is released in form of a fluorescent photon (radiative transition). Alternatively, the energy can dissipate into heat or can be transferred into another excited state without photon emission (non-radiative transition). This process can be visualized using a Jablonski diagram, see Figure 1.1.

The transition from the singlet ground state S0 to the excited state requires the absorption of a photon with an energy equal to the energy difference between these two states. However, the electronic states have additional vibrational sub-states, which allow for multiple transitions with slightly different energies. A fluorophore is excited to a higher vibrational level of either S1 or S2. Following this, molecules rapidly relax to the lowest vibrational level of S1. This process is called "internal

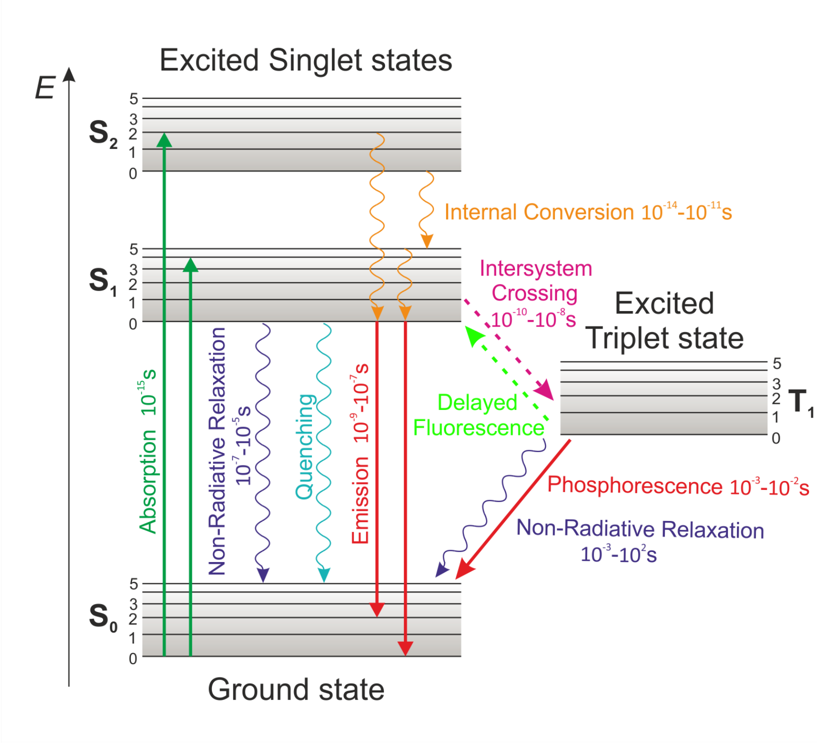

Figure 1.1: Jablonski diagram illustrating the energy levels of a typical fluorophore and the transitions between them. Additionally, the time-scales of these transitions are depicted.

conversion" and usually is completed prior to the emission. Because of this rapid relaxation, fluorescence emission generally results from the lowest energy vibrational state of S1. The consequence of this is that emission spectra are usually independent of the excitation wavelength, known as Kasha's rule.

Fluorescence emission typically occurs to a higher vibrational ground state, which is the reason for the vibrational structure (extra peaks) in the emission spectrum of some fluorophores. Interestingly, the emission spectra are typically a mirror image of the absorption spectra, see Figure 1.2. This occurs because electronic excitation does not alter the nuclear geometry and the spacing of excited state vibrational levels is similar to the ground state.

Rapid decay to the lowest vibrational level of S1 and further fluorescence emission to higher vibrational levels of S0 result in significant excitation energy dissipation. This means that fluorescence emission energy is typically lower than excitation energy. Hence, fluorescence occurs at lower energies or longer wavelength, see Figure 1.2. The shift between the two spectra is known as the Stokes shift.

Another possible scenario is a spin conversion to the first triplet state, which is highly relevant for fluorescence microscopy. This conversion of S1 to T1 is called "intersystem crossing". The low probability of this process arises from the fact that this transition is forbidden. In this state, the molecule does not fluoresce and is thus not detectable. The transition into and out of the triplet state leads to a visible blinking of a fluorophore, a phenomenon that is exploited in certain super-resolution microscopy methods (see Chapter 1.3). The slow radiative relaxation of the triplet state back to the ground state can be also connected with the emission of a photon, which is then called phosphorescence. This is also a very slow, forbidden transition. Another possibility is "delayed fluorescence", the transition back to the first excited singlet level.

Other non-radiative transitions from excited state to ground state exist and account for the majority of molecules not exhibiting fluorescence or phosphorescence behavior. One process is a quenching, which can occur by different mechanisms. Collisional quenching occurs when the fluorophore in excited state is deactivated through a contact with some other molecule, which is called the quencher. In this process molecules are not chemically altered. Examples of quencher molecules include oxygen, halogens, and amines.

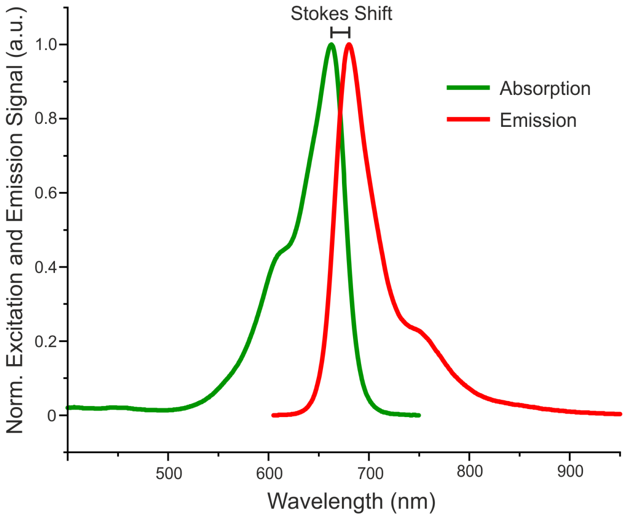

Figure 1.2: The absorption and fluorescence emission spectra of the common organic fluorophore Atto 655. The absorption spectrum is shown in green and the emission spectrum in red. The wavelength difference between absorption and emission maxima is called Stokes shift, as depicted in the plot. Data provided by the manufacturer ATTO-TEC.

Besides the fluorescence spectrum, other important parameters such as the fluorescence quantum yield or the fluorescence lifetime are important for selecting the optimum dye for microscopic and spectroscopic applications. The fluorescence quantum yield Φ of a fluorescent molecule is defined as the ratio of the number of emitted fluorescence photons to the number of absorbed photons. Mathematically, it is defined by:

$$\Phi = \frac{k_r}{k_r + k_{nr}} \tag{1.1}$$

where k_r and k_{nr} are the radiative and non-radiative decay rate constants, respectively. Non-radiative processes include internal conversion, quenching, or intersystem crossing. Ideally, one would like to work with fluorophores having a quantum yield value of Φ = 1, but most fluorophores show values between 0.2 and 1.0. A second important parameter is the fluorescence lifetime τ of a fluorophore which is defined as the average time a fluorophore spends in its excited singlet state S_1, and which is given by:

$$\tau = \frac{1}{k_r + k_{nr}} \tag{1.2}$$

The fluorescent lifetime can be measured by exciting the molecule with a short laser pulse. This results in initial population n_0 of fluorophores in the excited state. The population $n(t)$ in the excited state decays with rate $k_r + k_{nr}$, described by the equation:

$$\frac{dn(t)}{dt} = -(k_r + k_{nr})n(t) \tag{1.3}$$

The solution of this equation is given by an exponential decay of the excited state population:

$$n(t) = n_0 e^{-\frac{t}{\tau}} \tag{1.4}$$

Since the momentous fluorescence intensity $I(t)$ is proportional to the number of excited fluorophores $n(t)$, this leads also to a monoexponential decay of the observable fluorescence intensity with decay time τ, similar to a radioactive decay:

$$I(t) = I_0 e^{-\frac{t}{\tau}} \tag{1.5}$$

where I_0 is the intensity at time 0.

The lifetime of a fluorescent molecule can be sensitive to the local environment such as local electric charge, solvent pH, or viscosity. Hence, the fluorescence lifetime can serve as a sensor for studying local properties in various chemical and biochemical systems.

The two most commonly used types of fluorophores are organic dyes and fluorescent proteins. Organic dyes have a size of about 1 nm and are in general attached to the target of interest via immunolabeling. In this method, the fluorophore is covalently bound to an antibody that specifically binds to a target antigen with high affinity, or to another primary antibody introduced during the labelling procedure. Fluorescent proteins are incorporated via transfection, where the genome of a cell is altered by introducing a plasmid encoding for the fluorescent protein, leading to the expression of the protein fused to a structure of interest. Fluorescent proteins are larger than organic dyes, with a size of about 3 nm to 5 nm. In the last 20 years, semiconductor quantum dots have been introduced as alternative markers (luminescent emitters) for bio-imaging. Quantum dots are comparatively large, with sizes varying between 10 nm and 30 nm, but are significantly brighter and more photostable than conventional dyes or fluorescent proteins. Like organic dyes, they are attached to target structures via immunolabeling. Many types of quantum dots exhibit pronounced blinking, which is however not related to triplet state dynamics, but to different mechanisms of electron charge transfer.

The two major imaging methods in fluorescence microscopy are wide-field and confocal microscopies. In a wide-field epi-fluorescence microscope (Figure 1.3 A), emission is collected by the same objective that is used for the excitation light. This requires the usage of a so-called dichroic mirror that transmits fluorescence to the detector, while reflecting the excitation light towards the sample. These microscopes are widely used in bio-imaging. The main advantages of this type of microscopes are high speed of image acquisition, ease of use, cost-efficiency, and easy maintenance. The major drawback of wide-field fluorescence microscopy is relatively high background level, due to the fact that the microscope collects the light from all optical planes, leading to a significant contribution of out-of-focus emission to an image. Moreover, a wide-field microscope does not easily allow for recording three-dimensional images of a sample.

In a confocal microscope (see Figure 1.3 B), the laser excitation light is tightly focused into a diffraction-limited spot in the focal plane, in contrast to the homogeneous wide-field illumination of the sample in a wide-field microscope. The emitted and collected light passes through the dichroic mirror and is focused through a circular pinhole for blocking out-of-focus light. After the pinhole, the light is re-focused onto an avalanche photo-diode. Confocal microscopy rejects out-of-focus light, thereby improving the signal-to-noise ratio of the images. By scanning the sample with the focused laser beam in three dimensions, a 3D image of a sample can be obtained. The scanning procedure can be done by moving the sample using a piezo-mechanical translational stage while keeping the position of the excitation fixed, or by using a galvo scanner for rapidly moving the laser focus. Thus, confocal microscopy improves the signal-to-noise ratio and enables the recording three-dimensional images of specimens. However, due to its sequential scanning character, it is rather slow (as compared to wide-field microscopy), and it is technically far more complex than wide-field microscope.

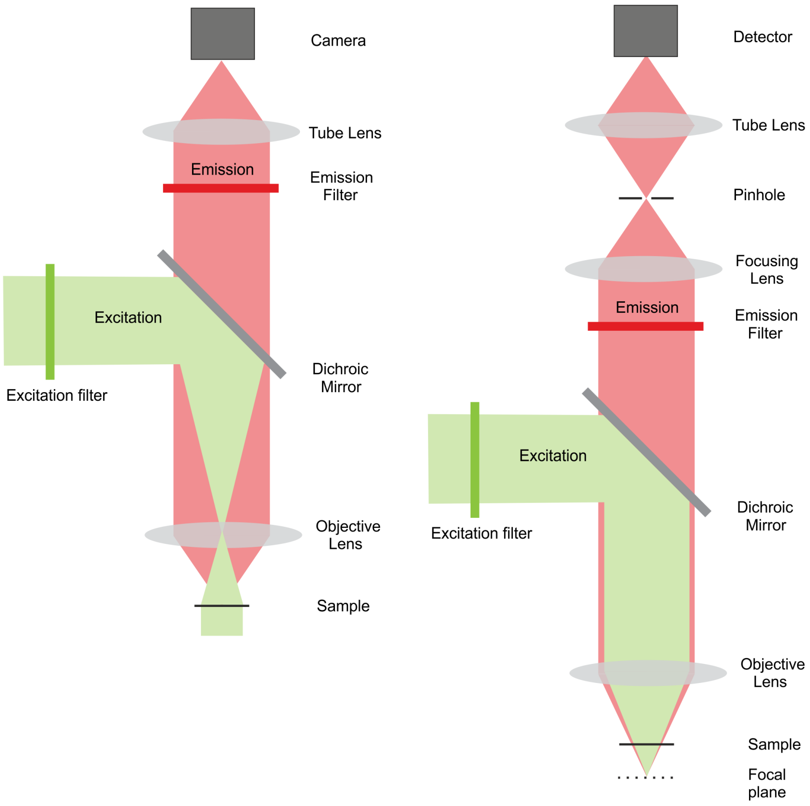

Figure 1.3: Schematics of two types of fluorescence microscopes. Left panel shows a wide-field epi-fluorescence microscope. Excitation light is shown in green and fluorescence emission in red. The right panel depicts a confocal microscope.

1.2 FLUORESCENCE LIFETIME IMAGING

Fluorescence microscopy has revolutionised our way to investigate biological processes. One of its extensions is Fluorescence Lifetime Imaging Microscopy (FLIM) which has become an important microscopy technique in medicine and biology [7][8]. In addition to a conventional intensity image, it provides additional lifetime information. The two most important applications of FLIM are distinguishing between different fluorophores with similar emission spectra based on their fluorescence lifetime [9], and Förster Resonance Energy Transfer imaging [10] [11]. One of the biggest technical challenges of FLIM is to achieve high image acquisition speed without compromising sensitivity. There are two fundamentally different technical approaches to FLIM. The first technique is Time-Correlated Single-Photon Counting (TCSPC) [12]. Mostly, it is used in tandem with Confocal Laser-Scanning Microscopy (CLSM), where one scans a field of view to create an image. During the scan, both intensity and fluorescence lifetime are measured. This assures high sensitivity, but for the prize of reduced image acquisition speed. The second approach to do FLIM is based on camera-based phase-fluorometry, which allows fast image acquisition, but for the prize of tremendously reduced sensitivity [13][14]. For example, wide-field phase-fluorometry is much too insensitive for being capable for single-molecule detection. Other available FLIM techniques are based on electro-optical modulators [15], electron Micro-Channel Plates (MCPs) [16], or wide-field time-gated Single-Photon Avalanche Diode (SPAD) arrays [17]. However, these methods are usually too insensitive for actual single-molecule applications or have very small field of view, with few exceptions like a recent application of Pockels cells for lifetime imaging [15]

1.2.1 *Time correlated single photon counting*

The direct recording of the fast fluorescence decay is very challenging, due to the fact that fast processes on the order of nanoseconds require detectors and electronics with high temporal resolution. A resolution in the order of picoseconds is not reachable with traditional photodiodes and amplifiers. The solution to this problem is Time-Correlated Single-Photon Counting (TCSPC), which is based on the ability of detecting and counting single photons. In TCSPC, the sample is illuminated with a high-repetition short-pulse laser, and the excited fluorescence is measured via single-photon counting [12]. This extends the observation over multiple excitation and emission cycles and the decay can be reconstructed from all single photon events collected over many cycles (see Figure 1.4). The detector registers the arrival times of single photons with respect to the exciting laser pulses (red dots in

Figure 1.4). By recording a large number of these single photon events and histogramming the arrival times, a fluorescence decay histogram is built up (bottom of Figure 1.4). The exponential decay of this histogram over time then yields the characteristic fluorescence decay time.

A typical TCSPC setup consists of a pulsed laser and a single-photon detector which both are interfaced to a fast electronics. The excitation source provides the reference times given by the light pulses. The detector generates an electrical pulse for each photon that it detects. In the TCSPC electronics, both signals are processed and photon arrival times are eventually stored in a computer. The photon flux on the detector has to be orders of magnitude smaller than the repetition rate of the laser for preventing any so-called pile-up effects [18]. The details of TCSPC instrumentation and operation can be found in Chapters 3 and 4, as well as in ref. [19].

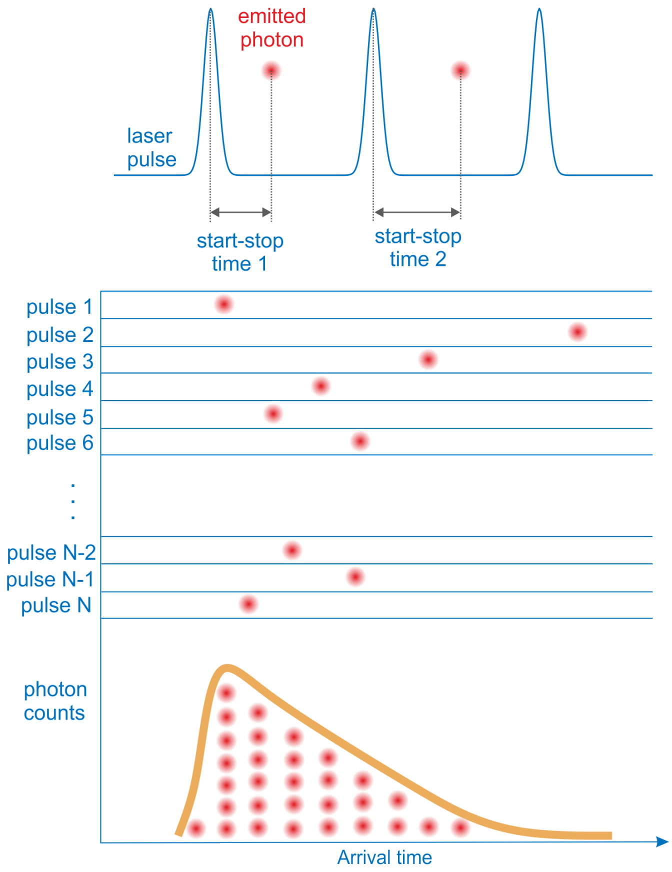

Figure 1.4: TCSPC principle. A pulsed laser excites fluorescence (blue). Less than one photon is detected in one excitation cycle on average. The detected photons (red dots) are collected and their arrival times with respect to the last laser pulse are histogrammed (bottom row). After many excitation cycles, the resulting histogram provides the lifetime decay curve, shown in orange.

1.2.2 *Frequency-domain lifetime imaging*

An alternative to TCSPC is Frequency-Domain Fluorescence Lifetime Imaging Microscopy (FD-FLIM), which requires a modulated light source and a gain-modulated detector. The excitation light is modulated in intensity with a fixed frequency (the blue curve in the Figure 1.5). The induced fluorescence emission mirrors this modulation pattern and shows, due to the fluorescence decay, a delay in time measurable as a phase shift (the red curve in Figure 1.5). The phase shift $\Delta\phi$ and modulation depth M directly depend on the fluorescence lifetime and the known modulation frequency ω (see Figure 1.5).

To extract the phase shift and modulation depth from the fluorescence emission signal, homodyne detection is often used [20]. In this method, the sensitivity of the detector is modulated (or gated) with the same frequency as the light source. This results in an intensity image with a specific brightness. By shifting the phase of the detector gain modulation with respect to the modulation of the light source in a series of fixed steps, a low-pass signal is generated for each pixel: the output image will be brighter or dimmer depending on whether the detector sensitivity is in or out of phase with the fluorescence emission. The result is a frequency-domain FLIM signal as a function of the phase difference between light source and camera gain modulations for each pixel of the detector.

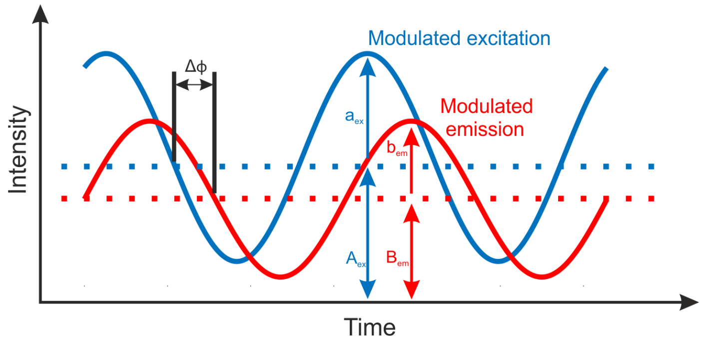

Figure 1.5: Illustration of frequency-domain fluorescence lifetime measurement. The excitation light (blue) is modulated in amplitude at a frequency ω, while the fluorescence light (red) is emitted with the same modulation frequency but with a phase shift in time, $\Delta\phi$.

In the frequency-domain method, the excitation is assumed to be sinusoidally modulated:

$$L(t) = a + b\sin(\omega t) \tag{1.6}$$

where b/a is the modulation ratio of the incident light.

The fluorescence emission is then modulated by the same frequency, but has a phase shift $\Delta\phi$ and a different modulation depth. Then, the excited-state population is given by:

$$I(t) = A + B\sin(\omega t - \Delta\phi) \tag{1.7}$$

where A/B is the demodulation parameter. For a single-exponential decay, the time-dependent intensity is described by the following first-order differential equation:

$$\frac{dI(t)}{dt} = \frac{-I(t)}{\tau} + L(t) \tag{1.8}$$

Substitution of $L(t)$ and $I(t)$ into the above equation yields:

$$\omega B\cos(\omega t - \Delta\phi) = -\frac{1}{\tau}(A + B\sin(\omega t - \Delta\phi)) + a + b\sin(\omega t) \tag{1.9}$$

From this equation, after expanding the trigonometric functions and comparing the coefficients of sine and cosine functions separately, one can obtain the relationship between phase shift and fluorescence lifetime:

$$\tau = \frac{1}{\omega}\tan\Delta\phi \tag{1.10}$$

Some fluorophores have a multi-exponential decay, consisting of two or more lifetime components. These multiple lifetime components can be separated and extracted using multiple frequency measurements and polar (or phasor) plots.

The key advantage of frequency-domain FLIM is its fast lifetime image acquisition making it suitable for dynamic applications such as measuring rapid cellular events, and its ability to measure a wide range of fluorescent lifetimes [21]. However, phase fluorometry is not suitable for fluorescence lifetime measurements at the single-molecule level. Thus, FD-FLIM is advantageous for bright, dynamic samples.

1.3 SUPER-RESOLUTION FLUORESCENCE MICROSCOPY

1.3.1 *Resolution limit of optical microscopy*

Fluorescence microscopy is currently the most commonly used method for bio-imaging. In contrast to electron microscopy and scanning probe microscopy, fluorescence microscopy is capable of live cell imaging with high degree of target selectivity. The resolution of fluorescence microscopy (its ability to resolve structural details) is fundamentally limited by the diffraction of light. In general, the emission of a fluorescent molecule can be described by an ideal oscillating electric dipole. Although a molecule has a finite size, its emission originates from a single point on its dipole axis. However, imaging this point source with an optical microscope spreads its intensity over a blurred spot of finite size, with an intensity distribution described by an Airy function. To answer the question of how close two emitters can be located that they still appear as two separate points in the image plane, let us consider two closely located emitters which emit waves in a coherent manner. Their synchronous oscillation results in a wave pattern and shows the effect of interference (see Figure 1.6 A). Destructive interference leads to the dark fringes in the superimposed wave pattern. The number and location of the observed dark fringes depend on the distance between the emitters. The farther the emitters are apart, the more dark fringes with even closer separation will appear (Figure 1.6 B). When the first dark fringe approaches the maximum collection angle Θ of the objective, the light collected by the objective will resemble that of a single point source (no interference fringes). When this happens, the microscope can no longer distinguish whether the light that comes from a single emitter or that coming from two spatially separated emitters. And this limiting value of distance, which still allows separation between two emitters, defines the lateral resolution limit of the microscope.

Let us again consider the direction of one of the dark destructive interference lanes in the interference pattern of two separated emitters (Figure 1.6 C). The difference in the distance from the first or the second emitter to a point along the dark fringe has to be half the wavelength λ. If we require that this fringe should stretch along the objective's maximum angle of light collection Θ, we find that this path difference is $d \sin \Theta$, where d is the spacing between the emitters. The path difference is equal to half the wavelength in the sample medium with refractive index n. These considerations lead to the resolution limit found by Abbe in the year 1873, which is also called

"Abbe resolution limit" or "diffraction limit" of resolution of an optical microscope:

$$d = \frac{\lambda}{2n\sin\Theta} = \frac{\lambda}{2NA} \tag{1.11}$$

In the above equation, I have defined the so-called Numerical Aperture $NA = n\sin\Theta$, which is the most important characteristics of an objective lens determining its resolving power. Common NA values range from 0.13 for air immersion objectives (4x) to 1.49 for oil immersion (100x). This corresponds to a resolution of about 310 nm and 180 nm, respectively, for an emission wavelength of λ = 500 nm.

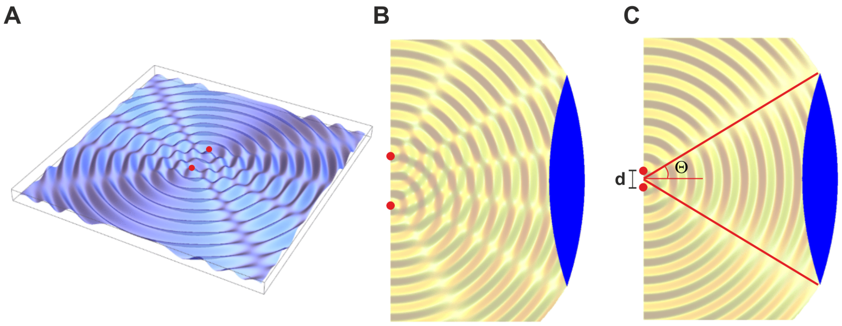

Figure 1.6: Resolution of an optical microscope. (A) Interference of waves emitted by two coherently oscillating point sources. (B-C) Observation of an interference by two spatially separated point sources within the focal plane of an objective with distance between them biger then diffraction limit (B) and equal to diffraction limit (C). This figure was adapted from Jörg Enderlein.

The spatial resolution of the microscope scales linearly with the wavelength of the used radiation. Thus, to increase the spatial resolution of imaging, radiation of shorter wavelengths can be used. This is realized in Electron Microscopy by the use of electrons (which have very short wavelengths) as the illuminating radiation [22][23]. Electron microscopy has a broad range of applications in many different fields of research including technology, industry, biomedical science and chemistry. This technique offers a higher resolution, but require more expensive equipment, complex maintenance and personnel training, as well as can be prone to artifacts. Also, due to the requirement of working in vacuum, the electron microscopy cannot be used for imaging live specimens.

1.3.2 *Enhanced resolution microscopy*

With the advent of digital image acquisition and computer-based image processing, it became possible to double the resolution of an optical microscope by combining structured illumination with wide-field detection. This is realized by Structured Illumination Microscopy (SIM) [24]. The principle of SIM is to use a spatially modulated light pattern to create a Moiré effect. The Moiré effect consists in the superposition of two periodic structures that produce a down-modulation of the frequencies. For example, two structures of high spatial frequency can produce a low spatial frequency when they overlap. The laser beams interfere at the focal plane of the objective and thus generating a patterned illumination (stripes). The intensity is hence described by a sinusoidal function. If the illumination is homogeneous (conventional illumination without patterns), the width of the point spread function does not allow for resolving two objects separated by a distance smaller than a critical value (the resolution limit), typically around 200 nm. Using structured illumination, the combination between the high spatial frequencies of a sample's structures and the high frequency of the illumination pattern creates a low frequency image, allowing to distinguish two objects that are separated by distances less than 200 nm. To understand how structured illumination can yield more spatial information than conventional wide-field illumination, let us consider a row of evenly spaced emitters along a line (see Figure 1.7 A). The distance between each two emitters is chosen to be two times smaller than the resolution limit of the wide field microscope. This sample should be now illuminated by a sinusoidal excitation pattern. When the illumination pattern is positioned in such a way that each emitter receives the same excitation intensity (Figure 1.7 A), the resulting wide-field image would show continuous line with individual emitters unresolved (Figure 1.7 B). However, if one moves the excitation pattern by one half of its period, then only every second emitter would be excited (Figure 1.7 C). In that case, the distance between excited emitters is equal to the resolution limit, and in the resulting image one can clearly distinguish between them (Figure 1.7 D). This demonstrates, how it is possible to extract more information with higher spatial resolution by structured illumination as compared to homogeneous illumination. To reconstruct a final doubly-resolved image, one has to record several images with different positions and orientations of the excitation pattern relative to the sample. This is achieved by moving the diffraction grating (translation and rotation). For 3D imaging, a grating can be used to generate three mutually coherent light beams. These beams interfere in the specimen's volume to form an illumination pattern that varies both laterally and axially [25]. SIM has been successfully used for long-term live-cell imaging [26], and for 3D imaging [27] [28].

Another enhanced resolution technique is Image Scanning Microscopy (ISM) [29] [30], which is based on a similar principle as SIM. The core idea of ISM is to replace the confocal pinhole and point

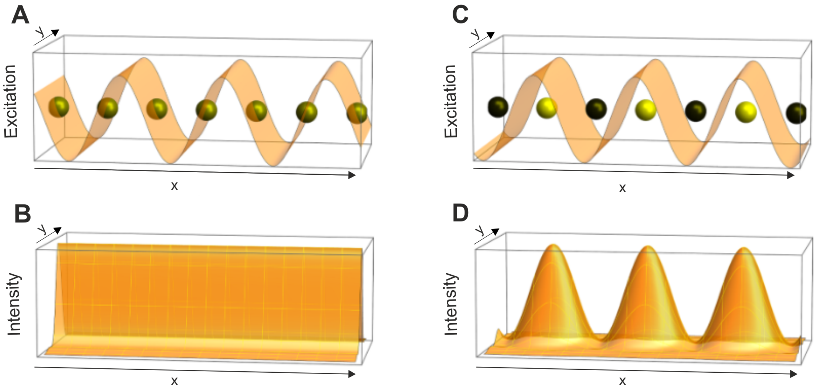

Figure 1.7: Example for the resolution enhancement by structured illumination. The figure was adapted from Jörg Enderlein.

detector of the confocal microscope with a multi-pixel array detector. When scanning the laser focus over the sample, each pixel of the detector acts as a separate light detector which records its own confocal image with very low signal intensity due to the large image magnification. Although each of these images has an extremely low signal intensity, the large number of pixels guarantees that no emission light is lost. Each photon traveling through the microscope will be registered on the detector pixels. Thus, an ISM records not a single image as a conventional confocal microscope, but a stack of images, one by each pixel on the array detector. However, simply adding all images into a single final image would yield a blurred image. For obtaining a high-resolution final image, one has to shift each scan image with respect to a common frame before adding it to the final image. Although ISM results only in a 1.63-fold raw increase in resolution, the final resolution can be elevated to 2 (similar to SIM) by appropriate image deconvolution. To speed up ISM image acquisition, a combination of ISM with confocal spinning-disk (CSD) microscopy was recently introduced [31]. This approach increases image acquisition speed by two orders of magnitude.

SIM and ISM provide an approximately two-fold resolution enhancement as compared to conventional wide-field microscopy [24][30]. They both are still limited by the diffraction of light and thus do not provide "true" super-resolution. In addition, artefacts may appear as a result of image reconstruction, therefore affecting the quality of an image [32].

1.3.3 *Super-resolution microscopy*

The first real super-resolution technique was Stimulated Emission Depletion (STED) microscopy [2]. Stimulated emission is the forced transition of an excited fluorescent molecule to its ground state by an external strong light source of suitable wavelength. In STED, the sample is scanned with two lasers simultaneously. A conventional Gaussian excitation laser focus is aligned with a second doughnut-shaped laser focus of longer wavelength, which is called "depletion beam". This depletion focus is usually generated by passing the depletion laser beam through a helical phase plate or a spatial light modulator. The depletion beam must have a laser power that is sufficient for efficient depletion of fluorophores around the center of the excitation focus. Its wavelength is chosen to be at the longer wavelengths of the fluorophore's emission spectrum. After the sample is excited by the diffraction limited tight Gaussian excitation beam, the STED beam depletes fluorophores around it with its doughnut-shaped profile. This excitation scheme leaves molecules in their excited state only inside a tight spot in the center of the doughnut, from where they can emit fluorescent light, see Figure 1.8. The resulting effective fluorescence emission spot size is no longer diffraction-limited and depends only on the intensity of the depletion beam (Figure 1.8). Photons from stimulated and spontaneous emissions can be separated based on their wavelength, using a long-pass optical filter. Higher depletion beam intensities increase the resolution, but induce photodamage. Resolution down to Angstroms has been demonstrated using highly photostable fluorescent nitrogen vacancies in diamond [33]. The achievable resolution is, in principle, unlimited, but typical values achieved in biological systems are in the 50 nm range [34].

An alternative approach to super-resolution microscopy is represented by the large class of methods based on single molecule localization. This category is named Single Molecule Localisation Microscopy (SMLM), see Figure 1.9 for illustration. It relies on switching of fluorophores between a dark and a fluorescent state. Here, the photoswitching of the fluorophores is adjusted in such a way that only a small fraction of them is emitting in every frame of a recorded movie. This is mostly achieved by controlling the chemical environment of the fluorophores and the laser intensity, and by using dyes that can be switched by light between dark and emissive states. Variants of SMLM are Photoactivated Localization Microscopy (PALM) [4] and Stochastic Optical Reconstruction Microscopy (STORM) [36]. They both rely on the same principle, that the center of an isolated diffraction-limited spot can be determined with much higher precision than its width, see Figure 1.9 B. If the fluorophores' dark-state dwell time is sufficiently long, the chance to observe two molecules simultaneously within a

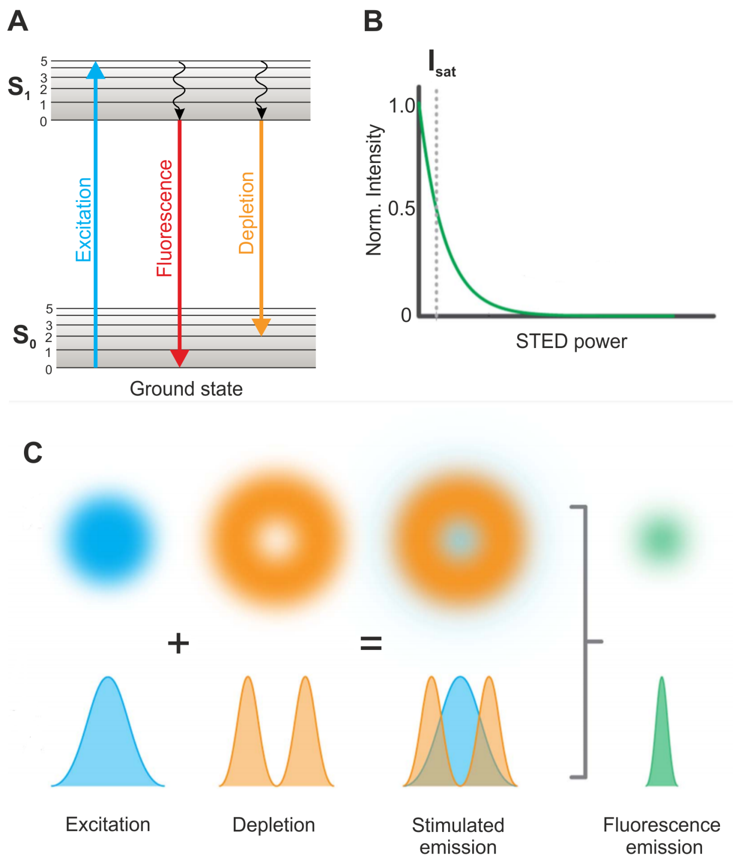

Figure 1.8: The underlying principle of STED microscopy. (A) Jablonski diagram showing excitation followed by spontaneous or stimulated emission. (B) Probability of a fluorophore to emit a photon (I_{fluo}) as a function of the intensity of the STED depletion beam (I_{STED}). At a certain threshold (I_{sat}), a molecule's ability to emit a photon is reduced to 50 %. (C) The excitation beam overlaps with a donut-shaped beam that depletes the fluorescence locally. The recorded fluorescence signal comes from the region, which has a smaller size compared to a diffraction-limited excitation. Adapted from ref. [35].

diffraction limited area is low. After localizing all activated emitters in each frame, a super-resolved image can be reconstructed from the accumulated emitter coordinates (Figure 1.9 C). The localization precision and thus the optical resolution increase with the number of collected photons during the on-time of a fluorophore [37]. Theoretically, there is no upper limit for achievable resolution. In practice, typical resolution values are in the 50 nm range [34].

The last major addition to the zoo of super-resolution techniques is MINFLUX, that utilizes some of the properties of STED microscopy [38]. Here, a location of a molecule is probed with the low-intensity region around the zero-intensity center of a doughnut-shaped exci-

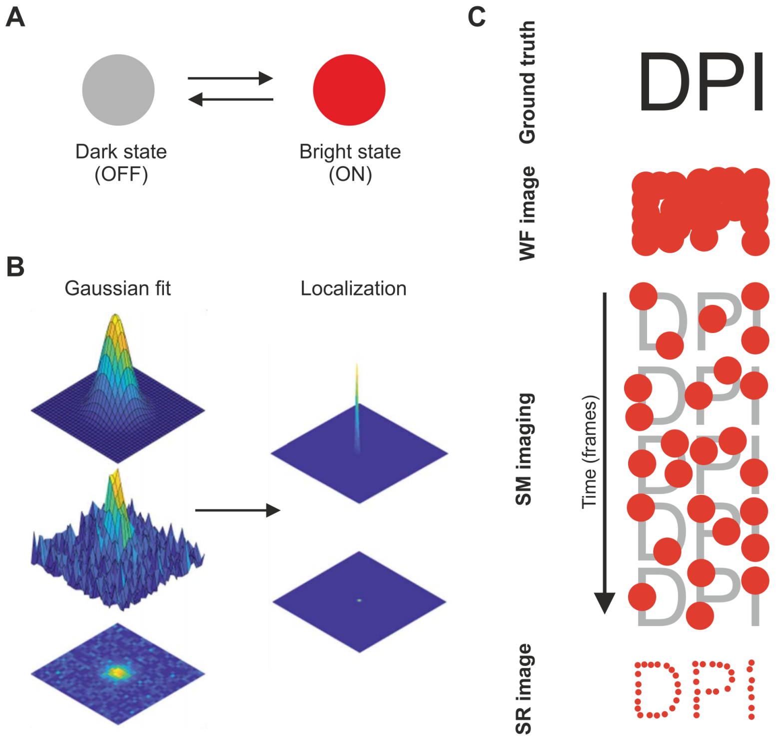

Figure 1.9: Principle of single molecule localization-based super-resolution microscopy. (A) A fluorophore is switching between 'on' and 'off' states or irreversibly from 'off' to 'on' state . (B) The centers of each Airy pattern are determined by a Gaussian fit. (C) A fraction of fluorophores is turned on in each frame, and this is repeated for a multiple cycles. Afterwards, each frame is analysed by localizing of all single-molecules, and a super-resolved image is reconstructed. Adapted from ref. [35].

tation focus, and the absence of fluorescence emission reveals the position of the molecule. If a fluorophore is located in the center of the doughnut, then the emission is zero. For two-dimensional MINFLUX, at least three scan positions of the doughnut, preferably arranged at the corners of an equilateral triangle, are required. An additional fourth position right in the triangle's center helps to decrease the uncertainty in position estimation of a molecule. Then, the set of four numbers of photons emitted from each position yields the location of a detected molecule. This strategy drastically reduces the number of photons required for a desired localization accuracy, which can be as low as a few nanometers for only a few hundred detected photons. An extension of MINFLUX is Pulsed-Interleaved MINFLUX (p-MINFLUX), which uses a simplified experimental setup and provides lifetime information as well [39]. In contrast to the original version of MINFLUX, p-MINFLUX has a modified excitation path of the microscope with four pulsed interleaved doughnut-shaped beams, which are focused on the sample arranged in a triangular pattern, with the fourth beam placed at the center of the triangle. Therefore, it does not require fast-scanning optics or field programmable gate array electronics.

All the above-mentioned super-resolution techniques rely on the switching between different photophysical states of fluorophores. In contrast, Points Accumulation for Imaging in Nanoscale Topography (PAINT) is based on reversible binding of fluorescent probes to a structure of interest [40]. Fluorophores freely diffusing in solution do generally not generate distinct single-molecule images that could be localized in a wide-field image. Only when they bind to a target structure they are detected as single molecules and can be localized in the same way as is done in conventional SMLM. An advanced variant of PAINT is named DNA-PAINT [41]. In this approach, one uses reversible and transient binding of freely diffusing single-stranded DNA labelled with a fluorophore to a target of interest, see Figure 1.10. A short single-stranded DNA called the imager strand carries the fluorophore. The imager strand binds to its complementary DNA strand called docking strand, which in turn is attached to the target (or to an affinity probe binding the target). This approach is insensitive to photobleaching of the fluorophore due to a constant replenishment of fluorophores. Moreover, in DNA-PAINT the binding/unbinding kinetics can be easily controlled. The on-time is determined by a DNA strand length and sequence, while the off time is controlled by the concentration of imager strands in solution [42] [43] [44]. Background originating from imager strands floating in solution can be reduced by using Highly Inclined Thin Illumination (HILO) for cellular imaging, or Total Internal Reflection Microscopy (TIRFM) for targets close to the surface, or with a spinning disk confocal microscope [45].

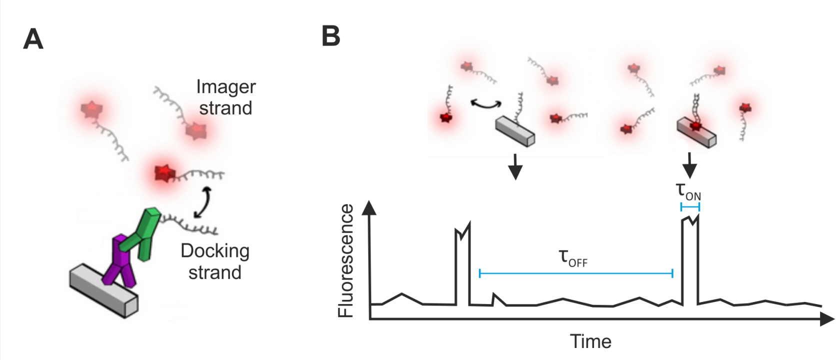

Figure 1.10: DNA-PAINT concept. (A) In situ protein-labelling strategy for DNA-PAINT using primary and secondary antibodies conjugated to a docking strand. (B) Transient binding of imager strand to the docking strand, attached in turn to a molecule of interest. The transient binding events can be referred as 'blinking', as intensity time trace shows. Adapted from ref. [42].

1.4 MULTIPLEXED SINGLE-MOLECULE LOCALISATION MICROSCOPY

In order to study several structures or molecular species and their interaction, imaging techniques with multiplexing capabilities are required. Currently used techniques for super-resolution multiplexed imaging suffer from considerable difficulties such as the spectral overlap of fluorophores and chromatic aberrations, when using spectral splitting [46]. In the following section, I will summarize the main super-resolution multiplexing techniques and their limitations, and discuss possible improvements.

1.4.1 *Spectral splitting*

Organic fluorophores and fluorescent proteins used in fluorescence microscopy emit photons with wavelengths that correspond to an energy difference between the excited and ground states. When using labels of different color for labelling different structures or molecular species, the spectra of the different fluorophores have to be disentangled in order to unambiguously identify the labelled targets. Therefore, in fluorescent microscopy, the choice of fluorophores is limited to combinations that do not overlap in their emission spectra. Most microscopes are capable of separating up to 4 different fluorophores based on their emission spectra [46]. Quantum dots (QDs) are semiconductor nanocrystals that feature a higher brightness and photostability than organic fluorophores [47]. QDs have emission spectra that are much more narrow than those of organic fluorophores, therefore allowing for better spectral separation. This helps to minimize cross-talk between emission spectra of different fluorophores. Spectral overlaps can also be tackled by using hyperspectral imaging [48] and linear unmixing [49]. This can be realized in standard fluorescent microscopes equipped with a multispectral camera. In each pixel of an image, signal intensities in several spectral windows are recorded. Reference spectra for the used individual fluorophores are measured independently in separate samples, under identical sample preparation conditions. Spectral contributions from the various fluorophores in a specimen can then be determined by calculating their individual contributions to each point in the measured spectrum.

An important problem in spectral splitting is “chromatic aberration”, which are coming from the fact that the refractive index of glass depends on the wavelength of transmitted light (dispersion). This leads to the effect that light of different wavelengths is focused into different positions. Chromatic aberrations can be negligible in traditional diffraction limited approaches, however, multi-color super-resolution imaging is impossible without appropriate image correction.

Multiplexing can be challenging when it comes to super-resolution microscopy. STED microscopy requires perfect overlap of excitation and "STED" (depletion) laser. For one single color that one wants to image, both an excitation and a depletion laser are needed, increasing the complexity of multiplexed imaging. Recently, STED has been successfully extended to four color imaging by distinguishing different fluorophores using hyperspectral detection [50]. SMLM techniques such as PALM and STORM rely on switching of organic fluorophores or fluorescent proteins. They require different blinking buffers for inducing photoswitching in different fluorophores. Such conditions tend to vary drastically between different fluorophores. Therefore, up to now simultaneous imaging of only up to four colors was possible [51]. In order to correct for chromatic aberrations, fiducial markers, such as gold nanoparticles, can be introduced into the sample [52]. They serve as reference coordinates in each of the color channels, which then permits to apply co-registration in post processing to map image coordinates from the different color channels onto each other. Another type of multiplexing SMLM is excitation Frequency-Based Single-Molecule Localisation Microscopy (fm-SMLM), which relies solely on excitation rather than fluorescence emission properties [53]. In this method, by modulating the intensities of the excitation lasers using different frequencies, the color of a channel can be identified based on the fluorophore's response to the modulated excitation. However, experimental implementations of fm-STORM and fm-DNA-PAINT are limited to three colors maximum.

1.4.2 *Exchange-based multiplexing*

All of the above-mentioned techniques are limited in number of different targets that can be potentially imaged. To increase this number, multiple rounds of labeling and imaging of the same sample can be done. The cycle of labeling includes washing, staining and photoswitching buffer exchange (for STORM acquisition). Staining is the process of the pairing of a primary antibody and a secondary antibody, which usually carries a fluorophore (indirect staining). Images of different staining cycles are later overlayed forming the final multi-target super-resolution image. However, the sample integrity during the re-labelling procedures can be compromised. Solution exchange in a sample chamber can be performed by microfluidic systems. Recently, several protocols for automated microfluidic systems have been reported [54] [55]. One of the implementations of a microfluidic system is the open-source NanoJ-Fluidics platform. It uses a computer-controlled syringe pump array, that takes care of fluid exchange in order to perform cell fixation and sequential rounds of labelling [54]. This system is based on low-cost Lego hardware and ImageJ-based software. Imaging of five different targets in a single cell with a combination of STORM and DNA-PAINT was reported. Another example is Multiplexed Automated Serial Staining Stochastic Optical Reconstruction Microscopy (masS3TORM), a technique capable of fully automated 3D direct STORM imaging and solution exchange employing a commercially available pipetting robot [55]. This approach enabled 3D super-resolution imaging of 15 targets in single cultured cells and 16 targets in individual neuronal tissue samples.

Another promising multiplexing techniques is called Exchange-PAINT. It is also based on sequential imaging of multiple targets. For Exchange-PAINT, only a single fluorophore and a single laser source is required [6], see Figure 1.11. The technique exploits the orthogonal binding of different complementary pairs of single DNA strands for assigning different DNA conjugates (imager/binding strands) to different targets. Sequential introduction of different imager strands allows for multiplexed super-resolution imaging. Importantly, in Exchange-PAINT all imager strands carry the same fluorophore, thus completely avoiding the chromatic aberrations. The number of targets that can be imaged with Exchange-PAINT is potentially unlimited, but since the total acquisition time is proportional to the number of targets, highly multiplexed imaging can be time-consuming. A detailed overview of the optical and computer-controlled microfluidics setups, designed and built as a part of this work particularly for Exchange-PAINT experiments, can be found in Chapter 3.

As already mentioned, Exchange-PAINT is time-consuming. DNA-PAINT can be much improved by using rationally designed DNA sequences and buffer conditions that speed up data acquisition. It was shown, that by optimizing of these parameters, a 10x speed increase in DNA-PAINT image acquisition can be readily achieved, while maintaining the high image resolution capabilities [56]. In another work, addition of ethylene carbonate to the imaging buffer, multiple repeats of the imager docking sequence, and using a spacer between the docking strand and the antibody resulted in imaging speed acceleration and improved image quality [44].

A more recent variant of this technique uses a kinetic barcoding in addition to structural barcoding. The concept of kinetic barcoding is that different targets are conjugated with docking strands of different lengths that are partially complementary to the same imager strand. This results in different binding kinetics, which can be used as a parameter for target identification. Using this idea, it was possible to identify 124 DNA origami structures with different sets of docking strands with 97 % accuracy [57]. However, kinetic barcoding for cel-

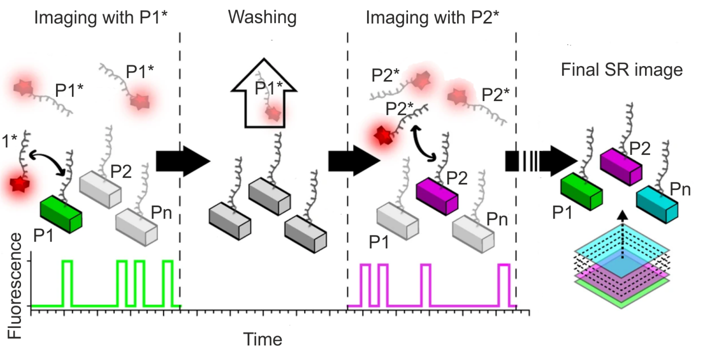

Figure 1.11: Schematic representation of sequential Exchange-PAINT of multiple targets. Left to right: P1* imager strands are in solution and interact with their complementary target sequence, P1. After the first acquisition round, the P1* imager strands are washed away and P2* imagers are introduced to image the next target. The process is repeated for the remaining targets, and different pseudo-colors are assigned for each target. Last, all images are aligned and overlaid to form the final multiplexed Exchange-PAINT image of n targets. Adapted from ref. [42].

lular PAINT is challenging due to the dense and sticky environment inside a cell, which strongly affects the imager binding kinetics, thus making targets identification unreliable.

Another promising way of multiplexing is to utilize fluorescence lifetime as a parameter for target identification. Such lifetime-based multiplexing is independent on binding kinetics, while still allowing for multi-target imaging in parallel. Similar to Exchange-PAINT, lifetime-based multiplexing uses probes with similar emission spectrum, but different fluorescence lifetimes, thus completely avoiding chromatic aberration [58]. As a result, lifetime-based multiplexing combined with DNA-PAINT has a great potential for multiplexed imaging. Our implementation of Fluorescence Lifetime PAINT (FL-PAINT) can be found in Chapter 5. I validated the technique using the well-established Exchange-PAINT and applied FL-PAINT to cellular super-resolution imaging of two commonly used cell lines: COS-7 and HeLa.

1.5 AXIAL LOCALIZATION OF FLUOROPHORES

Despite the rapid development of super-resolution techniques, most of them show a significant difference in their lateral and axial resolution capability. In SMLM super-resolution is achieved by localizing of single emitters, thus enabling the reconstruction of super-resolved images with a lateral resolution of around 10-20 nm. However, real samples are three-dimensional. Several experimental techniques have been developed to extend the SMLM to the third dimension. Among them, the most commonly used are: PSF engineering approaches such as astigmatic imaging [59] or bi-plane imaging [60], and interferometric approaches (iPALM [61] and isoSTED [62]).

Astigmatic imaging is the most straightforward method for single emitter localization in 3D. It belongs to a group of 3D-SMLM techniques, usually referred as PSF engineering. These techniques rely on the use of PSFs that strongly depend on the axial position of an emitter to enable accurate axial localization. In astigmatic imaging, this is achieved by positioning a cylindrical lens with long focal length (0.5-1.0 meter) into the emission path, typically next to the camera sensor. The induced astigmatism results in an elliptic PSF, where its ellipticity and orientation encode for a molecule's axial position. The axial depth of imaging using astigmatism is limited to around 800 nm. The second PSF engineering approach uses phase masks or spatial light modulators to modify the PSF of a single fluorophore into e.g. a double helix-shaped form, which rotates along the z axis [60]. Thus, the two lobes of the double-helix are oriented in a direction that depends on the axial position of the emitter. Double helix PSF SMLM is capable of axial localization over a range of 2 μm. Another technique, called bi-plane imaging, relies on the variation of the PSF width along the axial direction. The biplane approach images emitters in two different planes, slightly defocused one with respect to the other. By analyzing the two images of an emitter in the two image planes, one determines its axial position over an axial range of 1 μm.

However, the just discussed techniques suffer from a common drawback: the axial resolution is three to five times smaller than the lateral resolution. This is not the case for interferometry-based methods such as Interferometric Photoactivated Localization Microscopy (iPALM) [61] and isoSTED [62]. In these approaches, fluorescence is excited or detected from two sides of a sample with two objectives, to generate an excitation intensity interference pattern along the axial direction or, alternatively, to interfere the collected florescence on a detector. Using two objectives has the benefit of collecting most of the emitted fluorescence, making these approaches exceptionally photon-efficient. However, these methods are technically complex and challenging in maintenance and operation, therefore limiting their broad application.

Another class of axial super-resolution methods exploits near-field coupling of light at an interface between two media of high and low refractive index. The two most widely used approaches from this category are Variable Angle Total Internal Reflection Microscopy (va-TIRFM) [63] and Super-critical Angle Fluorescence (SAF) imaging [64] [65]. In TIRFM, the sample is illuminated through the glass cover slide with a plane wave travelling at an angle above the critical angle of Total Internal Reflection (TIR). This generates an exponentially decaying excitation intensity in the sample above the glass surface. The penetration depth of this evanescent field is typically a few hundred nanometers. Thereby, only emitters close to the interface will be excited. Consequently, TIRFM images only a small bottom section of a cell. This results in a much higher signal-to-noise ratio than that of classical wide-filed illumination. In fact, this is one of the main reasons why TIRFM is widely used by biologists to observe focal adhesion zones [66]. However, extracting quantitative height information from TIRFM images is not trivial due to its intensity-based nature. Variable angle TIRFM (va-TIRFM) overcomes this problem by recording several images at different excitation beam incidence angles, thus modulating the evanescence excitation field [63]. By analysing the emission intensity modulation as a function of excitation wave incidence angle, the distance of fluorescent structures from the surface can be precisely determined. In this way, using the ratio of emitter fluorescence intensities measured at different incidence angles of the excitation light, it is possible to calculate the height of single fluorophores from the substrate with extremely high axial resolution (down to nanometers). Over the years, va-TIRFM was employed in multiple biological assays: for studying focal adhesion zones [66], cell topography [67], or the axial motion of secretory granules in living cells [68]. Another near-field technique is Super-critical Angle Fluorescence (SAF) imaging. This technique is the emission equivalent of TIRFM and uses the distance-dependent near-field coupling of the emission of a fluorescent emitter into glass above the TIR angle [64]. By measuring the ratio of the intensity of this super-critical angle emission to the (distance-independent) intensity of sub-critical angle emission, one can determine the distance of an emitter from the glass surface. A recent application of SAF in combination with STORM achieved an axial resolution of 20 nm over a range of 150 nm from the surface [69]. However, both SAF and va-TIRFM require very careful alignment and calibration. As both techniques are strongly dependent on precise measurements of fluorescence intensities, they suffer from background and cross-talk.

1.5.1 *Metal-induced energy transfer*

Metal-Induced Energy Transfer (MIET) is a recently developed and highly promising alternative for 3D localization [70][71]. MIET relies on the energy transfer between an emitter and a thin metal layer (Figure 1.12). The energy transfer results in the quenching of the emitter's excited state which modulates both its intensity and fluorescence lifetime. Due to the steep distance-lifetime dependency (distance between fluorophore and metal layer), an experimentally measured lifetime value can be converted into a distance of the emitter from the metal surface, provided the quantum yield, free space lifetime, and the emission dipole orientation of the emitter are known. MIET is similar to Förster Resonance Energy Transfer (FRET), where the energy transfer occurs between donor and acceptor molecules and the relative distance between them can be obtained with sub-nanometer accuracy over a range of 2-12 nm, depending on the selection of the donor-acceptor pair. In contrast to FRET, MIET uses the metal layer as energy acceptor, allowing for measuring axial distances over an axial range that is by one order of magnitude bigger than that of FRET (up to 150-200 nm, depending on the metal type and layer thickness). In order to convert an experimental fluorescence lifetime value into a height value, a theoretically calculated calibration curve is needed. This is done by solving Maxwell's equation for an electric dipole emitter (fluorophore) in proximity to the metal layer [72].

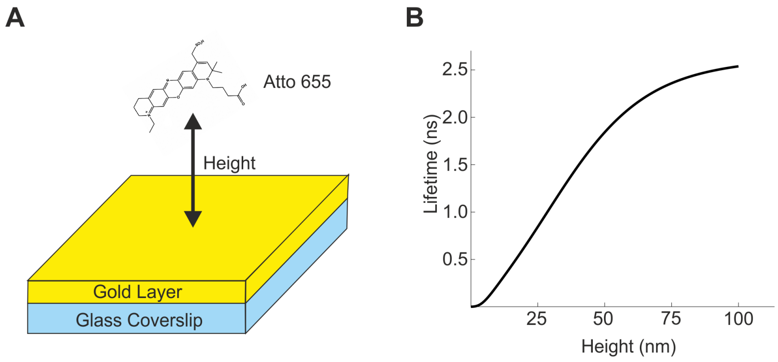

Figure 1.12: Metal-Induced Energy Transfer. (A) MIET experiment sample geometry. Atto 655 in close proximity to a thin layer of gold. (B) Theoretical dependence of fluorescence lifetime on the distance between fluorophore and gold layer of 10 nm thickness.

The axial localization accuracy achieved with MIET depends on both the accuracy of emitter orientation determination and the accuracy of the lifetime determination. The latter is in turn inversely related to the square root of the number of photons recorded (similar to the localization accuracy in SMLM).

MIET imaging was applied to various biological questions, for example for studying the 3D architecture of focal adhesion complexes [73], for following the reorganization of the actin cytoskeleton during the transformation of epithelial to mesenchymal cells [74], or for measuring the inter-bilayer distance of a nuclear envelope [75]. At the single-molecule level, MIET was shown to be able of localizing single emitters deposited on dielectric spacers of known thickness. The reported axial localization accuracy was 2.5 nm [71]. Single-Molecule Metal-Induced Energy Transfer (smMIET) was used for axial co-localization of two emitters on rigid DNA origami nanostructures [76]. A further increase in axial resolution was achieved with the recently developed variation of MIET, where the metal layer is replaced with a single layer of graphene. This variant of MIET was called Graphene-Induced Energy Transfer (GIET) [77]. GIET features a ten-fold improvement in axial resolution, as compared to MIET. The axial working range of GIET is limited to ca. 25 nm.

2

NANOBODY DETECTION OF STANDARD FLUORESCENT PROTEINS ENABLES MULTI-TARGET DNA-PAINT WITH HIGH RESOLUTION AND MINIMAL DISPLACEMENT ERRORS

2.1 MANUSCRIPT: NANOBODY DETECTION OF STANDARD FLUORESCENT PROTEINS ENABLES MULTI-TARGET DNA-PAINT WITH HIGH RESOLUTION AND MINIMAL DISPLACEMENT ERRORS

The original research article entitled: " Shama Sograte-Idrissi[1], **Nazar Oleksiievets**[1], Sebastian Isbaner, Mariana Eggert-Martinez, Jörg Enderlein, Roman Tsukanov, Felipe Opazo, Nanobody Detection of Standard Fluorescent Proteins Enables Multi-Target DNA-PAINT with High Resolution and Minimal Displacement Errors, Cells 2019, 8, 48. " was published. Nazar Oleksiievets performed all DNA-PAINT experiments, performed data analysis and co-wrote the manuscript.

The published research article is currently available at `https://www.mdpi.com/2073-4409/8/1/48`

---

[1] These authors contributed equally to this work

cells MDPI

Article

Nanobody Detection of Standard Fluorescent Proteins Enables Multi-Target DNA-PAINT with High Resolution and Minimal Displacement Errors

Shama Sograte-Idrissi [1,2,3,†], Nazar Oleksiievets [4,†], Sebastian Isbaner [4], Mariana Eggert-Martinez [1,2,3], Jörg Enderlein [4], Roman Tsukanov [4,*] and Felipe Opazo [1,2,*]

[1] Institute of Neuro- and Sensory Physiology, University Medical Center Göttingen, 37073 Göttingen, Germany; shama.sograteidrissi@med.uni-goettingen.de (S.S.-I.); mariana.eggertmartinez@gmail.com (M.E.-M.)
[2] Center for Biostructural Imaging of Neurodegeneration (BIN), University of Göttingen Medical Center, 37075 Göttingen, Germany
[3] International Max Planck Research School for Molecular Biology, Göttingen, Germany
[4] Third Institute of Physics-Biophysics, Georg August University, 37077 Göttingen, Germany; nazar.oleksiievets@uni-goettingen.de (N.O.); sebastian.isbaner@phys.uni-goettingen.de (S.I.); jenderl@gwdg.de (J.E.)
* Correspondence: roman.tsukanov@phys.uni-goettingen.de (R.T.); fopazo@gwdg.de (F.O.); Tel.: +49-(0)-55139-22297 (R.T.); +49-(0)-55139-61155 (F.O.)
† These authors contributed equally to this work.

Received: 14 December 2018; Accepted: 11 January 2019; Published: 14 January 2019

Abstract: DNA point accumulation for imaging in nanoscale topography (PAINT) is a rapidly developing fluorescence super-resolution technique, which allows for reaching spatial resolutions below 10 nm. It also enables the imaging of multiple targets in the same sample. However, using DNA-PAINT to observe cellular structures at such resolution remains challenging. Antibodies, which are commonly used for this purpose, lead to a displacement between the target protein and the reporting fluorophore of 20–25 nm, thus limiting the resolving power. Here, we used nanobodies to minimize this linkage error to ~4 nm. We demonstrate multiplexed imaging by using three nanobodies, each able to bind to a different family of fluorescent proteins. We couple the nanobodies with single DNA strands via a straight forward and stoichiometric chemical conjugation. Additionally, we built a versatile computer-controlled microfluidic setup to enable multiplexed DNA-PAINT in an efficient manner. As a proof of principle, we labeled and imaged proteins on mitochondria, the Golgi apparatus, and chromatin. We obtained super-resolved images of the three targets with 20 nm resolution, and within only 35 minutes acquisition time.

Keywords: nanobodies; super-resolution microscopy; multi-color imaging; fluorescent proteins; microfluidics; DNA-PAINT; molecular localization; single domain antibodies (sdAb); multiplexing; linkage error

---

1. Introduction

Super-resolution light microscopy is developing rapidly, and a growing number of cell biologists are embracing this technology to study proteins of interest (POI) at the nanoscale. Single molecule localization techniques like PALM [1], (d) STORM [2,3], and others [4] achieve resolutions that allows for distinguishing molecules that are separated by only a few nanometers. Among these localization techniques, DNA Point Accumulation for Imaging in Nanoscale Topography (DNA-PAINT) [5] has demonstrated to achieve a resolution below 5 nm on DNA origami structures [6,7] and offers the possibility to detect multiple POIs within the same sample [8]. A special feature of DNA-PAINT is that it is not limited by photobleaching of the fluorophore, due to the constant replenishment of fluorophores from the solution. In fact, a target site carries one or more single stranded DNA oligonucleotides (commonly referred to as the docking strand or handle) instead of a single fluorophore, while a second single stranded DNA molecule with a complementary sequence to the docking strand bears a fluorophore (referred to as the imager strand). In a DNA-PAINT experiment, the imager strands continuously bind to the docking strands and unbinds due to thermal fluctuations. The continuous transient binding of the imager strands results in sparse "blinking-like" fluorescence detection events. Similar to PALM or STORM, these events are then precisely localized to reconstruct a super-resolved image. The localization precision depends on the number of photons collected in a single event, whereas the total number of events recorded affects the quality of the final super-resolved image. Importantly, DNA-PAINT benefits from the orthogonality of DNA hybridization (with different sequences). DNA docking strands with different nucleotide sequences can be associated with different targets, thus making it easy to obtain multi-target super-resolution images using a single fluorophore. Thereby, chromatic aberrations are avoided, resulting in a comparable resolution for all the POIs under investigation [9]. For such multiplexed imaging (known as Exchange PAINT [8,9]), sequential introduction of different imager strands is required.

However, this methodology imposes several challenges to cell biologists who want to optimally image POIs with DNA-PAINT. Usually, primary antibodies that bind to a POI are labeled with secondary antibodies which carry the docking strand [10]. However, such an approach introduces a spatial displacement of up to 25 nm between the target site and the fluorophore [11–13], which seriously limits the resolving power of all single molecule localization super-resolution techniques, which use conventional antibody-based immunofluorescence labeling. The first attempt to minimize this "linkage-error" [14] was to use primary antibodies that are directly coupled to docking strands [8]. Typically, this has been performed by using an undirected coupling chemistry via maleimide-peG2-succinimidyl ester or via dibenzocyclooctyne(DBCO)-sulfo-NHS-ester cross linkers [10]. These non-targeted coupling methods can interfere with the binding ability of the primary antibody to the POI by reacting at the paratope of the antibody. Additionally, they result in a mixture of antibodies containing a broad distribution of the number of docking strands (even including antibodies with none), which results in an inhomogeneous labeling density of the POIs and makes single molecule detection non-quantitative. Recently, an attractive alternative to reduce displacement and avoid polyclonal secondary antibodies (and their inherent problems) has been proposed by using the immunoglobulin binding Protein A and Protein G coupled to docking strands [15].

To further tackle the "linkage error" of the reporter fluorophores, several small monovalent affinity probes are continuously emerging [16]. For instance, small DNA or RNA molecules known as aptamers [17–19] or single-domain antibodies (sdAb, or nanobodies) [20] have recently gained popularity in the field of super-resolution imaging [21–23]. Nanobodies are obtained from a special type of immunoglobulins known as heavy chain antibodies (hcAb), which are found in camelids. The recombinant production of the variable domain of these hcAbs result in a functional nanobody with only 2–3 nm size [24]. Recently, a significant improvement in spatial resolution, as compared to the conventional antibody immunofluorescence, was demonstrated by using nanobodies for labeling [12,25]. In addition to their small size, high specificity, and monovalent binding affinities, which make them an ideal tool for microscopy, the recombinant nature of nanobodies endows them with a great flexibility and allows introducing all types of modifications in a precise manner. This last feature permits to rationally design and control the number and location of desired functional elements on them (e.g., the number and locations of fluorophores or docking strands [22,25]).

Unfortunately, only few nanobodies able to recognize endogenous mammalian proteins are currently available. However, several new nanobodies against different fluorescent protein families like GFPs (from *Aequorea Victoria*), RFPs (from *Dicosoma* sp.), or mTagBFPs (from *Entacmaea quadricolor*) are now easily accessible. This opens the opportunity to obtain super-resolution images with a minimal linkage-error on a wide range of biological samples. Fluorescent proteins like EGFP [26], mCherry [27], and mTagBFP [28] are widely used in the life-sciences, fused to POIs within simple cell lines, large yeast libraries [29], and countless other genetically modified organisms (e.g., *Arabidopsis thaliana* [30], *Caenorhabditis elegans* [31], *Drosophila melanogaster*, [32] or mice [33]).

Here, we used a custom-built multi-channel total internal reflection fluorescence (TIRF) microscope and three nanobodies targeting mTagBFP, EGFP, and mCherry to perform exchange PAINT experiments on three different targets inside the same cell. For efficient buffer solution exchange, a versatile custom-built microfluidics system was developed and implemented. Exchange PAINT was performed by sequential introduction of three different imager strands and washing in between. Recorded single-molecule localization detection events were subsequently analyzed for reconstructing super-resolved images for each of the three targets. We achieved a resolution of 20 nm with a localization precision of 14 nm within 35 min of acquisition time (per target). We envision that nanobody-based DNA-PAINT will provide an efficient solution for the protein-DNA linkage problem and will help to exploit the full power of DNA-PAINT for cellular imaging, considering the broad availability of many fluorescent proteins.

2. Materials and Methods

2.1. Nanobody Coupling to Docking Oligo

The unconjugated nanobodies FluoTag®-Q anti-GFP, FluoTag®-Q anti-RFP, and the FluoTag®-Q anti-TagBFP (NanoTag Biotechnologies GmbH, Göttingen, Germany, Cat. No: N0301, N0401, and N0501, respectively) carry one ectopic cysteine at the C-terminus then allowing for chemical couplings via a thiol reactive compound. The DNA docking strands (Biomers GmbH, Ulm, Germany) were functionalized with an azide group at 5′-end and, in some cases, Atto488 fluorophore at the 3′-end. The coupling of the docking strands to the nanobodies were performed following the procedure from Schlichthärle and colleagues [34], with minor modifications. In brief, 15 to 20 nmol of nanobodies in phosphate buffer saline (PBS, 127 mM NaCl, 10 mM Na_2HPO_4, 2.7 mM KCl, 0.2 mM KH_2PO_4, pH7.4) were incubated with a final concentration of 5 mM TCEP (Sigma-Aldrich, Zwijndrecht, The Netherlands) for 2 h at 4 °C to reduce the ectopic cysteine. Afterwards, the excess of TCEP was removed by exchanging the buffer to PBS pH 6.5 using spin Amicon filters with a MWCO of 10 kDa (Merck/EMD Millipore, Molsheim, France, Cat. No. UFC501096). The reduced TCEP-free nanobodies were immediately mixed with 50 molar excess of maleimide-DBCO crosslinker (Sigma-Aldrich, Cat. No. 760668) and incubated overnight at 4 °C with mild stirring. The excess of DBCO crosslinker in the buffer was exchanged to PBS pH 7.4 using Amicon Filters (Molecular weight cut-off 10 kDa) as described previously. Azide functionalized docking strands were added (in 10 molar excess as performed also in [25]) to the crosslinker-coupled nanobody and incubated at room temperature for ~2 h with slow head-to-tail shaking. The excess of docking strands was then removed from the conjugated nanobodies using size exclusion chromatography (Superdex 75 Increase 10/300 column, Cat. No: 29148721) and ÄKTA pure 25 system (GE Healthcare life science, Chicago, Ill, USA). The correct fractions of labeled nanobodies were then identified by the SDS-PAGE followed by SYBR GOLD staining (Thermo Fisher, Waltham, MA, USA, Cat No: S11494). The docking strands sequences used for the assay were taken from Agasti et al [8]. FluoTag®-Q anti-GFP was coupled to P1 * sequence (5′-CTAGATGTAT-Atto488-3′), FluoTag®-Q anti-RFP was coupled to P2 * (5′-TATGTAGATC-3′), and the FluoTag®-Q anti-TagBFP was coupled to P3* (5′-GTAATGAAGA-3′). Imager strands were labeled with Atto655 fluorophore at the 3′ end.

2.2. Immunostaining

COS-7 cells were cultured in Dulbecco modified Eagle medium (DMEM) with 4 mM l-glutamine and 10% fetal calf serum (Thermo Fisher Scientific), supplemented with 60 U/mL of penicillin and 0.06 mg/mL streptomycin (Sigma-Aldrich) at 37 °C and 5% CO_2. Prior immunostaining and imaging, ca. 20,000 cells/well, were plated in 8-well chamber (155411PK, Thermo Fisher Scientific). The next day, the cells were transfected using 2.5% lipofectamine 2000® and 300 ng of plasmid in Optimem medium (Thermo Fisher Scientific). After incubation of ca. for 16 h, the cells were fixed using 4% paraformaldehyde (PFA) for 30 min at room temperature. The remaining aldehydes were quenched with 0.1 M glycine in PBS for 30 min. Afterwards, cells were permeabilized and blocked using 3% bovine serum albumin (4) and 0.1% Triton X-100 in PBS for 30 min at room temperature. Buffer solution containing nanobodies coupled to the docking strand (50 nM) was used to stain the cells. For this purpose, we proceeded with incubation of 1 h at room temperature, with slow orbital shaking. Finally, the cells were rinsed with PBS and then post-fixed with 4% PFA for 30 min at the room temperature. As described previously, remaining aldehydes were quenched with 0.1 M glycine in PBS. Cells were stored in PBS buffer at 4 °C.

2.3. Exchange PAINT Experiment

The imager strands P1 5′-CTAGATGTAT-3′-Atto655, P2 5′-TATGTAGATC-3′-Atto655, and P3 5′-GTAATGAAGA-3′-Atto655 (Eurofins Genomics) were aliquoted in TE buffer (Tris 10 mM, EDTA 1 mM, pH 8.0) at a concentration of 100 µM and stored at −20 °C. Prior to the experiment, the strands were diluted to the final concentration of 2 nM in PBS buffer, containing 500 mM NaCl. A chamber with eight wells (155411PK, Thermo Fisher Scientific) was fixed on the microscope stage with clips. A PDMS layer was used as a chamber cover and supported the inlet tubes and a tube for suction. The slide was held on the microscope stage for 0.5 h before the acquisition to equilibrate to the room temperature and achieve mechanical stability. Injection of fluids and its removal was done using our custom-built microfluidic setup, designed and constructed particularly for the Exchange PAINT experiment. First, the well was rinsed twice with 500 µL PBS buffer (pH 8.0, NaCl 500 mM). Then, suitable cells for imaging were selected based on the presence of the signal from the expressed fluorescent proteins: mTagBFP, mCherry, and EGFP. The cells were located by exposing them to the following laser excitation wavelengths and detecting the fluorescence in the corresponding emission channel: mTagBFP-405 nm laser, EGFP-488 nm laser, and mCherry-561 nm laser. A HILO-illumination scheme was used to excite the cells. The laser power was adjusted according to the sample brightness (respectively 0.5 mW, 1 mW, and 2 mW at the output of the optical fiber). Each selection movie of the fluorescent proteins included between 200–250 frames (Figure 4A1–A3). Afterwards, we proceeded with Exchange PAINT on the selected cell. All the solutions were injected into the cell by applying air pressure in the corresponding pressurized tube. First, imager strand P1 (2 nM) in PBS buffer (500 µL) was injected into the well and incubated for 10 min before the acquisition. Typical DNA-PAINT movie included 21,000 frames (corresponds to 35 min). The following acquisition settings for the emCCD camera was used: Exposure time 100 ms, pre-amplifier gain 3.0, EM gain 10. The laser 638 nm was set to 10–15 mW (corresponds to an excitation illumination power density of 0.4–0.6 kW/cm^2). After PAINT movie acquisition, an extensive wash of the well was performed (4–6 times volume exchange, in total about 3 mL buffer within 5 min), in order to remove the imager solution from the well completely. Suction was performed by the micro peristaltic pump (Makeblock) After the extensive wash, the next imager solution was introduced. We proceeded with the same solution exchange procedure also for the imagers P2 and P3 (see comprehensive chart in Figure 3B). All the experiments were carried out at a constant temperature of 22 ± 1 °C, which was crucial for the mechanical stability of the sample (remaining mechanical drifts were corrected for during the analysis).

2.4. DNA-PAINT Movies Analysis

Raw DNA-PAINT movies were analyzed using the Picasso software package [10]. In the end, drift-corrected super-resolution images were reconstructed, and the average localization accuracy was estimated. For further analysis of the achieved image resolution, the Fourier Ring Correlation (FRC) [35] technique was employed. First, localization events were detected using Picasso: Localize. For the specific binding-events recognition, the signal box size length was set to 7 pixels and the minimum net gradient was limited to the range of 1700 to 3500 (depends on the protein expression level in a particular cell). Then, the localized bright spots were fitted with the LQ Gaussian method to obtain precise fluorophore coordinates. The total number of localization events varied from 150,000 to 2,500,000 for the whole movie. The output file with the localization coordinates was then loaded into Picasso: Render. Using the Undrift RCC feature (segmentation 500 frames), movies were corrected for mechanical drift. The final reconstructed super-resolved images were exported in PNG format. Finally, all three reconstructed images of different organelles were merged together for each imaged cell using ImageJ [36], see Figure 4 C1,C2, D1–D3. The average localization precision (NeNa [37]) was estimated for each reconstructed super-resolved image. For image resolution quantification, Fourier Ring Correlation (FRC) [35] was applied using the FIRE ImageJ plugin [38], for detailed numbers see Supplementary Information, Table S1. Further image resolution analysis was performed by creating a resolution map using SQUIRREL [39] (super-resolution quantitative image rating and reporting of error locations), see Figure S4 in the Supplementary Information.

3. Results

3.1. Optimization of Cells Transfection and Nanobody Staining for EXCHANGE DNA-PAINT Imaging

First, we optimized the transfection of mammalian cells (COS-7) with plasmids encoding for proteins present in different organelles fused to various fluorescent proteins. We used TOM70 fused to EGFP to reveal mitochondria, GalNacT was fused to mCherry to detect the Golgi apparatus and histone H2B was fused to mTagBFP to detect the cellular chromatin (nucleus). Additionally, we used currently available nanobodies, which bind strongly and specifically to the three fluorescent proteins mentioned above. Each type of nanobodies were labelled with a unique docking strand, enabling the acquisition of multiple targets using Exchange PAINT, in single cells (see scheme in Figure 1).

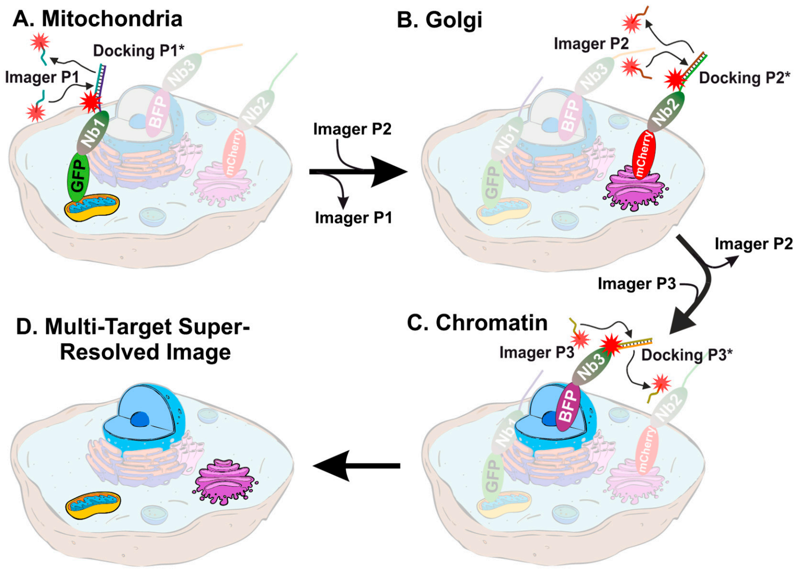

Figure 1. Schematic representation of multi-target exchange point accumulation for imaging in nanoscale topography (PAINT) in COS-7 cells. Sequential introduction of imager strands with different sequences reveal multiple targets and result in multi-color super-resolution image. (**A**) DNA-PAINT imaging of mitochondria with Imager P1. (**B**) DNA-PAINT imaging of the Golgi apparatus with Imager P2. (**C**) DNA-PAINT imaging of nucleus/chromatin. (**D**) The resulting super-resolved image of a single cell with three colors overlaid. The cells were stained with (1) nanobody anti-GFP (Nb1) coupled to the DNA strand P1, (2) nanobody anti-mCherry (Nb2) coupled to the docking P2, and (3) nanobody anti-mTagBFP (Nb3) coupled to the docking strand P3.

All nanobodies had an extra ectopic cysteine at their C-terminus that allowed the conjugation of molecules via maleimide chemistry. We used a maleimide-DBCO as a cross-linker to attach the single stranded DNA oligo bearing an azide group on its 5′ end (Figure 2A,B). The coupling of the docking strand was thus performed in two sequential steps. First, the nanobody was incubated with a 50 molar excess of the maleimide-DBCO cross-linker, inducing a thiol-maleimide conjugation with the previously reduced single ectopic cysteine at the C-terminus of the nanobody [22]. After removing the excess of cross linker, the complex was incubated with a 10 molar excess of azide functionalized DNA oligo to induce a strain-promoted azide–alkyne cycloaddition (copper-free click chemistry [40]). The separation of the excess of DNA oligo from the mixture was performed using a size exclusion chromatography (SEC), resulting typically in two obviously separated elution fractions (Figure 2C). This is an essential step to avoid unspecific signal from the free DNA oligo. As a first routine quality control after SEC, different elution fractions were passed through a polyacrylamide gel electrophoresis (PAGE), stained with SYBR gold, to report the presence of the oligonucleotides (Figure 2D). Only the fractions containing a clean band at the right molecular weight were used subsequently for the immunoassays of the transfected COS-7 cells. Due to the large excess of cross-linker and docking strands used for each coupling step (see Methods section), we are confident that a major proportion of the nanobodies were labelled with the docking oligo.

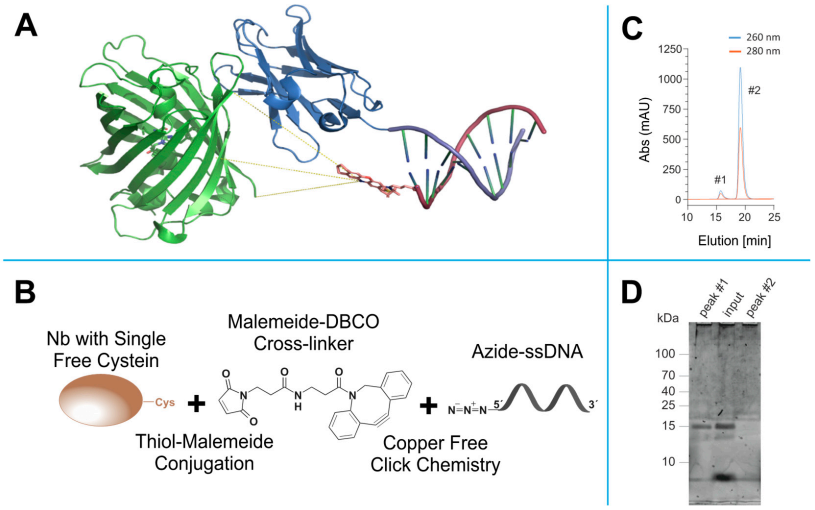

Figure 2. Click- and thiol-based strategy to conjugate nanobodies to a docking DNA strand for DNA-PAINT. (**A**) Anti-GFP nanobody (blue) bound to EGFP (green). The nanobody is modified with a docking stand with a complementary Atto655-labelled Imager strand attached (EGFP: Nanobody complex extracted from (PDB: 3K1K), DNA strand, and Atto655 were generated using ChemDraw (CambridgeSoft, Cambridge, MA, USA) and ensembled using PyMOL Molecular Graphics System (Schrödinger, LLC, Ney York, NY, USA). The yellow lines represent three estimated distances (theoretical estimates: 3.1 nm, 3.3 nm and 3.4 nm) of the fluorophore to the protein of interest (POI) extracted from the in silico model. (**B**) Scheme representing the orthogonal coupling strategy of docking DNA strand to the nanobody. (**C**) Example of the size-exclusion chromatography (SEC) for the separation of DNA-coupled nanobody (#1) from the excess of azide-functionalized docking strand (#2). (**D**) Example of the SDS-PAGE of fraction collected from the SEC run, post stained with SYBR gold, which reports DNA on the gel. Peak #1 collected from SEC shows a prominent band matching the expected molecular weight of nanobody coupled to the docking strand (~15 kDa). Peak #2 lacks the band at the nanobody molecular weight, suggesting that the SEC peak contains only the un-reacted excess of docking oligonucleotide.

3.2. Microfluidic Setup for Exchange DNA-PAINT Experiment

Solution exchange inside the sample chamber was done using a custom-built microfluidics setup, designed and constructed in particular for the Exchange PAINT experiments. The setup allows operation of up to 24 independent inlet channels and is capable of fluid injection/removal with an adjustable flow speed in/out of the experimental chamber.

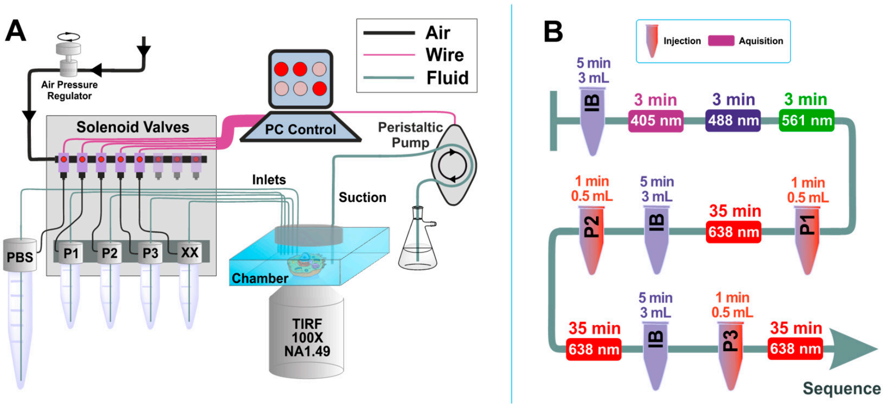

Figure 3. Scheme of custom-built microfluidics setup and Exchange PAINT experiment. (**A**) Microfluidics setup: The setup is controlled by a computer software, which includes both manual and automated operation modes. Maximum number of the input channels is 24 (only 5 channels are shown). The peristaltic pump used to remove the solutions from the chamber is also computer-controlled. (**B**) Typical sequence of actions for the Exchange PAINT experiment. The tube-shape sketches depict the injection of solutions (P1, P2, or P3) or the imaging buffer (IB) (solution volume and injection duration are indicated on top of the objects). Rectangles represent movie acquisition with certain laser excitation (laser wavelength and total acquisition time are indicated inside the rectangle and on top of the rectangle, respectively).

Magnetic solenoid valves (MH1, Festo) were used to turn on and off the air pressure in the channels, which were connected in turn to pressurized tubes. When air pressure is applied to such a tube, a liquid flow is created. Flow speed can be adjusted by changing air pressure using a pressure regulator (MS6, Festo). We used air pressure values in the range of 3–5 psi to generate a gentle flow of solutions. The pressurized air was purified with an air filter (PTA013, Thorlabs). Tygon tubing (VERNAAD04103, VWR) was used to guide the solutions from pressurized tubes to the experimental chamber. Suction was performed by a micro peristaltic pump DC12.0V (Makeblock). For washing, the buffer solution was loaded into a 15 mL test tube (Greiner Bio-One™ 188271, Fisher Scientific). The tube was equipped with a cap for pressurization (FLUIWELL 1C-15, Fluigent, Jena, Germany. The solutions of imager strands P1, P2, and P3 (concentration 2 nM, volume 1 mL) were loaded into 2.0 mL tubes (Micrewtube T341-6T, Simport, Beloeil, QC, Canada), which were then mounted into a holder for four pressurized tubes (FLUIWELL-4C, Fluigent). Both magnetic solenoid valves and peristaltic pumps were operated by a custom-written LabView (National Instruments, München, Germany) routine, which included both manual and automatic operation modes. A custom-built electronic controller served as an interface between the magnetic valves and the computer.

3.3. Super-Resolution Multiplexed DNA-PAINT Images of COS-7 Cells

We performed Exchange PAINT imaging of COS-7 cells stained with nanobodies, each functionalized with a single docking strand. For this purpose, a versatile custom-built optical setup was designed and constructed (see Figure S1). Initially, we checked that all cells to be imaged were triple transfected with the plasmids encoding for the TOM70, GalNacT and H2B fused to

EGFP, mCherry, and mTagBFP, respectively. The signal from each fluorescent protein was first imaged with a wide-field HILO illumination (see Figure 4A1–A3). Afterwards, we sequentially introduced and removed imager strands P1, P2, and P3 as shown in Figure 3B. Each DNA-PAINT movie was acquired during 35 minutes and then analyzed with the Picasso software [10] to obtain the super-resolved images (Figure 4B1–B3). The experiment was designed to monitor three different proteins that are located in very distinct organelles, in order to simplify the evaluation of our Exchange DNA-PAINT images. Clearly, the reconstructed super-resolved DNA-PAINT images (one for each of the imagers P1, P2, and P3) showed the “patterns” expected for the respective organelle, thereby providing additional confirmation of our imaging strategy. For a more informative representation, and to further confirm the specificity of each imager strand, the three super-resolved images (from each P-imager movie) were merged together (Figure 4C1). The result suggests that every “channel” remains clean, without significant unspecific binding events between the different docking-imager partners. The whole imaging cycle for the three target molecules, including imager strand injections, incubations, the removal of solutions and the acquisition of more than 60,000 frames took in total 2–3 h to be completed. The whole procedure worked robustly and provided high quality super-resolved DNA-PAINT images for nearly every imaged cell (selected at the initial wide-field HILO checkup).

In order to evaluate the image quality in a more quantitative manner, we performed a detailed analysis for the average localization accuracy and the actual resolution of the images. For the images presented in Figure 4, the average localization accuracy estimated by NeNa [37] was 19 ± 2 nm (the lowest value was 14 nm, Table S1) and the average resolution, as estimated by Fourier Ring Correlation (FRC) [35], was 27 ± 5 nm (the lowest value was 20 nm, Table S1). The full list of localization accuracies and FRC resolutions obtained for each organelle in each cell in Figure 4 can be found in Table S1 in the Supplementary Information.

Finally, we performed image quality analysis using FRC resolution maps using the SQUIRREL software [39]. The resolution values for different images varied between 26–34 nm. Moreover, we also compared the super-resolved images as obtained by Picasso and by RapidStorm [41]. Interestingly, both tools produce super-resolved images of similar quality (Figure S2).

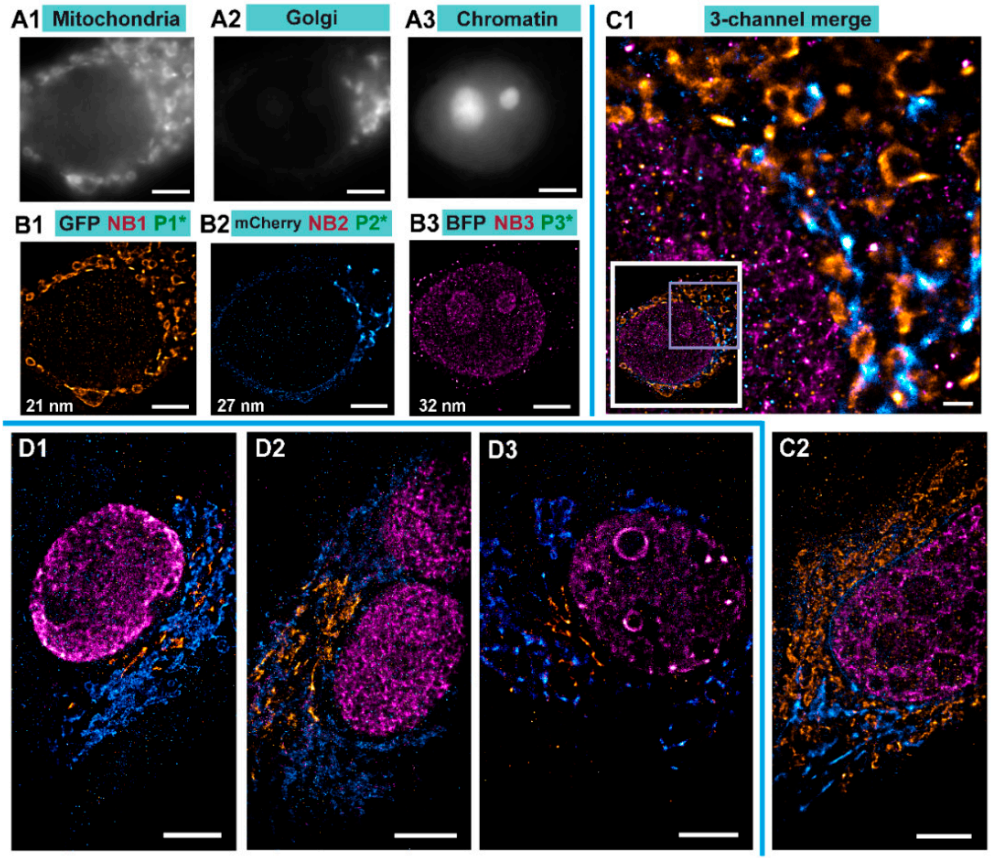

Figure 4. Exchange PAINT imaging. **A1–A3** Diffraction-limited wide-field images of individual target fluorophores: Mitochondria with TOM70-EGFP (**A1**), Golgi with GalNacT-mCherry (**A2**), Chromatin with H2B-mTagBFP (**A3**). (**B1–B3**) Single-channel super-resolution DNA-PAINT images of respective organelles. The number represents Fourier ring correlation (FRC) number for resolution for the respective image. (**C1**) Left bottom inset is the full view of the cell imaged in B with all 3-target Exchange PAINT images merged. Right, zoom of the boxed area I the inset. (**C2**) One more example of Exchange PAINT imaging with the same set of staining as in B and C. (**D1–D3**) Specificity controls were performed by swapping the fluorescent proteins and changing the Golgi marker. Now cells were expressing TOM70-mCherry and GM130-EGFP (a different Golgi marker). All scale bars correspond to 5 µm, except in C1 where the scale bar represents 1 µm.

To assess the effectiveness of our method, we performed several controls. First, the targeted protein GalNacT that we used to detect the Golgi, was changed to GM130 to ensure that the reconstructed organelle is labeled specifically regardless of the target protein used for reporting the Golgi apparatus (Figure 4D1–D3). Additionally, we exchanged the fluorescent proteins we used for targeting the Golgi and the mitochondria by transfecting cells with plasmids encoding for TOM70 fused to mCherry and GM130 fused to EGFP. The same coupled nanobodies were used to reveal those targets. Nb1 (nanobody anti GFP) coupled to P1 docking strand, Nb2 (nanobody anti-mCherry) coupled to P2, and Nb3 (nanobody anti-mTagBFP) coupled to P3. Therefore, in this experiment, the imager P1 revealed the structure of the Golgi apparatus and the imager P2 revealed the mitochondria. Detailed comparison of NeNa and FRC for both cases can be found in Table S1. These control experiments confirmed the efficiency of our system, the specificity of the coupled nanobody, and the interchangeability of the targets. Finally, cells transfected with a single plasmid coding for TOM70-EGFP were immunostained with anti-GFP nanobodies bearing the P1-docking DNA and were imaged with imager P3 under the same conditions as before. We observed very few binding events (i.e., P3 imager binding P1 docking) without showing any recognizable pattern (Figure S3). This extra control suggests a high specificity of the imager to its docking strand. Additionally, unspecific binding (e.g., stickiness of the imager to the glass coverslip or cellular elements) were negligible (Figure S3).

4. Discussion

Conventional antibodies (150 kDa and 12–15 nm in length) are often used for labelling cellular targets in DNA-PAINT imaging [5]. This approach has demonstrated to achieve an impressive spatial resolution [6,7], to a level where the size of the primary and secondary antibody sandwich (with ~25 nm linkage-error) limits its imaging resolution. It has been demonstrated that small camelid single domain antibodies or nanobodies (15 kDa and ~3 nm in length) have the capacity to increase the accuracy of super-resolution microscopy for mapping POIs in a cellular context [8,12]. Recently, a very interesting strategy using a combination of an enzymatic reaction (Sortase) and click chemistry has been used to couple with high efficiencies nanobodies to docking oligos to perform DNA-PAINT [25]. Unfortunately, only few nanobodies are currently available that work efficiently in immunoassay applications. Some of them have a strong affinity and high specificity towards specific fluorescent proteins. In this work, we exploited this property, which makes our method highly versatile since many bio-medical researchers typically have their favorite proteins already fused to fluorescent proteins [42]. Here, we showcase the simultaneous use of three specific nanobodies against the EGFP family (this nanobody also binds to EYFP, Citrine, mVenus, Cerrulean, Emerald EGFP, and more GFP derivatives), mCherry and similar variants (it also binds to mOrange2, tdTomato, dsRed1 & 2, mScarlet-I, and other mRFP derivatives), and finally to mTagBFP (it also recognizes mTagRFP, mTagRFP657, mKate, and mKate2) for DNA-PAINT super-resolution microscopy. As a proof of principle, we used cells expressing three different fluorescent proteins in different organelles. The cells were immunostained with anti EGFP, mCherry, and mTagBFP specific nanobodies, each coupled to a unique and single DNA-docking strand for performing multiplexing Exchange DNA-PAINT with them (Figure 4). We achieved an overall resolution of 20 nm, and an average localization precision of ~14 nm (in the best case, see Table S1), within only 35 min of acquisition time per target. We anticipate that, by further experimental and protocol optimizations, it will be possible to improve the resolution and acquisition time even further. The set of nanobodies presented in this work makes it already possible to investigate three proteins of interest within the same cell, all at diffraction-unlimited resolution, with the enhanced precision provided by the nanobody monovalency (no clustering of target protein) and small size (minimal linkage-error) [13,16]. We hope that our study will motivate other scientists who have their POIs already fused to fluorescent proteins to benefit from this technique.

Supplementary Materials: The following are available online at http://www.mdpi.com/2073-4409/8/1/48/s1. Figure S1. Schematic drawing of custom wide-field Total Internal Reflection (TIRF) optical setup; Figure S2. comparison between Picasso and RapidStorm software packages; Figure S3. control experiment for the nanobody specificity and the stickiness of the imager strand inside fixed COS7 cell transfected with TOM70-GFP-P1*; Figure S4. resolution estimation using Fourier Ring Correlation maps realized by SQUIRREL ImageJ plugin [39]. Table S1. average localization precision (NeNa) and resolution estimation using FRC technique for each of the reconstructed images presented in Figure 4.

Author Contributions: Conceptualization, J.E., R.T. and F.O.; data curation, S.S.-I., N.O., S.I. and R.T.; formal analysis, N.O., S.I. and R.T.; funding acquisition, J.E. and F.O.; investigation, S.S.-I., N.O., S.I., M.E.-M., R.T. and F.O.; methodology, S.S.-I., N.O., S.I., J.E., R.T. and F.O.; project administration, J.E., R.T. and F.O.; supervision, R.T. and F.O.; validation, S.S.-I., N.O., R.T. and F.O.; visualization, S.S.-I., N.O., S.I., R.T. and F.O.; writing—Original draft, S.S.-I., N.O., R.T. and F.O.; writing—review and editing, S.S.-I., N.O., S.I., M.E.-M., J.E., R.T. and F.O.

Funding: F.O. and S.S.-I. were supported by the *Deutsche Forschungsgemeinschaft* (DFG) through the Cluster of Excellence Nanoscale Microscopy and Molecular Physiology of the Brain (CNMPB). N.O. is grateful to the DFG for financial support via project A10 of the SFB 803. JE is grateful to the Deutsche Forschungsgemeinschaft (DFG) for financial support via the Cluster of Excellence and DFG Research Center “Nanoscale Microscopy and Molecular Physiology of the Brain.” R.T. and J.E. are grateful to the DFG for financial support via project A06 of the SFB 860.

Acknowledgments: We thank Mario Raab, Izabela Kaminska and Philip Tinnefeld for the DNA-PAINT training. The authors are grateful to Anna Chizhik for advising during the experiment, Oleksii Nevskyi and Arindam Ghosh for the fruitful discussions, Alexey Chizhik for advice with graphics design, Ingo Gregor for the advice during the construction of the optical setup and Jan Christoph Thiele for the help in design of the microfluidics setup. We thank Dieter Hille and his team from the precision engineering workshop of the Third Institute of Physics, Georg August University. We also thank Markus Schönekeß and his team, in particular Simon Hoelscher, from the electronics workshop Third Institute of Physics, Georg August University. We thank Thomas Schlichthärle and his supervisor Ralf Jungmann for sharing their initial protocol and guidance for conjugation of the nanobody with the docking strand. We thank Selda Kabatas for helping with the molecular models in Figure 2. Finally, we would like to thank Silvio Rizzoli for his support.

Conflicts of Interest: F.O. is a shareholder of NanoTag Biotechnologies GmbH. All other authors declare no conflict of interest.

References

1. Betzig, E.; Patterson, G.H.; Sougrat, R.; Lindwasser, O.W.; Olenych, S.; Bonifacino, J.S.; Davidson, M.W.; Lippincott-Schwartz, J.; Hess, H.F. Imaging Intracellular Fluorescent Proteins at Nanometer Resolution. *Science* **2006**, *313*, 1642–1645. [CrossRef] [PubMed]
2. Heilemann, M.; van de Linde, S.; Schüttpelz, M.; Kasper, R.; Seefeldt, B.; Mukherjee, A.; Tinnefeld, P.; Sauer, M. Subdiffraction-Resolution Fluorescence Imaging with Conventional Fluorescent Probes. *Angew. Chem. Int. Ed.* **2008**, *47*, 6172–6176. [CrossRef] [PubMed]
3. Rust, M.J.; Bates, M.; Zhuang, X. Sub-diffraction-limit imaging by stochastic optical reconstruction microscopy (STORM). *Nat. Methods* **2006**, *3*, 793–796. [CrossRef] [PubMed]
4. Selvin, P.R.; Lougheed, T.; Hoffman, M.T.; Park, H.; Balci, H.; Blehm, B.H.; Toprak, E. Fluorescence Imaging with One-Nanometer Accuracy (FIONA). *CSH Protoc.* **2007**, *10*, pdb.top27. [CrossRef] [PubMed]
5. Jungmann, R.; Steinhauer, C.; Scheible, M.; Kuzyk, A.; Tinnefeld, P.; Simmel, F.C. Single-Molecule Kinetics and Super-Resolution Microscopy by Fluorescence Imaging of Transient Binding on DNA Origami. *Nanoletters* **2010**, *10*, 43. [CrossRef] [PubMed]
6. Raab, M.; Schmied, J.J.; Jusuk, I.; Forthmann, C.; Tinnefeld, P. Fluorescence Microscopy with 6 nm Resolution on DNA Origami. *ChemPhysChem* **2014**, *15*, 2431–2435. [CrossRef]
7. Dai, M.; Jungmann, R.; Yin, P. Optical imaging of individual biomolecules in densely packed clusters. *Nat. Nanotechnol.* **2016**, *11*, 798–807. [CrossRef]
8. Agasti, S.S.; Wang, Y.; Schueder, F.; Sukumar, A.; Jungmann, R.; Yin, P. DNA-barcoded labeling probes for highly multiplexed Exchange-PAINT imaging. *Chem. Sci.* **2017**, *8*, 3080–3091. [CrossRef]
9. Jungmann, R.; Avendaño, M.S.; Woehrstein, J.B.; Dai, M.; Shih, W.M.; Yin, P. Multiplexed 3D cellular super-resolution imaging with DNA-PAINT and Exchange-PAINT. *Nat. Methods* **2014**, *11*, 313. [CrossRef]
10. Schnitzbauer, J.; Strauss, M.T.; Schlichthaerle, T.; Schueder, F.; Jungmann, R. Super-resolution microscopy with DNA-PAINT. *Nat. Protoc.* **2017**, *12*, 1198–1228. [CrossRef]
11. Ries, J.; Kaplan, C.; Platonova, E.; Eghlidi, H.; Ewers, H. A simple, versatile method for GFP-based super-resolution microscopy via nanobodies. *Nat. Methods* **2012**, *9*, 582–584. [CrossRef] [PubMed]
12. Mikhaylova, M.; Cloin, B.M.C.; Finan, K.; van den Berg, R.; Teeuw, J.; Kijanka, M.M.; Sokolowski, M.; Katrukha, E.A.; Maidorn, M.; Opazo, F.; et al. Resolving bundled microtubules using anti-tubulin nanobodies. *Nat. Commun.* **2015**, *6*, 7933. [CrossRef] [PubMed]
13. Maidorn, M.; Rizzoli, S.O.; Opazo, F. Tools and limitations to study the molecular composition of synapses by fluorescence microscopy. *Biochem. J.* **2016**, *473*, 3385–3399. [CrossRef] [PubMed]
14. Wouterlood, F.G. *Cellular Imaging Techniques for Neuroscience and Beyond*; Elsevier/Academic Press: Duivendrecht, The Netherlands, 2012.
15. Schlichthaerle, T.; Ganji, M.; Auer, A.; Wade, O.K.; Jungmann, R. Bacterial-derived antibody binders as small adapters for DNA-PAINT microscopy. *ChemBioChem* **2018**. [CrossRef] [PubMed]
16. Fornasiero, E.F.; Opazo, F. Super-resolution imaging for cell biologists: Concepts, applications, current challenges and developments. *Bioessays* **2015**, *37*, 436–451. [CrossRef] [PubMed]
17. Ellington, A.D.; Szostak, J.W. In vitro selection of RNA molecules that bind specific ligands. *Nature* **1990**, *346*, 818–822. [CrossRef] [PubMed]
18. Ellington, A.D.; Szostak, J.W. Selection in vitro of single-stranded DNA molecules that fold into specific ligand-binding structures. *Nature* **1992**, *355*, 850–852. [CrossRef] [PubMed]

19. Tuerk, C.; Gold, L. Systematic evolution of ligands by exponential enrichment: RNA ligands to bacteriophage T4 DNA polymerase. *Science* **1990**, *249*, 505–510. [CrossRef]
20. Hamers-Casterman, C.; Atarhouch, T.; Muyldermans, S.; Robinson, G.; Hamers, C.; Songa, E.B.; Bendahman, N.; Hamers, R. Naturally occurring antibodies devoid of light chains. *Nature* **1993**, *363*, 446–448. [CrossRef]
21. Opazo, F.; Levy, M.; Byrom, M.; Schäfer, C.; Geisler, C.; Groemer, T.W.; Ellington, A.D.; Rizzoli, S.O. Aptamers as potential tools for super-resolution microscopy. *Nat. Methods* **2012**, *9*, 938–939. [CrossRef]
22. Pleiner, T.; Bates, M.; Trakhanov, S.; Lee, C.-T.; Schliep, J.E.; Chug, H.; Böhning, M.; Stark, H.; Urlaub, H.; Görlich, D. Nanobodies: Site-specific labeling for super-resolution imaging, rapid epitope-mapping and native protein complex isolation. *Elife* **2015**, *4*, e11349. [CrossRef]
23. Strauss, S.; Nickels, P.C.; Strauss, M.T.; Sabinina, V.J.; Ellenberg, J.; Carter, J.D.; Gupta, S.; Janjic, N.; Jungmann, R. Modified aptamers enable quantitative sub-10-nm cellular DNA-PAINT imaging. *Nat. Methods* **2018**, *15*, 685–688. [CrossRef]
24. Kirchhofer, A.; Helma, J.; Schmidthals, K.; Frauer, C.; Cui, S.; Karcher, A.; Pellis, M.; Muyldermans, S.; Casas-Delucchi, C.S.; Cardoso, M.C.; et al. Modulation of protein properties in living cells using nanobodies. *Nat. Struct. Mol. Biol.* **2010**, *17*, 133–138. [CrossRef] [PubMed]
25. Fabricius, V.; Lefèbre, J.; Geertsema, H.; Marino, S.F.; Ewers, H. C-terminal labeling of nanobodies for DNA-PAINT dual-color imaging. *J. Phys. D Appl. Phys.* **2018**, *51*, 474005. [CrossRef]
26. Cormack, B.P.; Valdivia, R.H.; Falkow, S. FACS-optimized mutants of the green fluorescent protein (GFP). *Gene* **1996**, *173*, 33–38. [CrossRef]
27. Shaner, N.C.; Campbell, R.E.; Steinbach, P.A.; Giepmans, B.N.G.; Palmer, A.E.; Tsien, R.Y. Improved monomeric red, orange and yellow fluorescent proteins derived from Discosoma sp. red fluorescent protein. *Nat. Biotechnol.* **2004**, *22*, 1567–1572. [CrossRef] [PubMed]
28. Subach, O.M.; Gundorov, I.S.; Yoshimura, M.; Subach, F.V.; Zhang, J.; Grüenwald, D.; Souslova, E.A.; Chudakov, D.M.; Verkhusha, V.V. Conversion of Red Fluorescent Protein into a Bright Blue Probe. *Chem. Biol.* **2008**, *15*, 1116–1124. [CrossRef]
29. Yofe, I.; Weill, U.; Meurer, M.; Chuartzman, S.; Zalckvar, E.; Goldman, O.; Ben-Dor, S.; Schütze, C.; Wiedemann, N.; Knop, M.; et al. One library to make them all: Streamlining the creation of yeast libraries via a SWAp-Tag strategy. *Nat. Methods* **2016**, *13*, 371–378. [CrossRef] [PubMed]
30. Xiao, Y.-L.; Redman, J.C.; Monaghan, E.L.; Zhuang, J.; Underwood, B.A.; Moskal, W.A.; Wang, W.; Wu, H.C.; Town, C.D. High throughput generation of promoter reporter (GFP) transgenic lines of low expressing genes in Arabidopsis and analysis of their expression patterns. *Plant Methods* **2010**, *6*, 18. [CrossRef] [PubMed]
31. Gonzalez-Serricchio, A.S.; Sternberg, P.W. Visualization of C. elegans transgenic arrays by GFP. *BMC Genet.* **2006**, *7*, 36. [CrossRef] [PubMed]
32. Fatima, R. Drosophila Dynein Intermediate Chain Gene, Dic61B, Is Required for Spermatogenesis. *PLoS ONE* **2011**, *6*, e27822. [CrossRef]
33. Kawamoto, S.; Niwa, H.; Tashiro, F.; Sano, S.; Kondoh, G.; Takeda, J.; Tabayashi, K.; Miyazaki, J. A novel reporter mouse strain that expresses enhanced green fluorescent protein upon Cre-mediated recombination. *FEBS Lett.* **2000**, *470*, 263–268. [CrossRef]
34. Schlichthaerle, T.; Eklund, A.S.; Schueder, F.; Strauss, M.T.; Tiede, C.; Curd, A.; Ries, J.; Peckham, M.; Tomlinson, D.C.; Jungmann, R. Site-Specific Labeling of Affimers for DNA-PAINT Microscopy. *Angew. Chem. Int. Ed.* **2018**, *57*, 11060–11063. [CrossRef] [PubMed]
35. Nieuwenhuizen, R.P.J.; Lidke, K.A.; Bates, M.; Puig, D.L.; Grünwald, D.; Stallinga, S.; Rieger, B. Measuring image resolution in optical nanoscopy. *Nat. Methods* **2013**, *10*, 557–562. [CrossRef] [PubMed]
36. Schindelin, J.; Arganda-Carreras, I.; Frise, E.; Kaynig, V.; Longair, M.; Pietzsch, T.; Preibisch, S.; Rueden, C.; Saalfeld, S.; Schmid, B.; et al. Fiji: An open-source platform for biological-image analysis. *Nat. Methods* **2012**, *9*, 676–682. [CrossRef] [PubMed]
37. Endesfelder, U.; Malkusch, S.; Fricke, F.; Heilemann, M. A simple method to estimate the average localization precision of a single-molecule localization microscopy experiment. *Histochem. Cell Biol.* **2014**, *141*, 629–638. [CrossRef] [PubMed]
38. Burri, O.; Herbert, A. Fourier Ring Correlation, Fire. *Image J. Plugin* **2016**.
39. Culley, S.; Albrecht, D.; Jacobs, C.; Pereira, P.M.; Leterrier, C.; Mercer, J.; Henriques, R. Quantitative mapping and minimization of super-resolution optical imaging artifacts. *Nat. Methods* **2018**, *15*, 263–266. [CrossRef]

40. Agard, N.J.; Prescher, J.A.; Bertozzi, C.R. A Strain-Promoted [3 + 2] Azide−Alkyne Cycloaddition for Covalent Modification of Biomolecules in Living Systems. *J. Am. Chem. Soc.* **2004**, *126*, 15046–15047. [CrossRef]
41. Wolter, S.; Löschberger, A.; Holm, T.; Aufmkolk, S.; Dabauvalle, M.-C.; van de Linde, S.; Sauer, M. rapidSTORM: Accurate, fast open-source software for localization microscopy. *Nat. Methods* **2012**, *9*, 1040–1041. [CrossRef]
42. Day, R.N.; Davidson, M.W. The fluorescent protein palette: Tools for cellular imaging. *Chem. Soc. Rev.* **2009**, *38*, 2887–2921. [CrossRef] [PubMed]

Supplementary Materials

Nanobody-based multi-target Exchange DNA-PAINT with 20 nm resolution using standard fluorescent proteins

Shama Sograte-Idrissi[1,2,4,†], Nazar Oleksiievets[3,†], Sebastian Isbaner[3], Mariana Eggert-Martinez[1,2,4], Jörg Enderlein[3], Roman Tsukanov[3,*], Felipe Opazo[1,2,*]

[1]Institute of Neuro- and Sensory Physiology, University Medical Center Göttingen, 37073 Göttingen, Germany

[2]Center for Biostructural Imaging of Neurodegeneration (BIN), University of Göttingen Medical Center, 37075 Göttingen, Germany

[3]Third Institute of Physics – Biophysics, Georg August University, 37077 Göttingen, Germany

[4] International Max Planck Research School for Molecular Biology, Göttingen, Germany

[†]These authors contribute equality to this work

[*]**Corresponding authors:** fopazo@gwdg.de, roman.tsukanov@phys.uni-goettingen.de

Running title: Multicolor DNA-PAINT using nanobodies

Keywords: Nanobodies, Super-resolution microscopy, multi-color imaging, TIRF, microfluidics, DNA-PAINT, molecular localization, sdAb, GFP, mCherry, mtagBFP, multiplexing

Custom-built optical setup description

Measurements were performed on an in-house-built optical setup. In brief, the excitation part included four lasers: 405 nm (CUBE 405-100C, Coherent), 488 nm (PhoxX+ 488-100, Omicron), 561 nm (MGL-FN-561-100, Changchun), and 638 nm (PhoxX+ 638-150, Omicron). Manual shutters were used to easily switch between excitation lasers. The lasers were combined into the same optical path using dichroic mirrors DM1 (BrightLine DiO2-R561, Semrock), DM2 (BrightLine FF495-Di03, Semrock), and DM3 (zt405 RDC, Chroma). Then, the laser beams were coupled into a single-mode fiber (P1-460B-FC-2, Thorlabs) with typical coupling efficiency of 40-50%. After exiting the fiber, the beam was collimated and expanded by a factor of 3.6X using telescopic lenses. In order to achieve wide-field illumination, lens L1 (AC508-200-A-ML, Thorlabs) focused collimated laser beam on the back focal plane of the high-NA objective (UAPON 100x oil, 1.49 NA, Olympus). In order to switch between Epi-, HILO-, or TIRF-illumination schemes, the translation stage TS (LNR50M, Thorlabs) was used to mechanically shift the corresponding optical elements. The translation XY stage (M-406, Newport) ensured smooth and stable sample movement during the scan.

A separate translation stage with a differential micrometer screw (DRV3, Thorlabs) was holding the objective and was used for focusing. The emitted fluorescence was separated from the excitation laser using the multi-band dichroic mirror DM4 (Di03 R405/488/532/635, Semrock). Lens L2 (AC254-200-A-ML, Thorlabs) was used as a tube lens. An adjustable slit (SP60, OWIS) was positioned in the image plane and was used to limit the field of view. The multi-band filter BP1 (ZET488/561/635m, Chroma) was used to filter out laser remains in the detection path. Lenses L3 (AC254-100-A, Thorlabs) and L4 (AC508-150-A-ML, Thorlabs) were used to transfer the image plane from the slit to the EMCCD camera (iXon Ultra 897, Andor), thereby providing rectangular space for wavelength-based splitting of the emission light into two or three emission channels according to the experimental requirements. For this purpose, the dichroic mirrors DM5 (Chroma 550 LPXR) and DM6 (FF648-Di01, Semrock) were positioned on magnetic bases MB (KB50/M, Thorlabs). For each channel, additional band-pass filters were used: BP2 (BrightLine FF 445/20, Semrock) for the blue channel, BP3 (BrightLine FF 536/40, Semrock) for the green channel, and BP4 (BrightLine HC 692/40, Semrock) for the red channel. The overall magnification factor of the optical setup was 166.6X, the pixel size was 103.5 nm x 103.5 nm and the full field of view was 53 µm X 53 µm. Focus stability was achieved by robust construction of the custom microscope body, tightly fixing the 8-well chamber (155411PK, ThermoFisher Scientific) to the sample holder and keeping the temperature in the room stable.

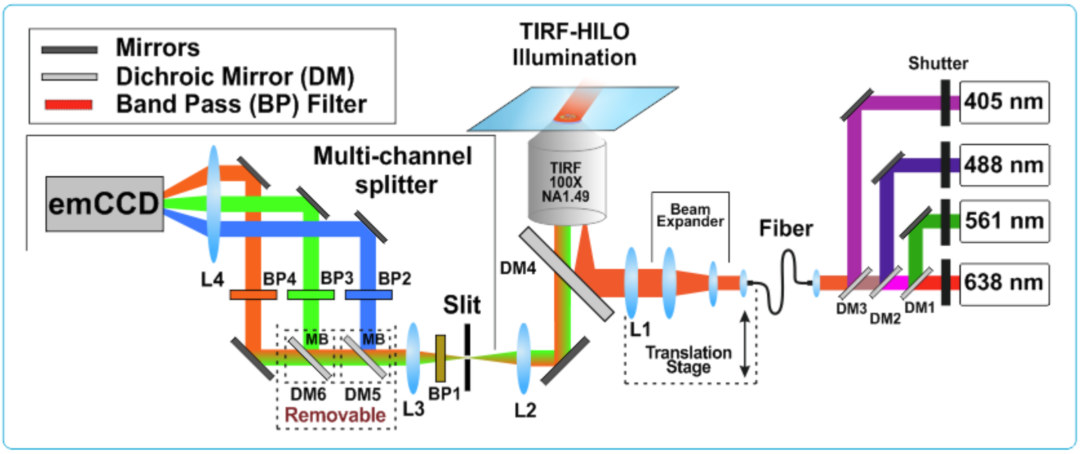

Figure S1. Schematic drawing of custom wide-field TIRF optical setup. The excitation is equipped with four lasers and allows excitation of fluorophores on broad spectral range. Multi-channel detection enables simultaneous imaging of fluorophores with different emission spectrum on the same CCD camera. Number of emission channels can be easily switched between one, two and three channels by removing the dichroic mirrors DM5 or/and DM6. The size of region of interest is controlled by a slit.

Localization accuracy and resolution estimations

Detailed numbers as for each reconstructed image resolution are listed in the Table S1.

Cell name	**Organelle, protein, docking**	**NeNa, nm**	**FRC, nm**
Fig 4, C1	Mito GFP P1*	20	21
	Golgi RFP P2*	18	27
	Nucleus BFP P3*	22	32
Fig 4, C2	Mito GFP P1*	22	34
	Golgi RFP P2*	16	23
	Nucleus BFP P3*	23	34
Fig 4, C3	Mito GFP P1*	19	38
	Golgi RFP P2*	16	28
	Nucleus BFP P3*	22	31

Cell name	**Organelle, protein, docking**	**NeNa, nm**	**FRC, nm**
Fig 4, D1	Mito RFP P2*	19	22
	Golgi GFP P1*	18	24
	Nucleus BFP P3*	23	38
Fig 4, D2	Mito RFP P2*	20	28
	Golgi GFP P1*	19	20
	Nucleus BFP P3*	19	24
Fig 4, D3	Mito RFP P2*	14	24
	Golgi GFP P1*	18	27
	Nucleus BFP P3*	17	26

Table S1. Average localization precision (NeNa) and resolution estimation using FRC technique for each of the reconstructed images presented in Figure 4. Cell names appear according to the order in Figure 4.

DNA-PAINT analysis toolkits comparison: Picasso vs. Rapidstorm

Verification of Picasso analysis was done by analysing same image with RapidStorm.[1] Recorded DNA-PAINT movie was loaded into RapidStorm. Blinking event were identified by setting the intensity threshold to 60 % of a total brightness. Resolution (both X and Y direction) was set to 10 nm/pixel. The comparison between reconstructed images shown on Figure S2. The achieved resolution was estimating by exporting the localization file output and then running it into SQUIRREL ImageJ plugin[2]. Resulting numbers and comparison to Picasso output shown on Table S1. We saw good agreement Picasso and RapidStorm results.

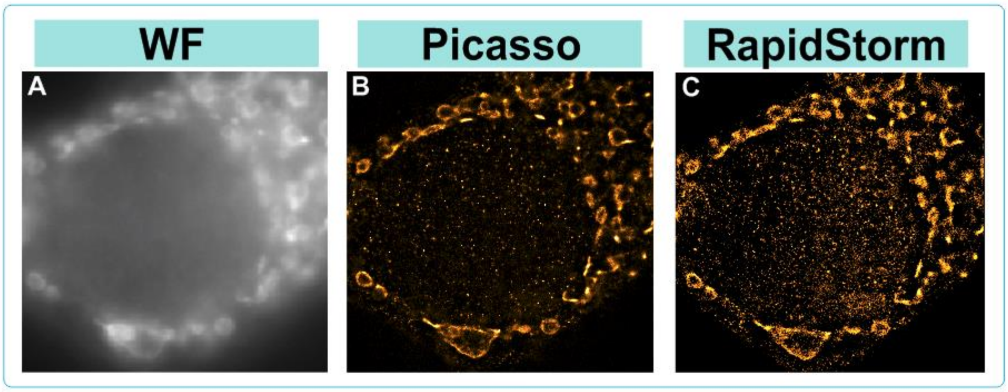

Figure S2. Comparison between Picasso and RapidStorm software packages. (**A**) Wide-field (WF) diffraction-limited image of GFP protein. (**B**) Reconstructed super-resolution image obtained with Picasso software. (**C**) Reconstructed super-resolution image obtained with Picasso software.

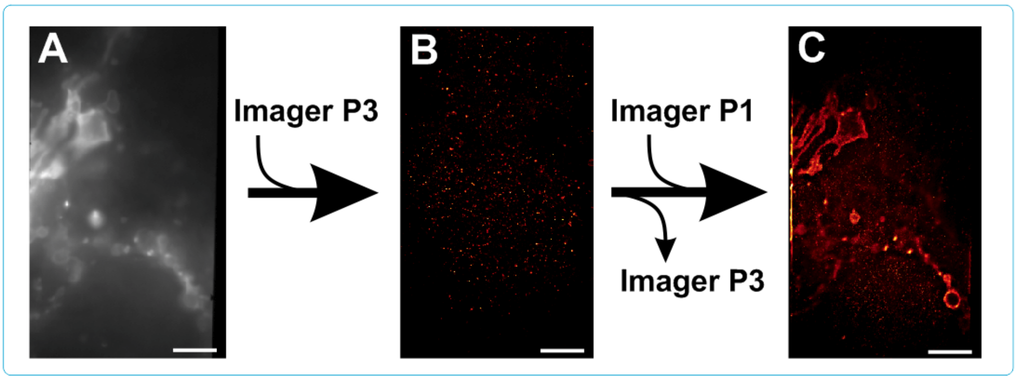

Figure S3. Control experiment for the nanobody specificity and the stickiness of the imager strand inside fixed COS7 cell transfected with TOM70-GFP-P1*. (**A**) wide-field image of TOM70 GFP. (**B**) Super-resolution image from a DNA-PAINT movie taken in presence of P3 imager. Only few random localization events detected in presence of the imager P3 (**C**) Super-resolution image of the same region of interest, taken in presence of P1 imager (after washing/removing the imager P3).

DNA-PAINT Fourier Ring Correlation resolution maps

For NanoJ-SQUIRREL analysis stack of two statistically independent super-resolution images of the same structure were reconstructed using Picasso and RapidStorm software. Then using 'Calculate FRC Map' feature (block per pixel value 25 and pixel size 10 nm) the FRC map was made and overlaid with respective super-resolution image. Average FRC resolution value was obtained by finding the mean value from the area with high localization density. For this purpose, obtained super-resolution image was cropped and whole procedure was repeated for this area. The average resolutions obtained are 26 nm for Picasso and 30 nm for RapidStorm.

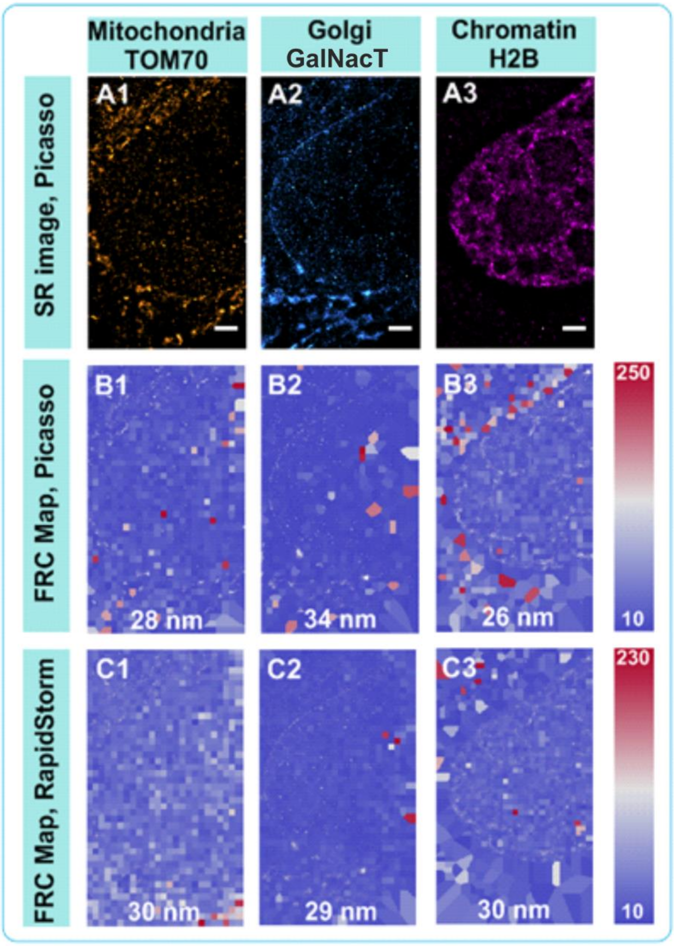

Figure S4. Resolution estimation using Fourier Ring Correlation maps realized by SQUIRREL ImageJ plugin[2]. Comparison between Picasso and RapidStorm analysis tools. (A1-3) Super-resolution DNA-PAINT images of COS7 cell organelles reconstructed by Picasso. (B1-3) FRC map overlaid with the corresponding super-resolution images, as reconstructed by Picasso toolkit. (C1-3) FRC map overlaid with the corresponding super-resolution images, as reconstructed by RapidStorm toolkit. The numbers on the images represent the resolution averaged over the object region. The colors on B and C indicated resolution, according to scale shown on the right-hand side.

Bibliography

1. Wolter, S. *et al.* rapidSTORM: accurate, fast open-source software for localization microscopy. *Nat. Methods* **9,** 1040–1041 (2012).
2. Culley, S. *et al.* Quantitative mapping and minimization of super-resolution optical imaging artifacts. *Nat. Methods* **15,** 263–266 (2018).

3

WIDE-FIELD FLUORESCENCE LIFETIME IMAGING OF SINGLE MOLECULES

3.1 MANUSCRIPT: WIDE-FIELD FLUORESCENCE LIFETIME IMAGING OF SINGLE MOLECULES

The original research article entitled: " **Nazar Oleksiievets**[1], Jan Christoph Thiele[1], Andre Weber, Ingo Gregor, Oleksii Nevskyi, Sebastian Isbaner, Roman Tsukanov, Jörg Enderlein, Wide-Field Fluorescence Lifetime Imaging of Single Molecules, Journal of Physical Chemistry A, 2020, 124, 17, 3494-3500" was published. Nazar Oleksiievets performed all single-molecule lifetime experiments, assisted in data analysis and co-wrote the manuscript.

Reproduced with permission, copyright 2020 American Chemical Society.

The published research article is currently available at `https://pubs.acs.org/doi/10.1021/acs.jpca.0c01513`

---

[1] These authors contributed equally to this work

THE JOURNAL OF
PHYSICAL CHEMISTRY A

pubs.acs.org/JPCA Article

Wide-Field Fluorescence Lifetime Imaging of Single Molecules

Published as part of The Journal of Physical Chemistry virtual special issue "Time-Resolved Microscopy".

Nazar Oleksiievets,[§] Jan Christoph Thiele,[§] André Weber, Ingo Gregor, Oleksii Nevskyi, Sebastian Isbaner, Roman Tsukanov,* and Jörg Enderlein*

Cite This: *J. Phys. Chem. A* 2020, 124, 3494–3500 Read Online

ACCESS | Metrics & More | Article Recommendations | Supporting Information

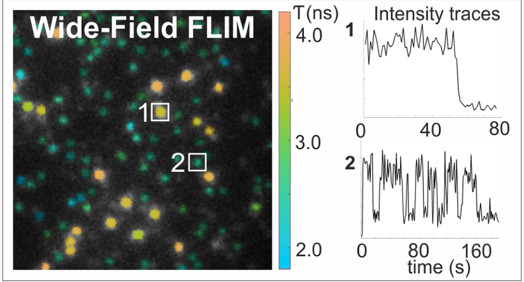

ABSTRACT: Fluorescence lifetime imaging (FLIM) has become an important microscopy technique in bioimaging. The two most important of its applications are lifetime-multiplexing for imaging many different structures in parallel, and lifetime-based measurements of Förster resonance energy transfer. There are two principal FLIM techniques, one based on confocal-laser scanning microscopy (CLSM) and time-correlated single-photon counting (TCSPC) and the other based on wide-field microscopy and phase fluorometry. Although the first approach (CLSM-TCSPC) assures high sensitivity and allows one to detect single molecules, it is slow and has a small photon yield. The second allows, in principal, high frame rates (by 2–3 orders of magnitude faster than CLSM), but it suffers from low sensitivity, which precludes its application for single-molecule imaging. Here, we demonstrate that a novel wide-field TCSPC camera (LINCam25, Photonscore GmbH) can be successfully used for single-molecule FLIM, although its quantum yield of detection in the red spectral region is only ~5%. This is due to the virtually absent background and readout noise of the camera, assuring high signal-to-noise ratio even at low detection efficiency. We performed single-molecule FLIM of different red fluorophores, and we use the lifetime information for successfully distinguishing between different molecular species. Finally, we demonstrate single-molecule metal-induced energy transfer (MIET) imaging which is a first step for three-dimensional single-molecule localization microscopy (SMLM) with nanometer resolution.

■ INTRODUCTION

Fluorescence microscopy has revolutionized our understanding of biological processes. One of its variants is fluorescence lifetime imaging (FLIM), which has become an important microscopy technique in medicine and biology.[1−3] The two most important applications of FLIM are (i) distinguishing between different fluorophores with similar emission spectra based on their fluorescence lifetime (thus allowing multiplexing),[4] and (ii) Förster resonance energy transfer imaging via measuring donor lifetime.[5,6] One of the big technical challenges of FLIM is to achieve high image acquisition speed without compromising sensitivity. There are two fundamentally different technical approaches to FLIM. The first approach is based on confocal laser-scanning microscopy (CLSM), where one scans a field of viewpoint by point and usually measures, at each scan position, the fluorescence lifetime (and intensity) by time-correlated single-photon counting (TCSPC).[7] This assures the highest sensitivity, but for the price of reduced image acquisition speed. The second approach uses camera-based phase-fluorometry,[8,9] which allows fast image acquisition, but for the price of tremendously reduced sensitivity. For example, wide-field phase-fluorometry is much too insensitive for being capable for single-molecule imaging. Only recently, new single-photon counting wide-field detectors have been developed, see, e.g., refs 10 and 11, but they are still in their infancy and are not widely available. Other more particular FLIM techniques are based on gated optical image intensifiers,[12] electro-optical modulators,[13] electron multiplying microchannel plates (MCP),[14,15] or wide-field time-gated SPAD arrays.[16] However, all these approaches are currently too insensitive for genuine single-molecule applications.

Here, we investigate the applicability of a novel, commercially available wide-field single-photon counting camera (LINCam25, Photonscore GmbH, a spin off from the Leibniz Institute for Neurobiology, Magdeburg, Germany) for FLIM with single molecule sensitivity, see Figure 1A. The TCSPC-based lifetime camera is designed and optimized for photon detection from the UV to the visible spectrum. It

Received: February 21, 2020
Revised: April 6, 2020
Published: April 7, 2020

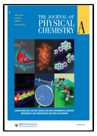

ACS Publications

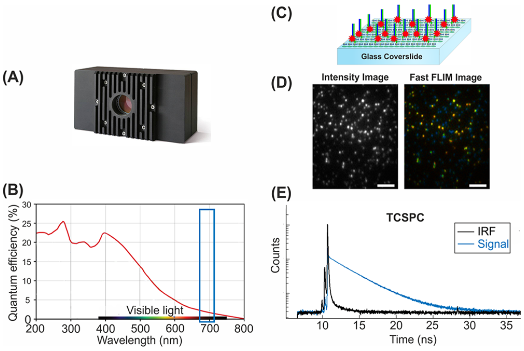

Figure 1. Wide-field FLIM with single-molecule sensitivity using the LINCam25. (A) Schematic of the lifetime-measuring camera LINCam25. The picture was provided by Photonscore GmbH, and is used with permission. (B) Typical quantum efficiency of LINCam25. Used with permission by Photonscore GmbH. The blue rectangle indicates the spectral range of emission of the fluorophores used in the current investigation. (C) DNA-assisted surface immobilization of the fluorophores. The double-stranded DNA was attached to the glass coverslip via biotin−avidin chemistry. (D) Conventional intensity and lifetime images of single molecules with different lifetimes. The scale bar is 5 μm. (E) Sample TCSPC curve of one of the red fluorophores together with the measured instrument response function (IRF) of the optical setup.

employs a micro-channel-plate photo-multiplier tube (MCP-PMT) and uses a capacity-coupled imaging technique (charge image) combined with a charge division anode for positional readout.[15] The detector is equipped with a multialkali photocathode optimized for the UV spectral region. However, its quantum efficiency of detection drops significantly toward the red spectral region: from the ~20% in the blue spectral region to ~5% in the red spectral region, see Figure 1B. Nonetheless, due its virtually absent noise and dark counts, we demonstrate here that one can successfully use the LINCam25 for FLIM with single-molecule sensitivity, even in the red spectral region. To demonstrate this, we perform wide-field FLIM of three widely used fluorophores, Cy5, Atto 655, and Atto 647N, which have similar emission spectra but differ in their lifetimes. For FLIM, the fluorophores are conjugated against DNA molecules and immobilized on a glass surface; see Figure 1C. FLIM results for the different samples are presented in Figure 1D.

We determine fluorescence lifetimes of individual molecules by fitting the recorded TCSPC data on a molecule-by-molecule basis; see Figure 1E. Using these fitted lifetime values, we successfully distinguish between different molecular species in a mixed sample of all three fluorophores. Finally, we apply the LINCam25 for FLIM of metal-induced energy transfer (MIET),[17] which allows us to determine the axial position of individual molecules above a surface,[18−24] which is a first step of applying the LINCam25 for three-dimensional single-molecule localization microscopy (SMLM).[25−30]

■ METHODS

LINCam25. The LINCam25 is a system where the light sensing element is a microchannel-plate based photomultiplier tube (MCP-PMT) equipped with a photocathode for visible light (S20BB). The fast reaction time of the MCP in combination with a time-to-amplitude converter coupled with a dedicated analog-to-digital converter (ADC) makes this camera suitable for TCSPC with a temporal resolution below 50 ps over the whole field of view. A capacity-coupled imaging technique (charge image) combined with a charge division anode is employed for positional readout. The position of an incident photon is reconstructed by means of an artificial neural network's (ANN's) computation model as precise as 20 μm over the active detection area of o.d. 25 mm.[15] Therefore, the resulting image is comparable to that of a conventional megapixel CCD camera and allows for TCSPC-FLIM with a regular fluorescence wide-field microscope.[31]

Data Acquisition. Experiments were performed with custom-built wide-field microscope. TIR illumination was done with an average laser power of 10−20 W/cm^2. Neutral density filters were employed for fine adjustment of laser power. A supplemental emCCD camera with a much higher quantum efficiency of detection than the LINCam25 was used for focusing. Typical acquisition times per image were between 3 to 5 min. Images of several regions of interest (3−6) for each sample were acquired. The image acquisition software was provided by Photonscore. A preliminary analysis of lifetime images was performed by the Photonscore Capture software. The further single-molecule lifetimes analysis was done using a custom-written MATLAB routine. All experiments were carried out at a constant temperature of 22 ± 1 °C, which was crucial for the mechanical stability of the optical setup.

Sample Preparation. Glass coverslips were sonicated in 1 M KOH for 15 min and then rinsed with doubly distilled water (DDH2O) and dried using air flow. Four-wells silicone inserts (Ibidi 80469, Germany) were attached to the coverslip to form four measurement chambers, therefore allowing for a convenient workflow through the preparation of different molecular samples in each of the four chambers on the same coverslip. BSA−biotin (A8549, Sigma-Aldrich) was diluted in buffer A to a concentration of 0.5 mg/mL and added to the chambers overnight at 4 °C. The next day, the chambers were flushed with buffer A for at least 3 times the volume of a chamber. Neutravidin (31000, Thermo Fisher Scientific) was diluted in buffer A to a concentration of 0.5 mg/mL and then added to one chamber for 5 min. Next, the chamber was rinsed for at least 3 times. DNA-fluorophore molecules were immobilized to the surface using biotin−avidin chemistry. We designed the double-stranded DNA molecules as follows: Primary single-stranded DNA (strand 1) was biotinylated at its 5′ end, while the complementary DNA (strand 2) was labeled at its 3′ end with a single fluorophore (either Cy5, Atto 655, or Atto 647N), see Table S2 in the Supporting Information for the DNA sequences. This ensured that the fluorophores are more photostable and less blinking than without DNA. The fluorophore is attached close to the surface anchor of the DNA. This design is similar to one used in DNA-PAINT.[29] The two DNA strands were hybridized at high concentration (200 nM) using the following protocol: The mixture of the two DNA strands was heated to 94 °C in the annealing buffer for 5 min and then gradually cooled to room temperature within 30 min. Then, the resulting dsDNA solution was diluted by about 10000× to reach a single-molecule concentration before being added to the experimental chamber. After 5−10 min incubation time, the chamber was rinsed with imaging buffer by exchanging the liquid in the chamber (~80 μL) for at least 3 times. For the mixed fluorophores sample, we diluted the stock solutions by the same factor as for the pure

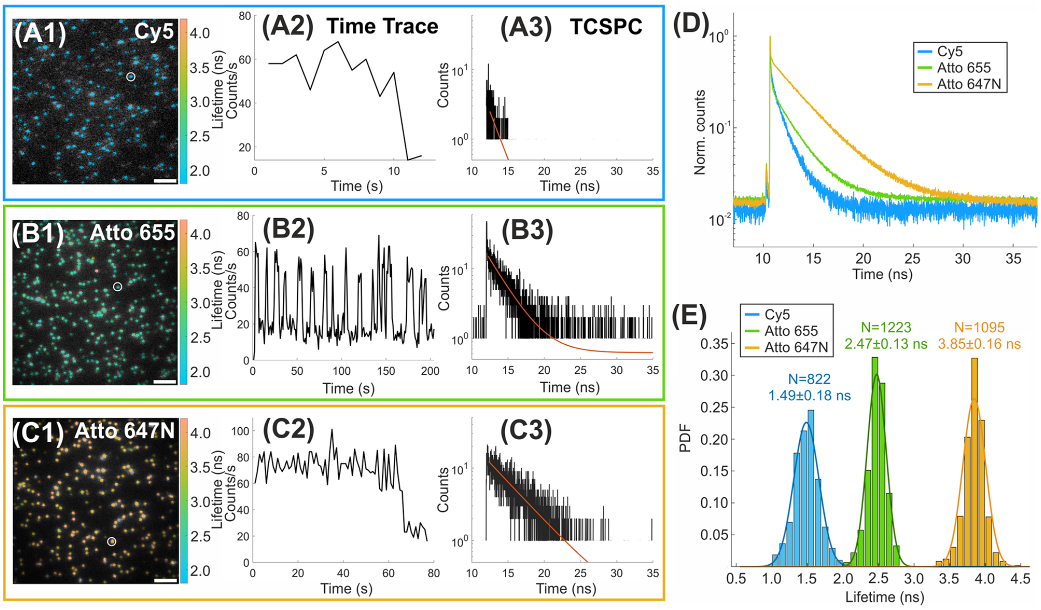

Figure 2. Lifetime imaging of surface-immobilized single molecules. Different types of fluorophores were imaged separately. The scale bar is 5 μm. Images of the following fluorophores are shown: (A1) Cy3, (B1) Atto 655, and (C1) Atto 647N. Colors represent lifetime values. The lifetime scale is shown on the right-hand side of the image. White circles indicate molecules that were chosen for the exemplary intensity time traces (A2, B2, and C2) and corresponding TCSPC curves (A3, B3, and C3). (D) TCSPC curves obtained by adding all single-molecule data of the same type. (E) Probability density function (PDF) of lifetime values of each fluorophore type with the correspondent single-Gaussian fit. The average lifetime and standard deviation of the fit appear next to each peak, as well as the number of molecules used in each lifetime histogram.

fluorophore samples and mixed in the final solution with a stoichiometry of Atto 647N:Atto 655:Cy5 = 1:3:10.

Buffer Solutions. The following buffer solutions were used: DNA annealing buffer included 10 mM Tris, pH 8.0, 1 mM EDTA, and 100 mM NaCl. Buffer A (used for surface immobilization) included 10 mM Tris, pH 8.0, and 50 mM NaCl. DNA storage buffer (B4) included 10 mM Tris, pH 8.0, and 1 mM EDTA. As imaging buffer solutions, we used either B4 with NaCl 500 mM, or alternatively GLOX buffer (enzymatic oxygen scavenging system) consisting of glucose oxidase 0.5 mg/mL, catalase 40 μg/mL, and glucose 10% w/v in PBS pH 7.4. The GLOX buffer was crucial for enhancing photostability and for increasing the number of emitted photons, especially for Cy5.

Data Analysis. Single-molecule lifetimes analysis was performed using a custom-written MATLAB program. First, an intensity image was generated from the raw photon data rejecting photons arriving outside a 10 ns time gate starting 0.25 ns after maximum intensity. This image was used for identifying single molecules using a wavelet algorithm as described in ref 32. Intensity time traces and TCSPC curves for each identified molecule were extracted from the raw data using a time binning of 1 s. This was done by collecting all photons within a 3 × 3 pixel region around the center position of each molecule (approximately 1.4σ_{PSF}). On the basis of the intensity time traces, a on/off-state-detection was applied (see Supporting Information for details), and a TCSPC curve was accumulated, including only time points where the molecule was in its fluorescent on-state. Fluorescence lifetime values were determined by fitting the tail (starting 0.2 ns after maximum) of the TCSPC curves with a monoexponential decay by minimizing the negative log-likelihood function with a Nelder−Mead simplex algorithm.[22,33] TCSPC curves with less than 100 photons in the tail, or with a χ^2 of the fit below 0.9 or above 1.1 were rejected. FLIM images were generated by coloring each identified molecule according to its lifetime fit, while the pixel brightness reflects the true pixel intensity. The lifetime histograms were fitted with a single Gaussian or, for the mixed sample, a sum of three Gaussians, using again a Nelder−Mead simplex algorithm.

■ RESULTS

Single-Molecule FLIM. Three distinct samples of surface-immobilized molecules of Cy5, Atto 655, and Atto 647N were prepared, using a DNA-assisted strategy for surface immobilization. This created a favorable photochemical environment for the fluorophores, and allowed surface immobilization with highly controllable coverage density. The latter was achieved by diluting a stock solution of molecules to concentrations of 100−500 pM, and by varying the incubation time of these solutions in the measurement chamber, see Supporting Information for more details. Exemplary lifetime images are shown in Figure 2, parts A1, B1, and C1. In order to enhance brightness and photostability of the fluorophores, we added oxygen-scavenger (GLOX, see Supporting Information for details) to the imaging buffer. Exemplary intensity time traces for single molecules are shown in Figure 2, parts A2, B2, and C2. More single molecule trajectories and photon number distributions can be found in the Supporting Information. For our experimental conditions, photobleaching of Cy5 occurred within a few seconds, while the emission showed no blinking until bleaching. Atto 655 kept on emitting for hundreds of seconds before photobleaching, while exhibiting blinking with a characteristic on-time of 8.2 s and an off-time of 10.5 s. This was revealed by an on/off-state-detection analysis; see the Supporting Information for details. The relatively slow blinking behavior might be explained by the low excitation laser power and also the oxygen-depleted environment in the imaging buffer containing GLOX.[34] Atto 647N showed the highest emission intensity and remained emitting for hundreds of seconds before photobleaching, without any discernible blinking. Lifetime values for identified single molecules were fitted with an exponential function, and the resulting single-molecule lifetime values were histogrammed; see Figure 2, parts A3, B3, and C3. We did also add all photons from all detected single molecules into one cumulative TCSPC curve, as shown in Figure 2D. From the single-molecule lifetime histograms, we extracted average lifetime values and the standard deviations; see Figure 2E.

In order to reduce the statistical uncertainty, several (3−5) regions of interest were combined together. All the peaks were fitted with a single Gaussian function. The following average lifetime values were determined: Cy5, 1.49 ± 0.18 ns; Atto 655, 2.47 ± 0.13 ns; and Atto 647N, 3.85 ± 0.16 ns. The errors are the standard deviation. As expected, the lifetime values of DNA-bound fluorophores are longer those for free fluorophores, due to the interaction between the fluorophores and the DNA.[35]

FLIM of Single Molecules in a Mixed Sample. The distinct fluorescence lifetimes of our three fluorophores can be used to identify them in mixed samples. We demonstrate this by performing FLIM measurement on a sample containing all three fluorophores. To mimic a common bioimaging situation with high labeling density, we prepared a sample with rather high surface coverage. A typical situation is shown in Figure 3A. For the well-separated lifetime values of our three fluorophores, the identification of each of them on a molecule-by-molecule basis was straightforward. However, the determination of correct lifetime values for each molecule was not trivial due to the frequently occurring partial overlap of the image of one molecule with those of neighboring molecules. To overcome this problem, we employed a on/off-state-detection algorithm; for details, see Supporting Information and Figure S8. It diminishes contributions from neighboring molecules and decreases the number of background photons by taking into account only photons emitted by a fluorophore in its on-state; see Supporting Information for the details. These sorted photons were used for building decay curves for each single molecule, providing better separation between peaks in the lifetime histograms, see Figure 3B. For a detailed comparison of the obtained lifetimes in pure and mixed fluorophores samples, see Figure S6 in the Supporting Information.

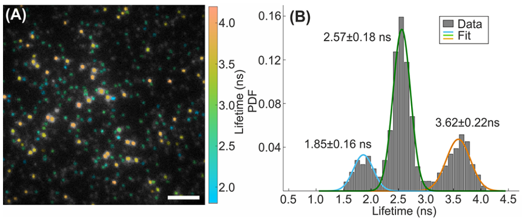

Figure 3. FLIM image of a mixture of Cy5, Atto 655, and Atto 647N fluorophores immobilized to the surface. (A) Exemplary lifetime image. Pseudo colors depict the lifetime values. The scale of lifetimes appears on the right-hand side of the image. The scale bar is 5 μm. (B) Lifetime histogram of the mixed sample and the corresponding three peak Gaussian fit. The different components of the Gaussian fit are shown in different colors. The lifetime histogram includes data from four images. The average lifetime values and the standard deviations of the fit appear next to each peak. The total number of molecules included in the histogram is 1573.

Application of FLIM to Metal-Induced Energy Transfer (MIET). One attractive application of FLIM is MIET,[23] which employs the distance-dependent quenching of fluorophores in proximity to a thin metal layer. The strong and well-known distance dependence of this quenching can be used to determine the precise distance of a fluorescent molecule from the surface, see Figure 4A. When using a thin gold film as the quencher, the accuracy of this axial localization can be as good as a few nanometers for typical single-molecule photon numbers.[18,22] With single graphene sheets as quenching material, even resolutions down to a few ångström are possible.[24] For MIET, total internal reflection (TIR) excitation is advantageous because it reduces background from the bulk and takes into account that MIET works anyway only over distances comparable to the penetration depth of the TIR excitation. This improves the signal-to-noise ratio (SNR) and therefore precision of the lifetime determination. For demonstrating the applicability of the LINCam25 for MIET measurements, we immobilized DNA-Atto 655 constructs on glass substrates that where coated with a thin gold film and topped with a SiO_2 spacer layer of well-defined thickness, see Figure 4A. The theoretical lifetime-height dependency for gold layer with 10 nm thickness is shown on Figure 4B. For typical DNA-Atto 655 lifetime images with different SiO_2 spacer thicknesses see Figure 4C. The obtained lifetime histograms are displayed in Figure 4D, see also the Supporting Information for the derived fluorophore height histograms. When assuming that the thickness of the BSA-biotin/neutravidin layer as ∼12 nm,[22] we find perfect agreement between the MIET-derived height values of the single fluorophores and the height values deduced from the sample architecture, see Table S3 and Figure S13 in the Supporting Information. We estimate the axial localization precision to be ∼10 nm from the standard deviation of the height histograms. For the biggest studied spacer layer thickness of 70 nm spacer (plus the extra height of the BSA-biotin/neutravidin layer), we reach the edge of the height range over which MIET still works (beyond that range, metal-induced quenching becomes too small to be useful for height determination). In that case, the localization accuracy is reduced and becomes ∼20 nm.

■ CONCLUSIONS

In this work, we performed single-molecule FLIM using the novel LINCam25 photon-counting camera. Although the camera's quantum yield of photon detection is only a few percent in the red spectral region, we could easily image single fluorescent molecules and determine their fluorescent lifetimes. To the best of our knowledge, this is currently the only wide-field lifetime imaging system (with a large field of view) with single-molecule sensitivity and a subnanosecond precision in lifetime determination. We used the system for measuring lifetimes of DNA-conjugated Cy5, Atto 655, and Atto 647N

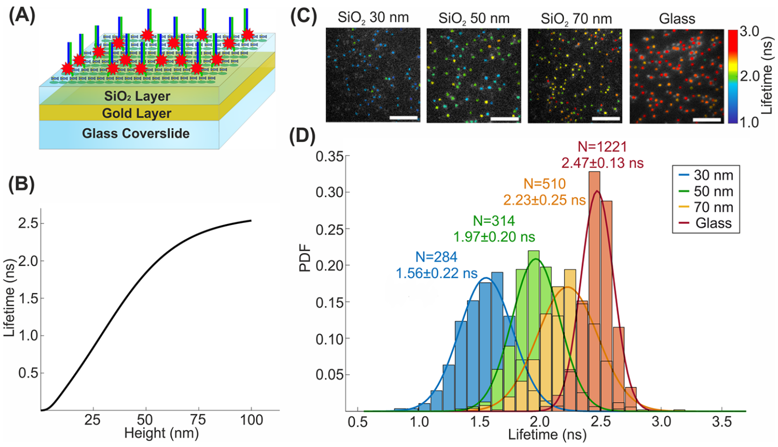

Figure 4. Application of single-molecule FLIM to MIET. (A) MIET experiment design. A 10 nm gold layer is deposited on top of a glass coverslip which is then covered with another spacer layer of SiO_2. (B) Theoretical lifetime-height dependency for a gold layer with 10 nm thickness. The height is given with respect to the gold layer surface. (C) Exemplary lifetime images of Atto 655 fluorophores on top of a glass/gold/SiO_2 substrate for different values of SiO_2 layer thickness (30, 50, and 70 nm). The glass coverslip was shown for the reference. The lifetime scale appears on the right-hand side of the image. (D) Lifetime histograms of Atto 655 fluorophores on different SiO_2 spacers (30, 50, and 70 nm) and the glass. The solid lines show fits with a single Gaussian distribution. The lifetime histograms include data from several regions of interest. Next to each peak are given the number of molecules included in the histogram, as well as the average lifetime and standard deviation.

fluorophores and were able to determine the lifetime values of single fluorophores with experimental errors of less than 0.3 ns, which is an exceptionally high precision taking into account the relatively low detection efficiency of the system in the red spectral region. Moreover, we could then successfully identify different types of fluorophores in a mixed fluorophores sample solely on the basis of their lifetime values. We found not only that it is possible to identify single molecules but also that their obtained lifetime values match within the experimental errors the values seen in pure samples of only one species. We showed implementation of the on/off-state-detection and dwell-time analysis for Atto 655 blinking behavior characterization and demonstrated that the LINCam25 is capable of capturing the blinking kinetics of single emitters. This makes the realization of SMLM with TCSPC-based lifetime determination feasible. In order to compare the performances of LINCam25 system with the conventional TCSPC-CLSM, we performed a measurement of mixed fluorophores sample with TCSPC-CLSM and found a remarkable agreement with the lifetime values obtained with LINCam25 system, see Figure S6 in the Supporting Information. We also found a good agreement between the lifetimes measured with LINCam25 in the diffusion-based samples and the lifetimes obtained using TCSPC-CLSM for the same samples, see Table S1 in the Supporting Information. As compared to TCSPC-CLSM, LINCam25 has an advantage of faster data acquisition. This advantage will be even more striking in the blue and green spectral regions, due to higher quantum efficiency of the camera than in the red. Finally, we demonstrated the application of single-molecule FLIM to MIET imaging for measuring the axial position of single fluorophores with ∼10 nm accuracy. This is a first step toward three-dimensional SMLM by combining conventional lateral single molecule localization with the axial localization provided by MIET.

■ ASSOCIATED CONTENT

Supporting Information

The Supporting Information is available free of charge at https://pubs.acs.org/doi/10.1021/acs.jpca.0c01513.

> Estimation of the detected number of photons emitted by each type of fluorophore; cumulative TCSPC curves of surface-immobilized fluorophores; fluorescence lifetimes of freely diffusing fluorophores; comparison of lifetime values measured with the LINCam25 and with TCSPC-CLSM; comparison between lifetime values obtained in LINCam25 measurements of pure and mixed fluorophores samples; influence of virtual pixel size on resolution of the lifetime histograms; on/off-state-detection algorithm and example of improved peak separation in lifetime histograms after applying a on/off-state-detection algorithm; description and scheme of experimental setup; analysis of peak broadening of lifetime histogram for Atto 655; detailed DNA sequences and its modifications; analysis of the blinking behavior of Atto 655; and MIET experiment details and experimental and calculated lifetime and height values for the DNA-conjugated Atto 655 fluorophores (PDF)

■ AUTHOR INFORMATION

Corresponding Authors

Roman Tsukanov − *III. Institute of Physics−Biophysics, Georg August University, 37077 Göttingen, Germany;* orcid.org/0000-0002-3967-1755; Phone: +49 551 39 26911; Email: rtsukan@gwdg.de

Jörg Enderlein − *III. Institute of Physics−Biophysics and Cluster of Excellence "Multiscale Bioimaging: from Molecular Machines to Networks of Excitable Cells" (MBExC), Georg August University, 37077 Göttingen, Germany;* orcid.org/0000-0001-5091-7157; Phone: +49 551 39 26908; Email: jenderl@gwdg.de

Authors

Nazar Oleksiievets − *III. Institute of Physics−Biophysics, Georg August University, 37077 Göttingen, Germany*

Jan Christoph Thiele − *III. Institute of Physics−Biophysics, Georg August University, 37077 Göttingen, Germany*

André Weber − *Special Laboratory for Electron and Laser Scanning Microscopy, Leibniz Institute for Neurobiology, 39118 Magdeburg, Germany*

Ingo Gregor − *III. Institute of Physics−Biophysics, Georg August University, 37077 Göttingen, Germany*

Oleksii Nevskyi − *III. Institute of Physics−Biophysics, Georg August University, 37077 Göttingen, Germany*

Sebastian Isbaner − *III. Institute of Physics−Biophysics, Georg August University, 37077 Göttingen, Germany*

Complete contact information is available at: https://pubs.acs.org/10.1021/acs.jpca.0c01513

Author Contributions

[§]These authors contributed equally to this work

Funding

N.O. is grateful to the Deutsche Forschungsgemeinschaft (DFG) for financial support via Project A10 of the SFB 803. J.C.T. is grateful to the DFG for financial support via Project A05 of the SFB 937 and to the International Max Planck Research School for Physics of Biological and Complex Systems (IMPRS PBCS) for financial support. A.W. was supported by German Federal Ministry of Education and Research (BMBF) via Project TCAM4Life (Grant Number 13N12675) and the DFG (Project TPZ of SFB 854). O.N. is grateful to the DFG for financial support via Project EN 297/16-1. S.I. is grateful to the Leibniz Gemeinschaft for financial support via Project K76/2017. J.E. is grateful to the DFG for financial support through Germany's Excellence Strategy EXC 2067/1-390729940.

Notes

The authors declare the following competing financial interest(s): Andre Weber is a part-time employee of Photonscore company. All other authors declare no completing financial interest.

■ ACKNOWLEDGMENTS

The authors are grateful to Photonscore GmbH and personally Dr. Yury Prokazov for the provided LINCam25 system and for the continuous support. We thank Dr. Evgeny Turbin for the help with electronics. We are grateful to Arindam Ghosh for the fruitful discussions.

■ REFERENCES

(1) Gadella, T. W., Jr; Jovin, T. M.; Clegg, R. M. Fluorescence lifetime imaging microscopy (FLIM): spatial resolution of microstructures on the nanosecond time scale. *Biophys. Chem.* **1993**, *48*, 221−239.

(2) Bastiaens, P. I.; Squire, A. Fluorescence lifetime imaging microscopy: spatial resolution of biochemical processes in the cell. *Trends Cell Biol.* **1999**, *9*, 48−52.

(3) van Munster, E. B.; Gadella, T. W. Fluorescence Lifetime Imaging Microscopy (FLIM). *Adv. Biochem. Eng./Biotechnol.* **2005**, *95*, 143−175.

(4) Niehörster, T.; Löschberger, A.; Gregor, I.; Krämer, B.; Rahn, H.-J.; Patting, M.; Koberling, F.; Enderlein, J.; Sauer, M. Multi-target spectrally resolved fluorescence lifetime imaging microscopy. *Nat. Methods* **2016**, *13*, 257−262.

(5) Periasamy, A.; Day, R. *Molecular imaging: FRET microscopy and spectroscopy*; Elsevier: 2011.

(6) Woźniak, A. K.; Schröder, G. F.; Grubmüller, H.; Seidel, C. A. M.; Oesterhelt, F. Single-molecule FRET measures bends and kinks in DNA. *Proc. Natl. Acad. Sci. U. S. A.* **2008**, *105*, 18337−18342.

(7) O'Connor, D. *Time-correlated single photon counting*; Academic Press: 2012.

(8) Dong, C. Y.; French, T.; So, P.; Buehler, C.; Berland, K. M.; Gratton, E. Fluorescence-lifetime imaging techniques for microscopy. *Methods Cell Biol.* **2003**, *72*, 431−464.

(9) Chen, H.; Holst, G.; Gratton, E. Modulated CMOS camera for fluorescence lifetime microscopy. *Microsc. Res. Tech.* **2015**, *78*, 1075−1081.

(10) Niclass, C.; Favi, C.; Kluter, T.; Gersbach, M.; Charbon, E. A 128 × 128 Single-photon image sensor with column-level 10-bit time-to-digital converter array. *IEEE J. Solid-State Circuits* **2008**, *43*, 2977−2989.

(11) Veerappan, C. C.; Richardson, J.; Walker, R.; Li, D.-U.; Fishburn, M. W.; Maruyama, Y.; Stoppa, D.; Borghetti, F.; Gersbach, M.; Henderson, R. K.; et al. A 160 × 128 single-photon image sensor with on-pixel 55ps 10b time-to-digital converter. *2011 IEEE International Solid- State Circuits Conference - (ISSCC)* **2011**, 312−314.

(12) Sparks, H.; Görlitz, F.; Kelly, D. J.; Warren, S. C.; Kellett, P. A.; Garcia, E.; Dymoke-Bradshaw, A. K. L.; Hares, J. D.; Neil, M. A. A.; Dunsby, C.; et al. Characterisation of new gated optical image intensifiers for fluorescence lifetime imaging. *Rev. Sci. Instrum.* **2017**, *88*, No. 013707.

(13) Bowman, A. J.; Klopfer, B. B.; Juffmann, T.; Kasevich, M. A. Electro-optic imaging enables efficient wide-field fluorescence lifetime microscopy. *Nat. Commun.* **2019**, *10*, 1−8.

(14) Michalet, X.; Siegmund, O. H. W.; Vallerga, J. V.; Jelinsky, P.; Millaud, J. E.; Weiss, S. Photon-counting H33D detector for biological fluorescence imaging. *Nucl. Instrum. Methods Phys. Res., Sect. A* **2006**, *567*, 133.

(15) Prokazov, Y.; Turbin, E.; Weber, A.; Hartig, R.; Zuschratter, W. Position sensitive detector for fluorescence lifetime imaging. *J. Instrum.* **2014**, *9*, C12015.

(16) Ulku, A. C.; Ardelean, A.; Antolovic, I. M.; Weiss, S.; Charbon, E.; Bruschini, C.; Michalet, X. Wide-field time-gated SPAD imager for phasor-based FLIM applications. *Methods Appl. Fluoresc.* **2020**, *8*, No. 024002.

(17) Chizhik, A. I.; Rother, J.; Gregor, I.; Janshoff, A.; Enderlein, J. Metal-induced energy transfer for live cell nanoscopy. *Nat. Photonics* **2014**, *8*, 124.

(18) Karedla, N.; Chizhik, A. I.; Gregor, I.; Chizhik, A. M.; Schulz, O.; Enderlein, J. Single-Molecule Metal-Induced Energy Transfer (smMIET): Resolving Nanometer Distances at the Single-Molecule Level. *ChemPhysChem* **2014**, *15*, 705−711.

(19) Baronsky, T.; Ruhlandt, D.; Brückner, B. R.; Schäfer, J.; Karedla, N.; Isbaner, S.; Hähnel, D.; Gregor, I.; Enderlein, J.; Janshoff, A.; et al. Cell−substrate dynamics of the epithelial-to-mesenchymal transition. *Nano Lett.* **2017**, *17*, 3320−3326.

(20) Chizhik, A. M.; Ruhlandt, D.; Pfaff, J.; Karedla, N.; Chizhik, A. I.; Gregor, I.; Kehlenbach, R. H.; Enderlein, J. Three-Dimensional Reconstruction of Nuclear Envelope Architecture Using Dual-Color Metal-Induced Energy Transfer Imaging. *ACS Nano* **2017**, *11*, 11839−11846.

(21) Karedla, N. *Single-Molecule Metal-Induced Energy Transfer: From Basics to Applications*; Springer: 2017.

(22) Isbaner, S.; Karedla, N.; Kaminska, I.; Ruhlandt, D.; Raab, M.; Bohlen, J.; Chizhik, A.; Gregor, I.; Tinnefeld, P.; Enderlein, J.; et al. Axial colocalization of single molecules with nanometer accuracy using metal-induced energy transfer. *Nano Lett.* **2018**, *18*, 2616−2622.

(23) Gregor, I.; Chizhik, A.; Karedla, N.; Enderlein, J. Metal-induced energy transfer. *Nanophotonics* **2019**, *8*, 1689−1699.

(24) Ghosh, A.; Sharma, A.; Chizhik, A. I.; Isbaner, S.; Ruhlandt, D.; Tsukanov, R.; Gregor, I.; Karedla, N.; Enderlein, J. Graphene-based

metal-induced energy transfer for sub-nanometre optical localization. *Nat. Photonics* **2019**, *13*, 860−865.

(25) Betzig, E.; Patterson, G. H.; Sougrat, R.; Lindwasser, O. W.; Olenych, S.; Bonifacino, J. S.; Davidson, M. W.; Lippincott-Schwartz, J.; Hess, H. F. Imaging intracellular fluorescent proteins at nanometer resolution. *Science* **2006**, *313*, 1642−1645.

(26) Rust, M. J.; Bates, M.; Zhuang, X. Sub-diffraction-limit imaging by stochastic optical reconstruction microscopy (STORM). *Nat. Methods* **2006**, *3*, 793.

(27) Hess, S. T.; Girirajan, T. P.; Mason, M. D. Ultra-high resolution imaging by fluorescence photoactivation localization microscopy. *Biophys. J.* **2006**, *91*, 4258−4272.

(28) Sauer, M.; Heilemann, M. Single-molecule localization microscopy in eukaryotes. *Chem. Rev.* **2017**, *117*, 7478−7509.

(29) Jungmann, R.; Steinhauer, C.; Scheible, M.; Kuzyk, A.; Tinnefeld, P.; Simmel, F. C. Single-molecule kinetics and super-resolution microscopy by fluorescence imaging of transient binding on DNA origami. *Nano Lett.* **2010**, *10*, 4756−4761.

(30) Schnitzbauer, J.; Strauss, M. T.; Schlichthaerle, T.; Schueder, F.; Jungmann, R. Super-resolution microscopy with DNA-PAINT. *Nat. Protoc.* **2017**, *12*, 1198−1228.

(31) Hartig, R.; Prokazov, Y.; Turbin, E.; Zuschratter, W. Wide-Field Fluorescence Lifetime Imaging with Multi-anode Detectors. *Methods Mol. Biol.* **2014**, *1076*, 457−480.

(32) Stein, S. C.; Thiart, J. TrackNTrace: A simple and extendable open-source framework for developing single-molecule localization and tracking algorithms. *Sci. Rep.* **2016**, *6*, 37947.

(33) Heilemann, M.; Herten, D. P.; Heintzmann, R.; Cremer, C.; Müller, C.; Tinnefeld, P.; Weston, K. D.; Wolfrum, J.; Sauer, M. High-resolution colocalization of single dye molecules by fluorescence lifetime imaging microscopy. *Anal. Chem.* **2002**, *74*, 3511−3517.

(34) van de Linde, S.; Krstić, I.; Prisner, T.; Doose, S.; Heilemann, M.; Sauer, M. Photoinduced formation of reversible dye radicals and their impact on super-resolution imaging. *Photochem. Photobiol. Sci.* **2011**, *10*, 499−506.

(35) Vogelsang, J.; Cordes, T.; Tinnefeld, P. Single-molecule photophysics of oxazines on DNA and its application in a FRET switch. *Photochem. Photobiol. Sci.* **2009**, *8*, 486−496.

■ NOTE ADDED AFTER ASAP PUBLICATION

This paper was published ASAP on April 17, 2020, with an incorrect Supporting Information document inadvertently due to production. The corrected version was posted on April 20, 2020.

Supporting Information: Wide-Field Fluorescence Lifetime Imaging of Single Molecules

Nazar Oleksiievets,[†,§] Jan Christoph Thiele,[†,§] André Weber,[‡] Ingo Gregor,[†]
Oleksii Nevskyi,[†] Sebastian Isbaner,[†] Roman Tsukanov,[*,†] and Jörg Enderlein[*,†,¶]

[†] *III. Institute of Physics – Biophysics, Georg August University, 37077 Göttingen, Germany.*

[‡] *Special Laboratory for Electron and Laser scanning Microscopy, Leibniz Institute for Neurobiology, 39118 Magdeburg, Germany.*

[¶] *Cluster of Excellence "Multiscale Bioimaging: from Molecular Machines to Networks of Excitable Cells" (MBExC), Georg August University, Göttingen, Germany.*

[§] *These authors contributed equally to this work*

E-mail: rtsukan@gwdg.de; jenderl@gwdg.de

Estimation of the detected number of photons emitted by each type of fluorophore

In order to estimate detected number of photons emitted by each type of fluorophore until photobleaching, we count the photons coming from each detected single molecule and histogram these values. Then, the mean value is calculated for each type of the fluorophores (Cy5, Atto 655, and Atto 647N), see Figure S1. The obtained average values were as following: Cy5 – 196 photons, Atto 655 – 1759 photons, and for Atto 647N – 3242 photons.

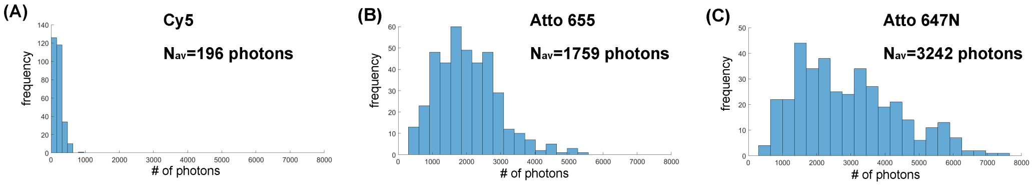

Figure S1: Distributions of detected photon numbers per fluorophore till photobleaching: (A) Cy5, (B) Atto 655 and (C) Atto 647N.

Cumulative TCSPC curves of surface-immobilised fluorophores

Analysis of fluorescence lifetime decays was performed using a custom-written MATLAB routine. First, photon positions and photon arrival times were read from the raw data file of the LINCam using MATLAB functions provided by the Photonscore Software Kit for FLIM analysis. Next, the detector area is divided into 512x512 virtual pixels. In order to optimise photon detection yield of the LINCam25 system, we optically restricted the region of interest using a slit aperture (see "Experimental setup" below). A single exponential function was used to tail-fit the TCSPC curves as described in the main text, with the cutoff window from 12.6 ns till 30.0 ns. The following average lifetimes were obtained for each of the dyes: Cy5 - 1.49 ± 0.01 ns; Atto 655 - 2.46 ± 0.01 ns; Atto 647N - 3.77 ± 0.01 ns. The errors are the standard deviation of three consecutive measurements for each case.

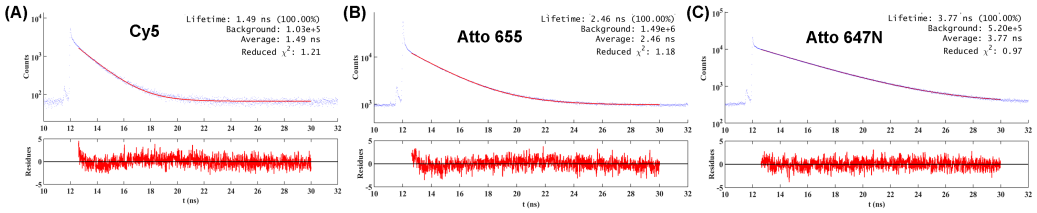

Figure S2: Cumulative TCSPC curves for the three types of the fluorophores immobilised on a surface, together with the corresponding single-exponential fits: (A) Cy5, (B) Atto 655, (C) Atto 647N. The fit output is given in the plot.

Fluorescence lifetimes of freely diffusing fluorophores

We investigated the lifetimes of freely diffusing DNA-fluorophore constructs. Ensemble measurements were performed at high concentration (10 nM) of the molecules. For the diffusion experiment, TCSPC fitting procedure was performed as described in the main text. However, different TCSPC cutoff window were used for LINCam25 and TCSPC-CLSM, starting from 17.8 ns till 35.2 ns for LINCam25 system and from 3.6 ns till 21.0 ns for TCSPC-CLSM. We found that for Cy5 and Atto 655, the single exponential function does not describe well the experimental TCSPC curves, and therefore we fitted these curves by a double exponential function, as shown in Figure S3. In both cases, an additional faster lifetime component can be explained by the presence of fluorophores that were not bound to DNA. This is due to the fact that the faster lifetime values fully agree with the lifetimes of the non-conjugated Cy5 and Atto 655 measured by us (data not shown). We attribute the longer lifetime component to the DNA-dye constructs. It shall be noticed that, while immobilising the DNA-dye construct to the surface, free dye is flushed from the sample and therefore does not affect the measurements of surface-immobilised molecules. As expected, we find that the lifetimes of freely diffusing fluorophores are 5-10% longer than the values of the same molecules immobilised on glass coverslips and this is due to surface-fluorophore interaction.[S1]

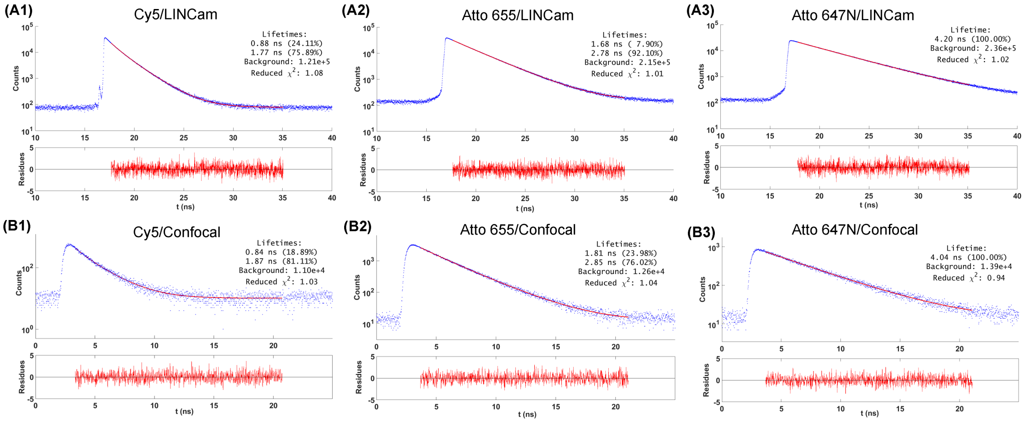

Figure S3: Lifetime measurements of freely diffusing fluorophores using either LINCam (A) or TCSPC-CLSM (B). The TCSPC curves and the correspondent single- or double-exponential fits are shown for: (A1,B1) Cy5, (A2,B2) Atto 655, (A3,B3) Atto 647N. For convenience, all lifetime values are summarised in Table S1

Comparison of lifetime values measured with the LINCam25 and with TCSPC-CLSM

In order to verify the lifetime values obtained by the LINCam25, we performed independent measurements for all three fluorophores in solution using our TCSPC-CLSM setup. For the TCSPC-CLSM data, lifetime values were determined by tail-fitting the TCSPC curves with exponential decay functions, similar to what we have done for the LINCam data, see Figure S3. We found a remarkable agreement between the lifetimes for both single- and double-exponential decay fits. The results are listed in Table S1. The errors are the standard deviation of three consecutive measurements for each case.

In addition to a freely-diffusing molecules, we performed the lifetime confocal scan of surface-immobilised mixed fluorophores using the TCSPC-CLSM setup, see Figure S4.

Imaging parameters for the TCSPC-CLSM measurement were as following: virtual pixel size was 100 nm, frame size was 400 × 400 pixels with total area of interest of 40 × 40 microns. We used bidirectional scan to make the measurement faster and also collect more photons, as compared to a single-directional scan. Dwell time was 100 μs.

Table S1: Lifetime values of freely diffusing molecules measured by LINCam25 and with the TCSPC-CLSM setup.

Fluorophore	Setup	$\tau_{free-dye}$ (ns)	$\tau_{DNA-dye}$ (ns)
Cy5	LINCam25	0.88 ± 0.01	1.77 ± 0.01
Cy5	confocal	0.84 ± 0.04	1.87 ± 0.02
Atto 655	LINCam25	1.68 ± 0.09	2.78 ± 0.02
Atto 655	confocal	1.81 ± 0.10	2.85 ± 0.09
Atto 647N	LINCam25	-	4.20 ± 0.01
Atto 647N	confocal	-	4.04 ± 0.01

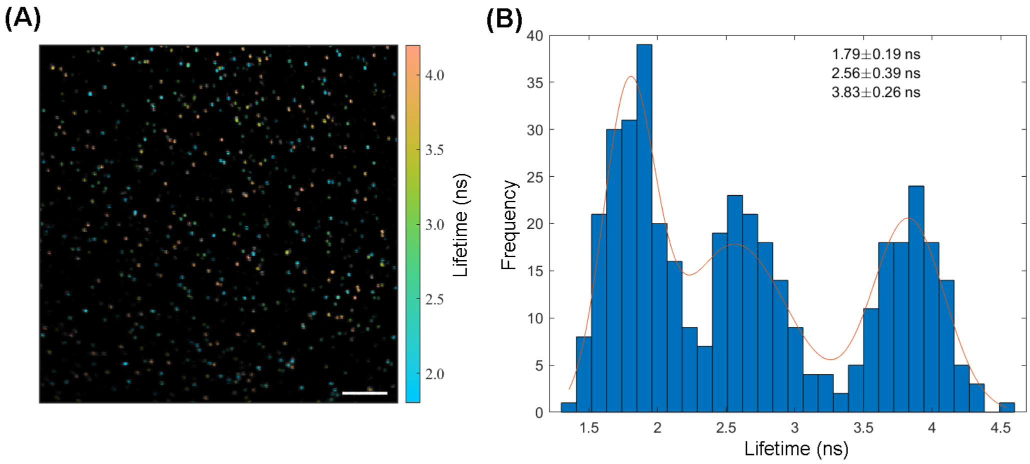

Figure S4: FLIM image using the TCSPC-CLSM setup of a mixture of Cy5, Atto 655 and Atto 647N fluorophores immobilised to the surface. (A) Exemplary lifetime image. Pseudo colours depict the lifetime values. The scale of lifetimes appears on the right-hand side of the image. The scale bar is 5 microns. (B) Lifetime histogram of the mixed sample and the corresponding three peak Gaussian fit. The solid line represents a fit. The fit output is given in the plot.

In the next step, we compared the results of the mixed fluorophores sample measured by LINCam25 and TCSPC-CLSM setup, see Figure S5.

Same as for the freely diffusion case, for the surface immobilised case we found an excellent agreement between the lifetime values for the both experimental approaches. However, it is evident that the width of the peaks for the TCSPC-CLSM measurements is broader than for the LINCam25 peaks. When we compared the number of photons acquired during the same time interval for both techniques, we found that the TCSPC-CLSM setup registered five-fold

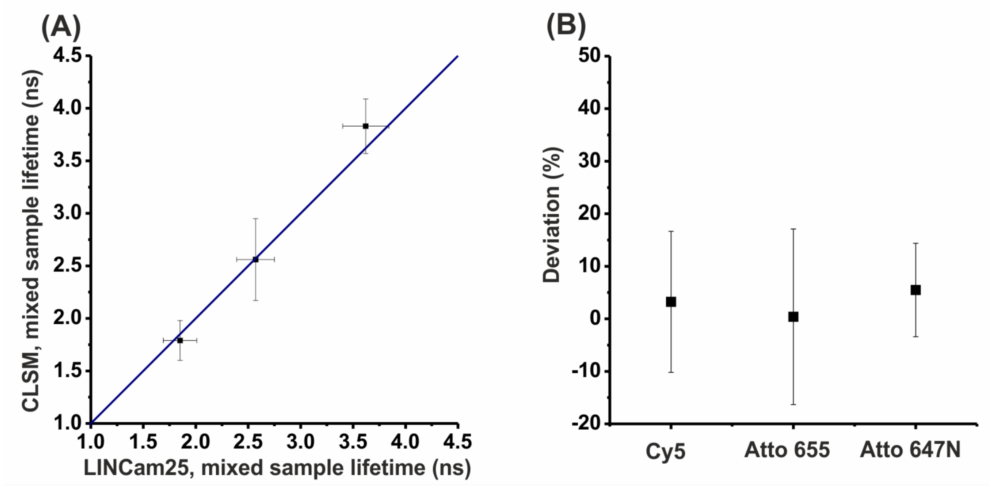

Figure S5: Comparison between lifetime values measured by the LINCam25 system and TCSPC-CLSM setup. (A) Mixed fluorophores sample. The blue line shows the equal lifetimes. (B) The relative deviation between the two experimental techniques.

less photons that LINCam25, despite the fact its quantum efficiency is only ∼5%. It could be that the data accumulation runs slower for the TCSPC-CLSM because the excitation laser time is shared between the molecules during the data acquisition process.

Comparison between lifetime values obtained in LINCam25 measurements of pure and mixed fluorophores samples

We compared the lifetime values obtained for pure and mixed fluorophores samples for the surface-immobilised case, see Figure S6. For both measurements, the central peaks corresponding to the surface-immobilised Atto 655 molecules show a very good agreement. For the mixed sample, the peaks positioned on the left-hand side of the histogram (corresponds to Cy5) and right-hand side of the histogram (corresponds to Atto 647N) are shifted towards the centre, as also shown in Figure 3 in the main text. These shifts can be explained by the relatively high density of fluorophores that was used in the mixed sample. This was done on purpose to mimic a dense labelling scenario, as often found in real biological samples.

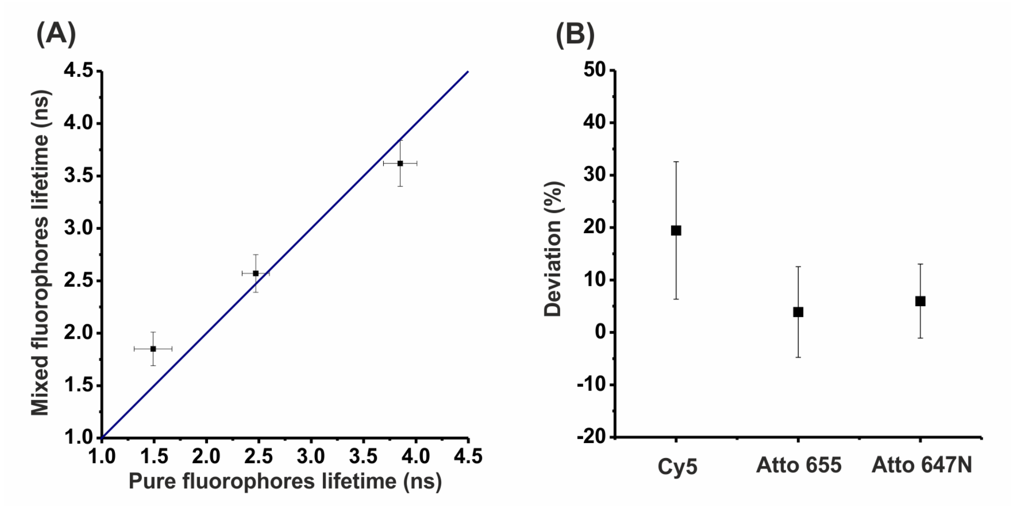

Figure S6: Comparison between the average lifetimes obtained by LINCam25 system. (A) Pure and mixed fluorophores sample of surface-immobilised case. The blue line shows the equal lifetimes. (B) The relative deviation between pure and mixed fluorophores sample lifetimes.

Influence of virtual pixel size on resolution of the lifetime histograms

When fluorophores with different lifetimes are densely distributed on a surface, cross-talk of emission from neighbouring molecules is unavoidable and can affect the determined lifetime values of individual molecules. We confirmed this in the following way: lifetime images taken on mixed samples were divided into virtual pixels of two different sizes, starting from 96 nm (same as used in this assay) to 192 nm pixel size. For the larger pixel size, the side peaks in the lifetime histograms shifted towards the centre, see Figure S7 C. The pixel size had no effect on the lifetime histograms of the pure samples of fluorophores with low surface concentration, see Figure S7 A, B. Division into smaller virtual pixels could be one option for reducing cross-talk effects, but it would also lead to lower photon numbers per pixel and thus increased shot noise. Therefore, we suggested a on/off-state-detection analysis (see below) for improving assignment of photons to individual fluorophores.

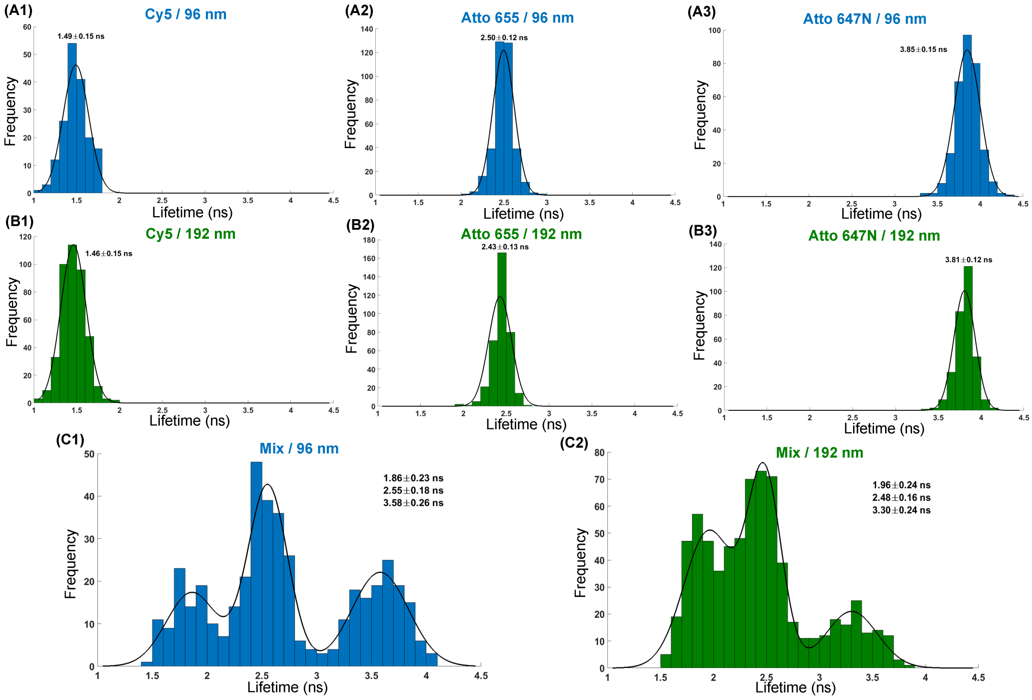

Figure S7: Influence of virtual pixel size on lifetime histograms. (A1-3) and(C1): Lifetime histograms for pure and mixed fluorophore samples when using a pixel size of 96 nm. (B1-3) and (C2): The same for a pixel size of 192 nm.

On/off-state-detection algorithm

We used an on/off-state-detection algorithm for identifying on-states within intensity time traces of individual molecules.[S2] Briefly, the intensity time trace recorded from one molecule is smoothed by applying a moving Lee-filter, and a step (switching from off- to on-state or vice versa) is identified if the smoothed signal exceeds a pre-set threshold. This threshold is determined as twice the background level, and it is scaled for each molecule by the maximum intensity in its time trace divided by the average of the maximum intensities over all molecules. The scaling of the threshold is required to compensate for inhomogeneous illumination. The background level is estimated as the median of all intensities in all time traces below the average intensity level. In order to verify the efficiency of this on/off-state-detection algorithm, we compared the lifetime histograms obtained by taking into account all photons with those obtained after applying the algorithm, see Figure S8 A. As expected, the on/off-state-detection algorithm efficiently reduces contributions from neighbouring molecules by taking into account only photons belonging to the on-state of the analysed fluorophore. This results in an improved separation between peaks in the lifetime histograms, see Figure S8 B. In addition, the algorithm was employed for the detection of on/off-states of blinking Atto 655 fluorophores, see chapter "Characterisation of Atto 655 blinking behaviour" below. Therefore, the on/off-state-detection algorithm can be an efficient tool for the analysis of samples with high label density and/or fluorophores with poor photo-stability or significant blinking.

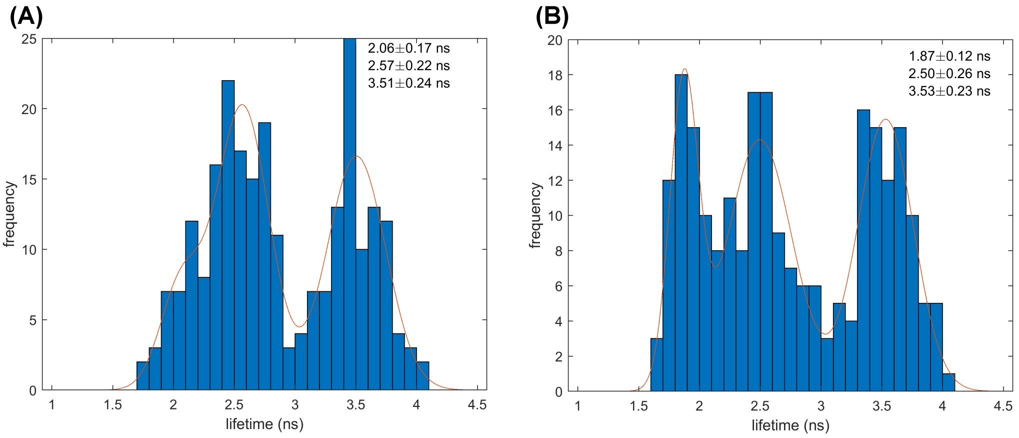

Figure S8: Improved peak separation in lifetime histograms after applying a on/off-state-detection algorithm. (A) Lifetime histogram obtained from a single movie of mixed fluorophores sample, when all photons are included. The solid line represents a fit with three Gaussians. Fit values are given in the plot. (B) Same as before, but after applying the on/off-state-detection algorithm.

Experimental setup

Measurements were performed using a custom-built setup. A pulsed super-continuum white-light laser (Fianium WhiteLase SC450, NKT Photonics) with pulse repetition of 20 MHz was used for excitation. A custom photodiode (PD) was used to optically trigger the LINCam. A clean-up filter (CUF) (ZET 640/10, Chroma) was used for narrowing the spectral width of the excitation light. Neutral density filters (NE10A-A,NE20A-A, Thorlabs) in combination with a variable neutral density filter (ND) (NDC-50C-4-A, Thorlabs) were used to adjust the laser excitation power. The laser beam was coupled into a single-mode optical fiber (SMF) (P1-460B-FC-2, Thorlabs) with a typical coupling efficiency of 40-50%. After the fiber, the beam was expanded by a factor of 3.6 using two telescopic lenses (TL1 and TL2). The collimated laser beam was focused into the back focal plane of the objective (UAPON 100x oil, 1.49 NA, Olympus) using lens L1 (AC508-180-AB, Thorlabs). In order to switch between different illumination schemes (Epi-, HILO-, or TIR), a translation stage TS (LNR50M, Thorlabs) was used to mechanically shift the beam perpendicular to the optical axis. A high-performance two-axis linear stage (M-406, Newport) was used for smooth lateral sample positioning. An independent one-dimensional translation stage (LNR25/M, Thorlabs) was equipped with differential micrometer screw (DRV3, Thorlabs) to move the objective along the optical axis for focusing. Collected fluorescence was spectrally separated from the excitation pathway using a multi-band dichroic mirror (DM) (Di03 R405/488/532/635, Semrock), which sent the fluorescence light towards the tube lens L2 (AC254-200-A-ML, Thorlabs). An adjustable slit aperture (SP60, OWIS) was positioned in the image plane and was used for selecting a region of interest within the field of view. Lenses L3 (AC254-100-A, Thorlabs) and L4 (AC508-150-A-ML, Thorlabs) re-imaged the fluorescence light form the slit onto an emCCD camera (iXon Ultra 897, Andor). Alternatively, lens L5 (AC508-250-A-MC, Thorlabs) re-imaged the light onto the lifetime camera (LINCam, Photonscore). For switching between the two cameras, a dielectric mirror (BB1-E02, Thorlabs) was positioned on a magnetic base plate MB (KB50/M, Thorlabs) with removable top. A band-pass filter BP (BrightLine HC 692/40, Semrock) was used to reject scattered excitation light. Magnification for imaging with the emCCD was 166.6X, resulting in an effective pixel size in sample space of 103.5 nm. Magnification for imaging with LINCam was 222X, so that for a partitioning of the field of view into 512 X 512 pixels, the effective pixel size in sample space was 191.6 nm.

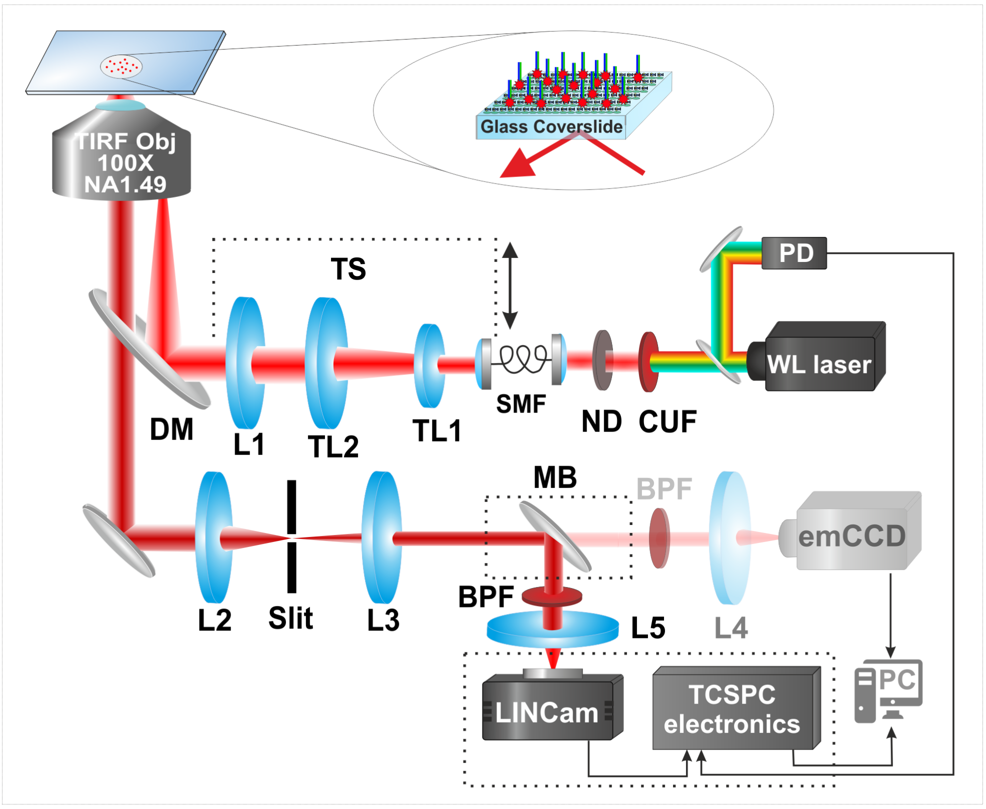

Figure S9: Detailed schematic of the custom-built optical setup used for wide-field lifetime imaging with the LINCam25.

Theoretical estimate of the peak broadening of lifetime histograms

To judge how close the experimentally observed width of the lifetime histograms comes close to the theoretical shot-noise limit, we calculated theoretical shot-noise limited distribution in the following way: we first determined a mean lifetime $\langle\tau\rangle$ as the average of lifetime values from all identified molecules. Then, for each molecule we generated a Gaussian distribution of unit area with peak position at $\langle\tau\rangle$ and variance equal to $\langle\tau\rangle^2/N$, where N is the number of detected photons from the considered molecule. Finally, we added all these Gaussians into one final theoretical lifetime distribution. For the Atto 655 sample, the standard deviation of this theoretical distribution was 0.06 ns, see Figure S10 B. Fitting the experimentally determined histogram with a single Gaussian yields a standard deviation of 0.13 ns, see Figure S10 A. We attribute this extra broadening of the experimental histogram to lifetime variations due to local molecule-environment interactions.

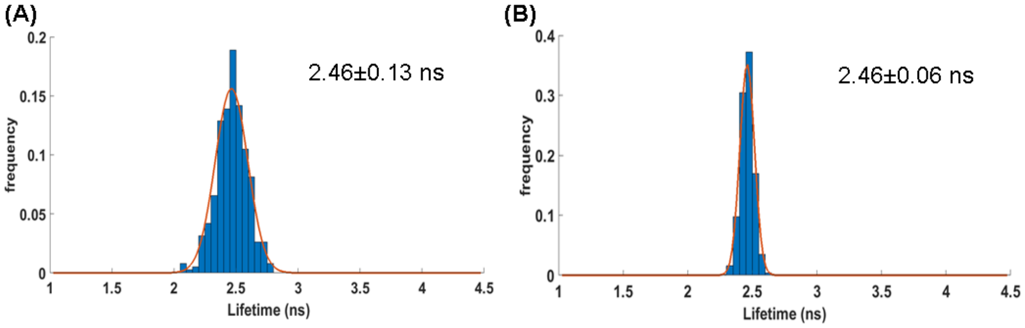

Figure S10: Analysis of peak broadening of lifetime histogram for Atto 655. (A) Experimental determined lifetime histogram with single Gaussian fit. (B) Shot-noise limited theoretical lifetime histogram generated from experimental data.

DNA sequences

Table S2: Detailed DNA sequences and its modifications

name	sequence $5' \rightarrow 3'$	$5'$ modification	$3'$ modification
strand 1	GCAGCCACAACGTCTATCATCGATT	-	fluorophore
strand 2	AATCGATGATAGACGTTGTGGCTGC	biotin	-

Characterisation of Atto 655 blinking behaviour

Although the detection efficiency of the LINCam25 is rather low, we were able to capture blinking events of single Atto 655 fluorophores. Conditions that favour blinking were created by adding GLOX buffer to the sample solution, as described in the “Methods” section in the main text. The blinking behaviour analysis included On/off-state-detection algorithm to identify the states for each single fluorophore, as shown in the exemplary trajectories in Figure S11 A1-3. Then, dwell time analysis was employed to determine the on- and off-times. Both histograms for the on- and off-times were fitted with single exponential functions, see Figure S11 B. From these fits, the following characteristic on- and off-time values were obtained: τ_{on}=8.2 s ,τ_{off}=10.5 s. Compared to literature values,[S3] we find rather slow on- and off-times for Atto 655, which may be explained by presence of GLOX buffer[S4] and the low laser power used in our experiment. Atto 655 fluorophores without addition of GLOX exhibit blinking on much faster time-scale. To demonstrate it, we imaged same surface-immobilised Atto 655 fluorophores in imaging buffer B4 with 500 mM NaCl. In this case we observed fast blinking events, which could not be captured by LINCam25 system, see Figure S12.

Metal-Induced Energy Transfer (MIET)

For the MIET experiments, we used substrates consisting of a glass coverslip covered by a thin 10 nm gold film which was coated with with a SiO_2 spacer laser of variable thickness (30, 50 and 70 nm). DNA-bound Atto 655 fluorophores were attached to the surface, using the same procedure as for pure glass coverslips. Measured average lifetime values were compared to theoretical values calculated using MIET theory,[S5] where we assumed that the actual distance of fluorescent molecules from the metal was given by the thickness of the SiO_2 spacer plus the width of the BSA-biotin/neutravidin layer (12 nm).[S1] A comparison between experimental and theoretical values is given in Table S3. As can be seen, there is excellent agreement between measured and theoretically calculated values, showing that MIET works well with the LINCam25 FLIM system.

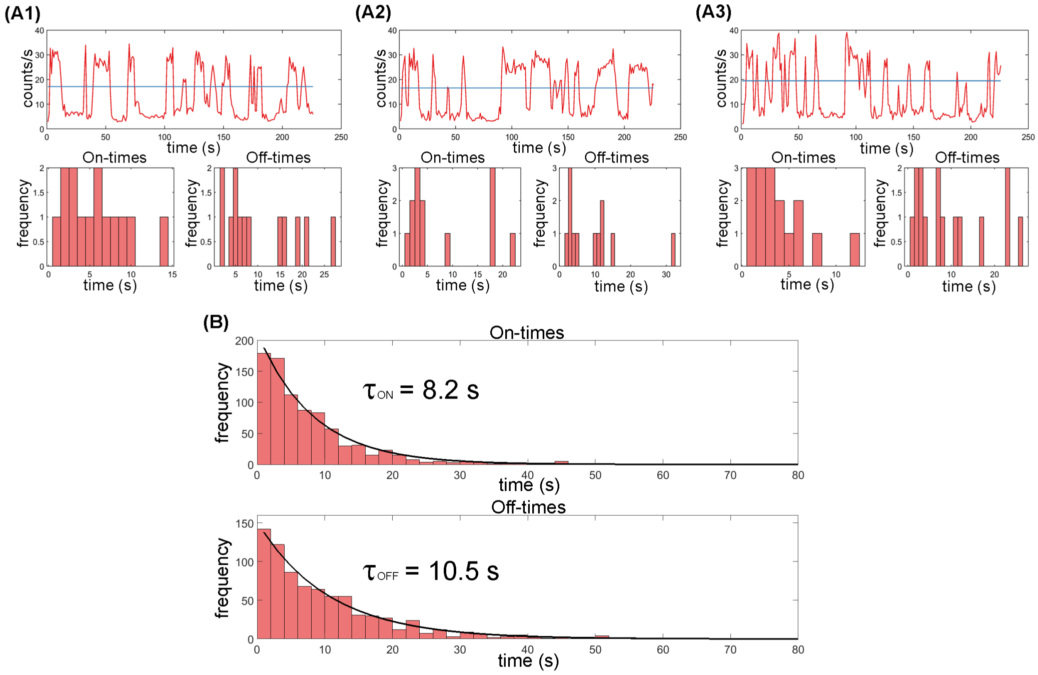

Figure S11: Analysis of the blinking behaviour of Atto 655. (A1-3) Exemplary intensity time traces for single molecules and corresponding dwell time histograms. Solid blue lines represent the thresholds applied to the time traces. (B) Cumulative on- and off-dwell time histograms for 65 time traces with corresponding single exponential fits (solid line). The values for the average on- and off-times are given in the plot.

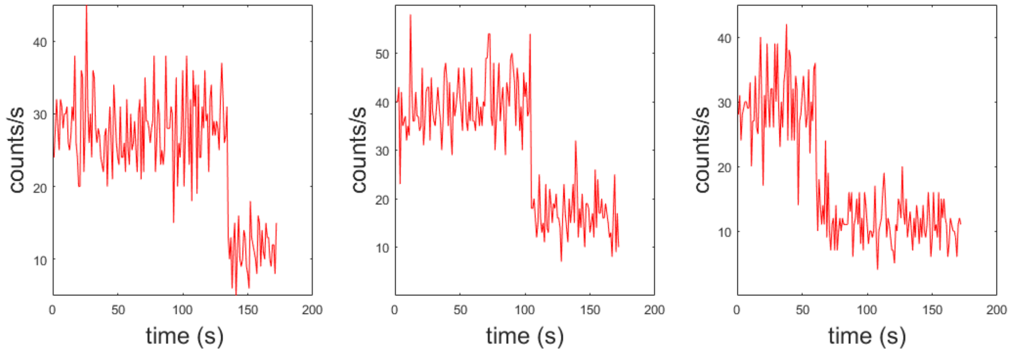

Figure S12: Atto 655 in a fast-blinking conditions, without the presence of GLOX in the buffer solution. Exemplary intensity time traces for Atto 655 single molecules are shown.

Table S3: Experimental and calculated lifetime and height values for the MIET experiment.

h_{design} (nm)	τ_{theory} (ns)	$\tau_{experiment}$ (ns)	$h_{experiment}$ (nm)
42	1.40	1.56 ± 0.22	45.15 ± 6.99
62	2.02	1.97 ± 0.20	59.88 ± 9.44
82	2.33	2.23 ± 0.25	76.2 ± 20.38
Glass	-	2.47 ± 0.13	-

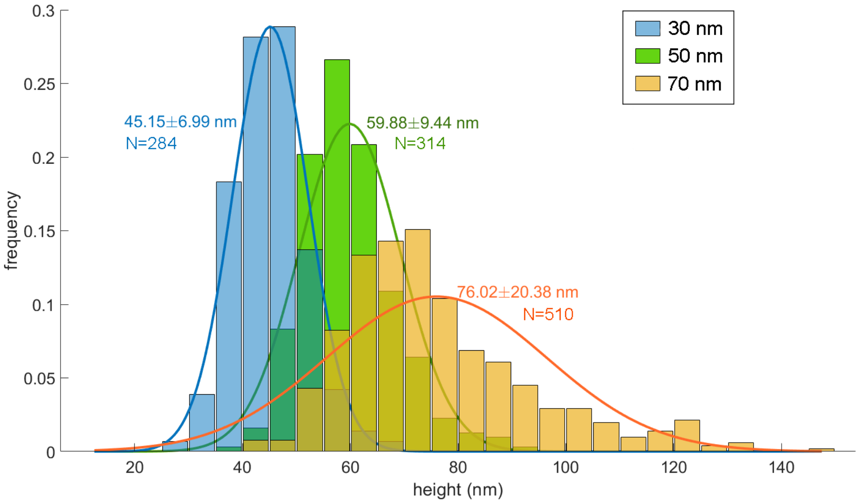

Figure S13: Metal-Induced Energy Transfer: Histograms of axial positions (height values) of single molecules as determined from their measured lifetime values. The thickness of the BSA-biotin/neutravidin layer was assumed to be 12 nm, which adds to the SiO_2 spacer thickness. Single Gaussian distributions were fitted to each peak, and the average values, the standard deviations, and number of detected molecules are written next to each peak.

References

(S1) Isbaner, S.; Karedla, N.; Kaminska, I.; Ruhlandt, D.; Raab, M.; Bohlen, J.; Chizhik, A.; Gregor, I.; Tinnefeld, P.; Enderlein, J., et al. Axial colocalization of single molecules with nanometer accuracy using metal-induced energy transfer. *Nano letters* **2018**, *18*, 2616–2622.

(S2) Enderlein, J.; Robbins, D. L.; Ambrose, W. P.; Keller, R. A. Molecular shot noise, burst size distribution, and single-molecule detection in fluid flow: effects of multiple occupancy. *The Journal of Physical Chemistry A* **1998**, *102*, 6089–6094.

(S3) Vogelsang, J.; Cordes, T.; Tinnefeld, P. Single-molecule photophysics of oxazines on DNA and its application in a FRET switch. *Photochem. Photobiol. Sci.* **2009**, *8*, 486–496.

(S4) van de Linde, S.; Krstić, I.; Prisner, T.; Doose, S.; Heilemann, M.; Sauer, M. Photoinduced formation of reversible dye radicals and their impact on super-resolution imaging. *Photochem. Photobiol. Sci.* **2011**, *10*, 499–506.

(S5) Gregor, I.; Chizhik, A.; Karedla, N.; Enderlein, J. Metal-induced energy transfer. *Nanophotonics* **2019**, *8*, 1689–1699.

4

FLUORESCENCE LIFETIME-BASED DNA-PAINT FOR MULTIPLEXED SUPER-RESOLUTION IMAGING OF CELLS

4.1 ABSTRACT

DNA-PAINT is a powerful super-resolution technique, that reaches spatial resolution of less than 10 nanometers and can be implemented in almost all conventional fluorescence microscopes. The multiplexing potential of DNA-PAINT is particularly attractive for bio-imaging applications. However, when it comes to the multiplexed imaging of cells, most of currently existing workflows suffer from drawbacks such as long acquisition times for Exchange-PAINT, or uncertainty in target identification when using a kinetic barcoding approach. Here, we introduce Fluorescence Lifetime PAINT (FL-PAINT), a new technique for multiplexed DNA-PAINT imaging, by combining DNA-PAINT with fluorescence lifetime imaging microscopy. FL-PAINT is capable of imaging multiple targets simultaneously. From raw lifetime images, single-target images are generated based on the lifetime information of the fluorophores used. We report about a combination of fluorophores that is particularly suitable for multiplexed FL-PAINT imaging within the green spectral region. We validate FL-PAINT against established Exchange-PAINT and exploit its multiplexing capabilities for 2D and 3D imaging of up to three targets simultaneously in COS-7 and HeLa cells. We realize FL-PAINT imaging using two different experimental techniques: wide-field Fluorescence Lifetime Imaging Microscopy (FLIM), and time-resolved Confocal Laser Scanning Microscopy (CLSM). Finally, we employ a Bayesian pattern-matching algorithm for optimal target identification. We anticipate that FL-PAINT will become a versatile and robust tool for multiplexed super-resolution imaging of biological samples.

4.2 INTRODUCTION

Fluorescence lifetime microscopy (FLIM) has become an important tool for bio-imaging, as it adds the fluorescence lifetime dimension to conventional intensity-based imaging. A recently introduced new generation of commercially available lifetime cameras [78] features single-molecule sensitivity [79], making the combination of FLIM and Single-Molecule Localisation Microscopy (SMLM) feasible. Moreover, a recently reported SMLM using Confocal Laser-Scanning Microscopy (CLSM) considerably broadens the availability of Fluorescence Lifetime SMLM (FL-SMLM) [80].

Bio-imaging particularly benefits from multiplexed super-resolution imaging, as it allows to investigate the co-localization of different intracellular targets with high resolution. Such information sheds light on the mutual organisations, interaction, and function of different organelles [81]. There exist numerous experimental techniques for multiplexed imaging [82][53], among them methods that are based on sequential label exchange using microfluidic platforms [54][55].

DNA-PAINT is a rapidly developing super-resolution technique, capable of generating images with nearly molecular resolution. The fact that DNA-PAINT can be readily realized with almost all conventional fluorescence microscopes makes it particularly attractive. DNA-PAINT exploits several of the unique properties of DNA: stability, orthogonality, and designability. Such combination makes DNA-PAINT a favored choice for multiplexed super-resolution imaging [42].

In order to use the full power of DNA-PAINT for cellular imaging, considerable efforts were invested into enhancing its resolution by bringing the reporter dye as close as possible to the target of interest. In this direction, one of the most exciting labelling ligands are aptamers [83][84] and affimers [85]. However, their widespread availability is still limited. Also, high-affinity small binders to commonly available protein were reported [86]. Another approach uses single-domain antibodies (nanobodies), some of them being commercially available and possessing a high affinity against commonly used fluorescent proteins (BFP, GFP and RFP) [87]. These nanobodies are also used in this work.

The general idea behind multiplexed DNA-PAINT imaging is to reversibly bind short pieces of single-stranded DNA (imager strands) with different sequences to complementary docking strands, which are in turn coupled to specific targets of interest. Among the existing multiplexed DNA-PAINT strategies, two techniques stand out. The first one, called Exchange-PAINT [6][87], performs sequential imaging of targets by introducing different imager strands directed against different targets one-by-one. Exchange-PAINT is capable of imaging, in principle, an unlimited number of targets. However, the total acquisition time increases linearly with the number of imaged targets and can become exceedingly long for multi-target imaging. The second technique is based on engineering the binding/unbinding kinetics (alternatively called kinetic barcoding) [57]. It relies on the tunability of the binding/unbinding kinetics of an imager strand to/from its complementary docking strand. The binding kinetics can be further optimised by using particular imager sequences, specifically designed to prevent the formation of secondary structures [56] or to introduce repetitive complementary sequences in the docking strands [43]. Both approaches significantly shorter the acquisition times and decrease imager concentration, while the latter improves the signal-to-noise ratio. Using protein binding agents can further facilitate binding speed of the imager strand to the docking strand [44]. However, implementing kinetic barcoding for multiplexed DNA-PAINT imaging of cells suffers from high variability in the binding kinetics due to the dense and sticky environment inside the cell, limiting the number of targets that can be imaged. As an alternative, single-molecule FLIM (smFLIM) enables detection and identification of different species of molecules emitting within the same spectral emission window, while completely avoiding chromatic aberration. In this study, we demonstrate fluorescence lifetime multiplexing for DNA-PAINT (FL-PAINT) and we validate this technique against the Exchange-PAINT. We apply FL-PAINT for multi-target cellular 2D and 3D imaging of common cell lines. We report on a combination of three of fluorophores that is particularly suitable for lifetime-based multiplexing in the green spectral region. We present two different realizations of FL-PAINT: one using wide-field FLIM, and the other using Confocal Laser-Scanning Microscopy (CLSM).

4.3 METHODS

4.3.1 *Preparation of COS-7 cells*

COS-7 cells were cultured in DMEM medium supplemented with 4 mM l-glutamine, 10% (v/v) Fetal Calf Serum (Thermo Fisher Scientific), 60 U/ml of penicillin and 0.06 mg/ml streptomycin (Sigma-Aldrich) in 5% CO2 at 37°C. Prior to plating the cells, ca. 20.000 cells/well were triple transfected for mitochondria, histones, and endoplasmic reticulum (ER) with 70 ng TOM70-GFP, 131 ng H2B-mTagBFP and 131 ng GalNac-mCherry, respectively. During transfection, 2% lipofectamine 2000 was used according to manufacturer's instructions. After transfection, cells were plated in 8-well chambers (155411PK, Thermo Fisher Scientific), incubated for ca. 16 hours, and subsequently fixed using 4% paraformaldehyde (PFA) for 30 minutes at room temperature. The remaining aldehydes were quenched with 0.1 M glycine in PBS for 15 minutes.

4.3.2 *Preparation of HeLa cells*

HeLa cells were cultured in low glucose Dulbecco's Modified Eagle Medium (DMEM) medium (Gibco) supplemented with 1% Pen/Strep (100 units/ml Penicillin and 100 μg/ml Streptomycin), 1% (w/v) glutamine and 10% (v/v) FCS in 5% CO2 at 37°C. 16000 cells were seeded on 8-well chambered cover glass (Cellvis) and transfected with GFP-

PTS1 (PST990) and mito-BFP (gift from Gia Voeltz, Addgene plasmid #49151) using Effectene (Qiagen) transfection reagent according to the manufacturer's instructions. 24 hours after transfection, cells were washed with phosphate buffered saline (PBS), fixed with 4% PFA in PBS for 30 min and permeabilized for 10 min using 1% Triton X-100 in PBS. After blocking for 30 min with 10% BSA in PBS (blocking buffer) at 37°C, antigens were labelled with rabbit anti-PEX14 (Proteintech, 10594-1-AP) and/or mouse anti-α-tubulin (Sigma, T9026) primary antibodies for 1 hour at room temperature.

4.3.3 *Immunostaining*

Cells were permeabilized and blocked using 2% bovine serum albumin (BSA) and 0.1% Triton X-100 in PBS for 30 minutes at room temperature. Buffer solution containing nanobodies coupled to the docking strand (50 nM) was used to stain the cells. For this purpose, we incubated cells for 1 h at room temperature, with slow orbital shaking. Finally, the cells were rinsed with PBS and then post-fixed with 4% PFA for 15 minutes at room temperature. Cells were stored in PBS buffer at 4°C. The unconjugated nanobodies FluoTag-Q anti-GFP, FluoTag-Q anti-RFP, and the FluoTag-Q anti-TagBFP (NanoTag Biotechnologies GmbH, Göttingen, Germany, Cat. No: N0301, N0401, and N0501, respectively) carry one ectopic cysteine at the C-terminus allowing for chemical coupling via a thiol reactive compound. The docking strand sequences used for the assay were taken from Agasti et al [88]. The DNA docking strands (Biomers GmbH, Ulm, Germany) were functionalized with an azide group at 5'-end. Coupling of the docking strands to the nanobodies was performed following the procedure described previously [85]. FluoTag-Q anti-GFP was coupled to P1* sequence (5'-CTAGATGTAT-Atto488-3'), FluoTag-Q anti-RFP was coupled to P2* (5'-TATGTAGATC-3'), and FluoTag-Q anti-TagBFP was coupled to P3* (5'-GTAATGAAGA-3').

4.3.4 *Screening of fluorophores in the green spectral range suitable for FL-PAINT*

We distinguish different cellular targets based on the different fluorescence lifetimes of the fluorophores conjugated to the imager strands. This requires careful fluorophore selection. The green spectral range was chosen due the improved quantum yield of the lifetime camera in this spectral range. Besides the lifetime of the fluorophores, additional selection criteria were brightness, reduced number of unspecific bindings of imager inside cells, and width of the lifetime distribution of the fluorophore. The final selected candidates for multi-target FL-PAINT were Alexa-555, Cy3b, and Atto-550, as their lifetimes were sufficiently separated. Detailed information about lifetimes and brightness values of the different fluorophore-imager combinations can be found in Table 1 in Appendix.

4.3.5 *Data acquisition*

4.3.5.1 *Wide-field FL-PAINT*

Fluorescence lifetime imaging was performed on a custom-built optical setup equipped with a lifetime camera (LINCam, Photonscore), see Figure 4.4 in Appendix. The imager strands P1 5′-CTAGATGTAT-3′, P2 5′-TATGTAGATC-3′, and P3 5′-GTAATGAAGA-3′ (Eurofins Genomics) were labeled with Cy3b, Atto550 and Alexa555 fluorophores at the 3′ end. All imager strands were aliquoted in TE buffer (Tris 10 mM, EDTA 1 mM, pH 8.0) at a concentration of 100 μM and stored at $-20°$C. Prior to the experiment, the strands were diluted to the final concentration of 0.5 nM in PBS buffer, containing 500 mM NaCl. A chamber with eight wells (155411PK, Thermo Fisher Scientific) was fixed with clips on the microscope stage. A PDMS layer was used as chamber cover and supported the inlet tubes and one tube for suction. The slide was held on the microscope stage for 0.5 h before acquisition to allow thermal equilibration to room temperature and to avoid subsequent mechanical drift. First, the well was rinsed twice with 500 µL PBS buffer (pH 8.0, NaCl 500 mM). Then using an emCCD camera, suitable cell was selected for imaging, based on the presence of the signal from expressed fluorescent proteins: mTagBFP, mCherry and EGFP. Afterwards, we proceeded with FL-PAINT of the selected cell. All solutions were injected into the well by applying a pressure gradient to the corresponding tube. Mix of imager strands P1, P2 and P3 with final concentration of 0.2 nM in PBS buffer were injected into a well and incubated for 5-10 min before image acquisition. The laser power was adjusted according to sample brightness to around 1-2 mW (output of optical fiber). A HILO-illumination scheme was used for fluorescence excitation. In the emission path, a neutral density (ND) filter with optical density 0.3 (Absorptive ND Filter, Thorlabs) was used to reduce the fluorescence signal for avoiding overheating of the camera sensor. Image magnification was set to 222×, resulting in the partitioning of the LINCam's field of view into 1024 × 1024 pixels corresponding to an effective pixel size in sample space of 95.8 nm. The single molecule lifetime analysis was performed as described in the "Data analysis section". All experiments were done at a constant temperature of 22°C. This was crucial for the mechanical stability of the optical setup. Typical acquisition time per image varies between 45 minutes and 1 hour, depending on the final concentration and brightness of fluorophores used for imaging.

4.3.5.2 *CLSM FL-PAINT*

Fluorescence lifetime measurements were performed on a custom-built confocal setup, see Figure 4.4 in Appendix. Typically, 5000 scan images with a virtual pixel size of 100 nm, a dwell time of 5 μs/pixel, and a TCSPC time resolution of 16 ps were recorded. Typical total acquisition time was around 1-1.5 hours for a 20 μm × 20 μm scan region. Mix of imager strands P1 and P3 with final concentration of 0.1 nM in PBS buffer were injected into the well and incubated for 5-10 min before image acquisition.

4.3.6 *Data analysis*

Single-molecule lifetimes analysis was performed using an upgraded version of a custom-written MATLAB-based GUI program. The original version of this GUI program was published elsewhere [89], and the version suitable for analysing both wide-field and confocal FL-PAINT data, which was used in for the present paper, can be freely downloaded from GitHub (`https://github.com/scstein/TrackNTrace`). The package includes a data visualiser capable of generating single-molecule localizations, performing drift correction, and reconstruction of super-resolved FLIM images for both data types (wide-field and confocal).

For confocal data analysis, we chose a time binning of 8 time frames for a pixel dwell time of 2.5 μs. For a 20 μm × 20 μm scan region, total image acquisition time was around 1-1,5 hours (corresponding to a framerate of 10 Hz). The imager binding events detection and refinement were done with the Cross correlation and TNT Fitter plugin. TNT NearestNeighbor selected the time traces based on minimum track length, maximum tracking radius and no gap closing. The lifetime fitting was performed with the feature fit lifetime. For the purpose, the TCSPC curves were fitted by a mono-exponential maximum likelihood estimation (MLE) with a cutoff of 0.1 ns. Only lifetimes in the range from 0.5 to 5.0 ns were taken into account. The emitters detected in a single frame only were discarded. In addition, the localizations with a PSF width of more than 180 nm or a number of photons smaller than 100 were rejected. Finally, a drift correction was applied and the super-resolved image was reconstructed.

For the wide-field FL-PAINT data analysis, we chose a spatial binning of 8 pixels (corresponds to a virtual pixel size of 192 nm) and a time bin of 500 ms. Same localisation parameters as for the confocal FL-PAINT were used for image reconstruction, besides the TCSPC cutoff time, which was set to 0.3 ns. Again, emitters detected in a single frame were discarded. Also, localisations with a PSF width of more than 180 nm or a number of photons smaller than 100 were rejected as well. After that, drift correction was applied and a super-resolved image was reconstructed.

4.4 RESULTS

4.4.1 *Wide-field FL-PAINT*

Recent improvements in the performance of photo-multiplier tubes (PMT) lead to the development of a commercial lifetime camera (LINCam, Photonscore) with large diameter of the detector (25 mm) and high signal-to-noise ratio. We recently demonstrated that detection of single molecules is possible even in the far-red spectral range [79], which is the most challenging spectral range for the camera. Because its quantum yield (QY) in this region is only about 2%. We were able to identify individual fluorophores in a mixture of three different dyes with similar emission spectra based solely on the fluorescence lifetime. In the current paper, we switch to fluorophores in the green spectral region where the camera's QY is ∼12%. Highly inclined and laminated optical sheet (HILO) illumination was used in order to improve the signal-to-background ratio. As a proof-of-concept experiment, we performed FL-PAINT imaging on two targets in fixed HeLa cells: peroxisomes labeled with the P1 docking strand, and mitochondria labeled with the P3 docking strand, see Figure 4.1. In contrast to Exchange-PAINT, where imagers are introduced sequentially, in FL-PAINT the targets are imaged simultaneously while using imagers with fluorophores of different lifetimes. When reconstructing a super-resolution image, arrival times of photons were used to create a Time-correlated Single Photon Counting (TCSPC) curve for each binding event and to obtain its lifetime value, see Figure 4.1b. The resulting lifetime histogram shows peaks at values corresponding to the different fluorophores conjugated to the imagers: P1-Alexa 555 and P3-Atto 550 for mitochondria and peroxisome respectively (Figure 4.1c). The exceptionally good separation between the two peaks in the lifetime histogram allows fpr a straightforward target identification with negligible cross-talk (Figure 4.1d and e for multiplexed FL-PAINT and Figure 4.1f and g for each target separately).

To optimize FL-PAINT, we examined the imaging quality for different combinations of fluorophores conjugated to imager strands. For this purpose, we performed two-target FL-PAINT imaging of HeLa cells, with the following dye-imager combinations: P1-Alexa 555/P3-Cy3b (Figure 4.2a), and P1-Atto 550/P3-Cy3b (Figure 4.2c). Imager P1 targeted peroxisomes, while imager P3 targeted mitochondria. Lifetime values for identified imager binding events were determined as described in the "Methods" section, and the resulting lifetimes were

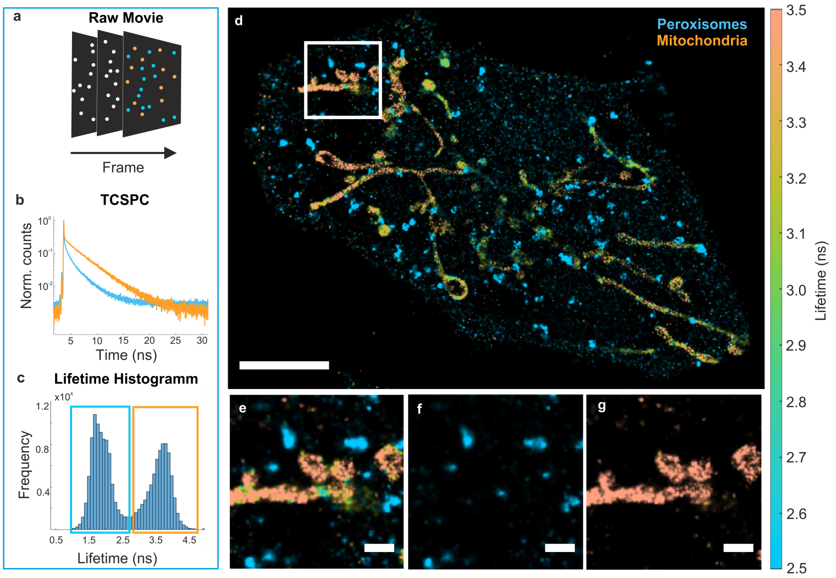

Figure 4.1: Multiplexed FL-PAINT imaging of a fixed cell. (a) Stack of DNA-PAINT frames with single-molecule localisations. Alexa 555 is depicted in blue color and Atto 550 in orange color. (b) TCSPC curves of the two fluorophores obtained by adding all single-molecule localisations of the same type. The colors correspond to single-molecule image colors in (a). (c) Lifetime histogram of two-target FL-PAINT of HeLa cell. The mixture of imagers P1-Alexa 555 and P3-Atto 550 allowed for a remarkable separation between the lifetimes of two targets, depicted by blue and orange rectangles. (d) Reconstructed FL-PAINT image of HeLa cell. The lifetime color bar appears on the right hand side of the FL-PAINT image. Scale bar is 5 μm. (e) Magnification of white frame in the primary image. A lifetime threshold was used to separate the targets into two images: peroxisomes (f) and mitochondria (g). Scale bar is 1 μm.

histogrammed as shown in Figures 4.2b and d. In both cases, the histograms had two prominent peaks, making target identification and localisation disentanglement straightforward. In a next step, we performed three-target imaging of HeLa cell (Figure 4.2e-f). In this case, P1-Alexa 555, P2-Atto 550 and P3-Cy3b were used to target peroxisomes, endoplasmic reticulum, and mitochondria, respectively. Detailed information on the possible combinations of imagers with different fluorophores and the obtained average lifetimes for each target are summarised in Table 4.2 in the supplementary information (SI). A library of additional FL-PAINT images of HeLa and COS-7 cells obtained with different combinations of imagers are shown in Figure 4.6 in the SI. The quality of the single-target images generated from the FL-PAINT image can be further improved by applying a Bayesian pattern matching algorithm, where reference measurements with single targets were used to obtain reference TCSPC curves for each target. This algorithm was applied to the mixed target data, assigning target probabilities for each binding event. Further details and images generated with the algorithm are shown in the Figure 4.7 in Appendix.

To estimate the quality of FL-PAINT images, we performed a detailed analysis of the localisation precision for each measurement. For the cells shown in Figure 4.1 and Figure 4.2, the average localization precision varied around 18 nm. The localization precision is lower than that achieved in conventional cellular PAINT imaging [87], which we attribute to the low quantum efficiency of the lifetime camera.

Because the quantum efficiency of the camera drops at photon rates of more then $\sim$ 700 kcounts/s, neutral density filters were used to adjust the photon detection rate to a value optimal for the lifetime camera. The optimal photon rate was set to $\sim$ 500 kcounts/s. This value was chosen in accordance with manufacture's instruction to increase the lifespan of the camera. Measurements performed for estimating the experimental dependency between the number of detected photons and the localisation accuracy show that single-molecule imaging and localization is possible even when detecting only 10% of the photons arriving at the detector. These results are summarized in Table 4.3 and Figure 4.8 in the Appendix.

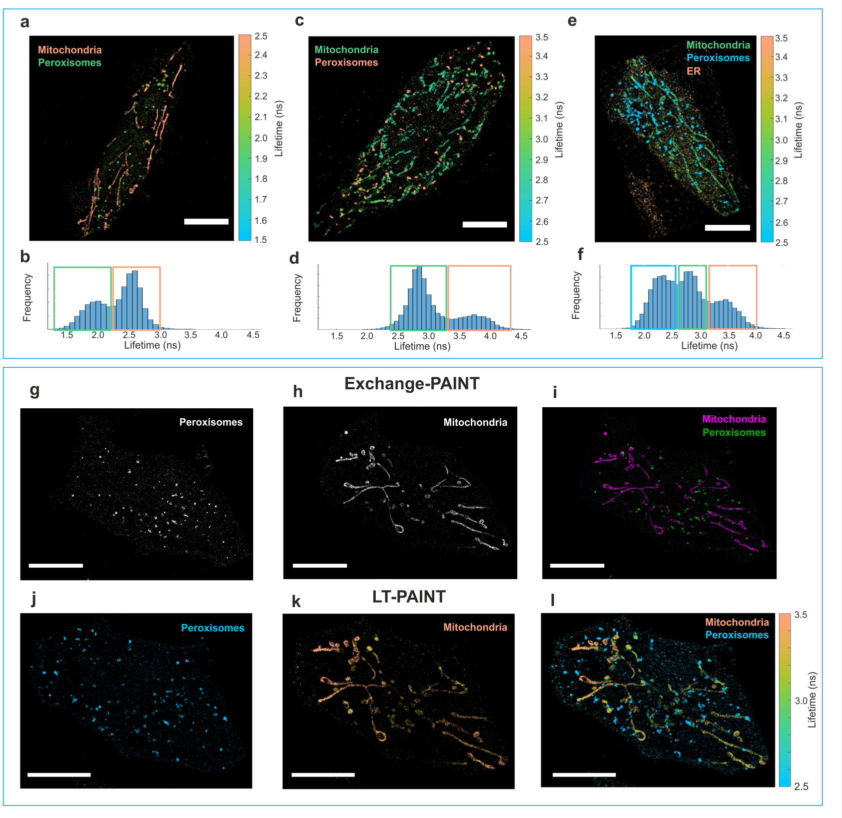

Figure 4.2: (a-f) Two- and three-target FL-PAINT of HeLa cells using wide-field FLIM. (a) Two target FL-PAINT image: peroxisomes and mitochondria labeled with imagers P1-Alexa 555 and P3-Cy3b. (b) Lifetime histogram for the HeLa cell shown in (a). The two peaks in the lifetime histogram correspond to the two targets: mitochondria and peroxisomes. (c) Two target FL-PAINT image: peroxisomes and mitochondria labeled with the two imagers P1-Atto 550 and P3-Cy3b. (d) Lifetime histogram for the HeLa cell shown in (c). (e) Three-target FL-PAINT image: peroxisomes, endoplasmic reticulum, and mitochondria labeled with the three imagers: P1-Alexa 555, P2-Atto 550 and P3-Cy3b, respectively. (f) Lifetime histogram of the FL-PAINT image shown in (e). The blue, green and orange rectangles show the two or three lifetime ranges associated with the different targets. The lifetime color bar is shown on the right hand side of the lifetime images. Scale bars are 10 μm. (g-l) FL-PAINT validation with Exchange-PAINT. (g-i) Exchange-PAINT image of HeLa cell with two targets: peroxisomes (g) and mitochondria (h). (i) Overlay of the two DNA-PAINT images. (j-l) FLPAINT image of the same HeLa cell with two targets. (j) Reconstructed single-target image of mitochondria. (k) Reconstructed single-target image of peroxisomes. (l) Combined two-target FL-PAINT image. Scale bars in (g-l) are 5 μm.

4.4.2 *WF-FL-PAINT validation with Exchange-PAINT*

Next, we validated FL-PAINT against Exchange-PAINT commonly used for multiplexed cellular DNA-PAINT imaging. For this purpose, we used HeLa cells with two labeled targets. For both Exchange-PAINT and FL-PAINT, exactly the same imagers were used: P1-Atto 550 (targeting mitochondria) and P3-Cy3b (targeting peroxisomes). First, we performed Exchange-PAINT imaging with two cycles: first cycle peroxisomes (Figure 4.2g), thorough washing, and then mitochondria (Figure 4.2h). For solution exchange, a microfluidic system was employed, as described previously [87]. An overlay of the two images can be seen in Figure 4.2i. Then, we performed FL-PAINT imaging of the same HeLa cell. The sample chamber was washed with the buffer solution and filled with the mixture of two imagers used in Exchange-PAINT but with 5 times lower concentration of each imager strand. The emission light was redirected from the emCCD camera to the lifetime camera. The total acquisition time of the two-target Exchange-PAINT experiment was 70 minutes, close to two-fold longer then the FL-PAINT experiment (40 min). The resulting FL-PAINT image and the corresponding lifetime histogram are shown in Figure 4.2l. Lifetime thresholding was used to separate the two targets in the FL-PAINT image into two separate images: peroxisomes in Figure 4.2j and mitochondria in Figure 4.2k.

4.4.3 *CLSM-based FL-PAINT*

As alternative to the costly and thus not widely available LINCam used above, we next demonstrate the feasibility of FL-PAINT using a CLSM capable of TCSPC measurements [80]. As sample we use again HeLa cells labeled with a mixture of the two imagers P1-Atto 550 and P3-Cy3b, which were injected into the sample chamber, similarly to what was described for wide-field FLIM. Fast scanning with frame rate of 5-10 Hz was performed in order to collect a sufficient number of photons from each binding event. A typical lifetime image is shown in Figure 4.3a. In the corresponding lifetime histogram, two distinct peaks are visible, corresponding to the two targets - peroxisomes and mitochondria, see Figure 4.3b.

One of the main benefits of CLSM is its ability of optical sectioning, which allows to acquire three-dimensional images. We demonstrate two-target 3D FL-PAINT by imaging HeLa cells with P1-Alexa 555 and P3-Atto 550 imagers. Image acquisition was performed across a 3 μm z-stack with steps of 500 nm. The resulting two target FL-PAINT images in different planes of the z-stack are displayed in Figure 4.3c. Based on the lifetime values we sorted localized single-molecules into two subgroups corresponding to mitochondria (Figure 4.3d) and per-

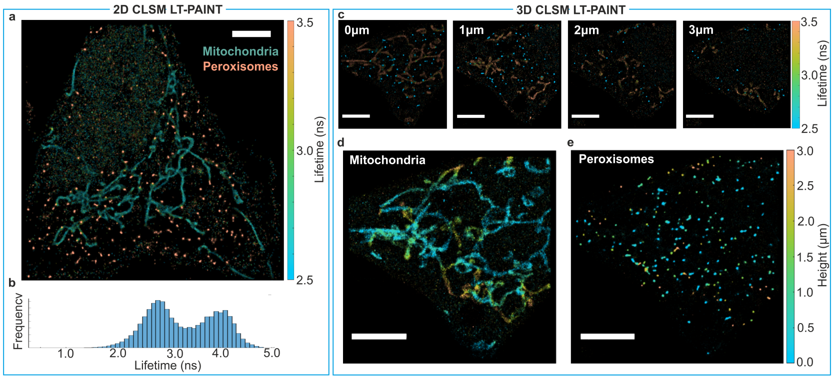

Figure 4.3: 2D and 3D FL-PAINT using a CLSM. (a) 2D CLSM FL-PAINT image of a HeLa cell with two targets: mitochondria and peroxisomes, labeled with the imagers P1-Atto 550 and P3-Cy3b. (b) The corresponding lifetime histogram is shown in (a). (c) 2D CLSM FL-PAINT images of a HeLa cell with two targets labeled with P1-Alexa 555 and P3-Atto 550 imagers. The images correspond to focal planes at 0 μm, 1 μm, 2 μm and 3 μm axial distances above coverslip. (d-e) 3D FL-PAINT images of mitochondria and peroxisomes in the HeLa cell from (c). Z-projections of the separated images for mitochondria (d) and peroxisomes (e). Here, color represents the height. Lifetime and height color bars are shown on the right hand side of the images. Scale bar is 5 μm.

oxisomes (Figure 4.3e).

CLSM is advantageous when imaging relatively small regions of interest - 20 μm × 20 μm or less. CLSM is also the method of choice for imaging fluorophores in the red spectral region, where the LINCam's quantum yield becomes very low. In this study, we chose fluorophores in a green spectral region as they are suitable for both CLSM-based imaging and WF-FLIM.

4.5 CONCLUSIONS

In summary, we developed and validated FL-PAINT, by combining DNA-PAINT with FLIM. FL-PAINT is particularly suitable for multiplexed DNA-PAINT imaging. Due to the robustness of lifetime-based target identification, FL-PAINT is insensitive to the binding kinetics of imager to its complementary docking strand. Also, the sample is not disturbed during data acquisition, as no buffer exchange (and consequently a dedicated microfluidics system) is needed. Furthermore, in FL-PAINT multiple targets are imaged simultaneously, therefore shortening the total acquisition time. We implemented FL-PAINT using both WF-FLIM (equipped with commercially available lifetime camera) and CLSM (equipped with TCSPC electronics and fast laser scanning). In contrast to multiplexed DNA-PAINT using kinetic barcoding, FL-PAINT performs exceptionally well in a dense and sticky environment inside a cell. We identified also a combination of three bright fluorophores with similar emission spectra in the green spectral range, but with different lifetimes, which are the perfect choice for simultaneous two- and three-target FL-PAINT. We emphasize that FL-PAINT uses fluorophores in the same spectral range and is therefore not affected by chromatic aberration. On the experimental side, a single pulsed laser and a single emission band pass filter are required for imaging of the multiple fluorophores. For an improved separation and reconstruction of single-target images from an FL-PAINT image, a Bayesian pattern-matching algorithm was employed. We anticipate that FL-PAINT has great potential for multiplexed super-resolution bio-imaging. Furthermore, FL-PAINT provides fluorescence lifetime information, making it attractive for single-molecule FRET and metal-induced energy transfer imaging.

4.6 APPENDIX

OPTICAL SETUPS

Wide-field setup

Excitation was done using a pulsed super-continuum white light laser (Fianium WhiteLase SC450, NKT Photonics) with a pulse repetition rate of 20 MHz. A custom photodiode (PD) was employed to optically trigger the TCSPC-based camera. A custom photodiode (PD) was employed to optically trigger the TCSPC-based camera. White light laser source in combination with clean-up filters (ZET 640/10, Chroma; BrightLine HC 563/9, Semrock; ZET 488/10, Chroma) was used to excite fluorophores with different excitation spectra (blue, green and red). Neutral density filters (NE10A-A,NE20A-A, Thorlabs) and a variable neutral density filter (ND) (NDC-50C-4-A, Thorlabs) were used for adjusting the laser excitation power. The laser beam was coupled into a single-mode optical fiber (P1-460B-FC-2, Thorlabs) with a typical coupling efficiency of 50%. The collimated laser beam was expanded by a factor of 3.6X using telescope lenses after the fiber. The beam was focused onto the back focal plane of the TIRF objective (UAPON 100× oil, 1.49 NA, Olympus) using an achromatic lens (f = 200 mm, AC508-200-A-ML, Thorlabs). Switching between direct and Total Internal Reflection (TIR) illumination was achieved by shifting the beam with respect to the objective lens using a translation stage (LNR50M, Thorlabs). Fluorescence emission was collected using the same objective lens. Samples were placed onto a XY translation stage (M-406, Newport). An independent one-dimensional translation stage (LNR25/M, Thorlabs) was equipped with a differential micrometer screw (DRV3, Thorlabs) for axially moving the objective lens for focusing. Collected fluorescence light was spectrally decoupled from scattered excitation laser light using a multiband dichroic mirror (Di03 R405/488/532/635, Semrock) and band-pass filters (BrightLine HC 692/40, Semrock; BrightLine HC 615/45, Semrock; BrightLine FF 536/40, Semrock). A tube lens (AC254–200-A-ML, Thorlabs) focused the light on an adjustable slit aperture (SP60, OWIS). The latter was employed to select a region of interest within the field of view. Two lenses (AC254-100-A and AC508–150-A-ML, Thorlabs) were used to focus the light onto an emCCD camera (iXon Ultra 897, Andor). Similarly, lens L5 (AC508-250-A-MC, Thorlabs) re-imaged the light onto the lifetime camera (LINCam, Photonscore). Switching between the two cameras was attained by using a dielectric mirror (BB1-E02, Thorlabs) fixed to a magnetic base plate MB (KB50/M, Thorlabs) with removable top.

Confocal setup

Fluorescence lifetime measurements were performed on a custom-built confocal setup. For excitation, a white light laser (Fianium WhiteLase SC450, NKT Photonics) was used. The laser beam was coupled into a single-mode fiber (PMC-460Si-3.0-NA012–3APC-150-P, Schäfter + Kirchhoff) with a fiber-coupler (60SMS-1-4-RGBV-11-47, Schäfter + Kirchhoff). After the fiber, the output beam was collimated by an air objective (UPlanSApo 10× /0.40 NA, Olympus). After passing thought a clean-up filter (BrightLine HC 563/9), an ultraflat quad-band dichroic mirror (ZT405/488/561/640rpc, Chroma) was used to direct the excitation light into the microscope. The excitation beam was directed into a laser scanning system (FLIMbee, PicoQuant) and then into a custom side port of the microscope (IX73, Olympus). The three galvo mirrors in the scanning system are deflecting the beam while preserving the beam position in the back focal plane of the objective (UApo N 100× /1.49 NA oil, Olympus). The sample position can be adjusted a using manual XY stage (Olympus) and a z-piezo stage (Nano-ZL100, MadCityLabs). Fluorescence light was collected by the same objective and descanned in the scanning system. Afterwards, an achromatic lens (TTL180-A, Thorlabs) was used to focus the beam onto a 100 μm pinhole (P100S, Thorlabs). Excitation laser light was blocked in the emission path by a long-pass filter (647 LP Edge Basic, Semrock). Next, the emission light was collimated by a 100 mm lens. A band-pass filter (BrightLine HC 615/45) was used to reject scattered excitation light. Finally, the emission light was focused onto a SPAD-detector (SPCM-AQRH, Excelitas) using an achromatic lens (AC254–030-A-ML, Thorlabs). The output signal of the SPAD-detector was recorded by a TCSPC system (HydraHarp 400, PicoQuant) which was synchronized with the triggering signal from the excitation laser. Measurements were controlled with a dedicated software (SymPhoTime 64, PicoQuant), which controlled both the TCSPC system and the scanner system.

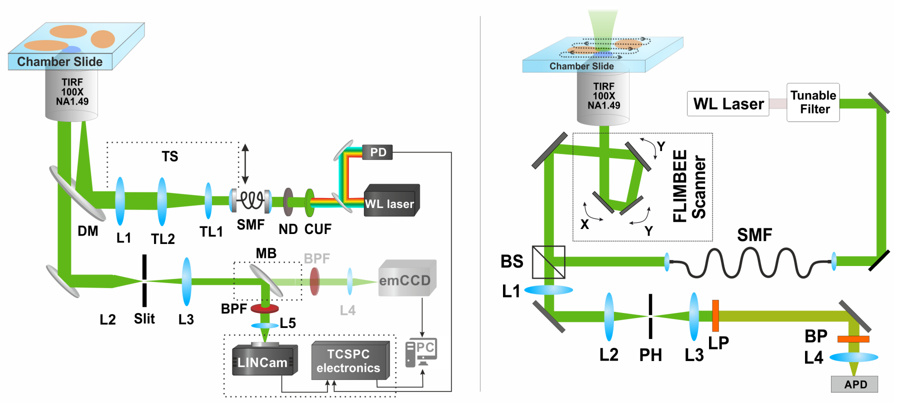

Figure 4.4: Experimental FLIM techniques compatible with FL-PAINT. (A) Conventional wide-field microscope equipped with lifetime camera. (B) Confocal-based laser scanning microscope equipped with TCSPC electronics and fast scanner.

EXCHANGE-PAINT IMAGING

To validate the performance of FL-PAINT, we compared it with Exchange DNA-PAINT using a custom-built optical setup with a conventional emCCD camera. Injection and removal of solutions was done using our custom-built microfluidics setup, designed and constructed particularly for Exchange PAINT [87]. First, imager strand P1 (0.5 nM) diluted in PBS buffer with NaCl 500 mM (500 μL) was injected into the chamber and incubated for 5-10 min before image acquisition. A typical DNA-PAINT movie included 20000 frames, which corresponds to $\sim$30 min acquisition time. The following settings for the emCCD camera were used: exposure time 100 ms, pre-amplifier gain 3.0, EM gain 100. After a first round of image acquisition, the imager P1 was removed from the chamber by extensive washing of the well with the imaging buffer (4–6 times the chamber volume, in total about 2 mL buffer within 5 min). After washing, the next imager solution was introduced. Same solution exchange procedure was applied also for the imager P3. The total optical magnification of the setup was 166.6×, resulting in an effective pixel size in sample space of 103.5 nm. Recorded images were analyzed with the ImageJ plugin ThunderSTORM [90] for determining the positions of single emitters and reconstructing a super-resolution image. In all experiments, the same parameters were used for emitter localizations and subsequent super-resolution image reconstruction.

LIFETIMES OF FLUOROPHORES CONJUGATED TO THE IMAGER STRANDS

Lifetimes of fluorophores are affected by the presence of single-stranded DNA in a sequence-dependent manner. We systematically measured the lifetimes of fluorophores attached to all the imager strands that we used. The results are displayed in the Table below.

Imager strand	Dye	Lifetime (ns)	Brightness (photons)
P1	Alexa 555	1.80 ± 0.22	511
P1	Atto 550	3.44 ± 0.26	1318
P2	Alexa 555	1.58 ± 0.11	751
P2	Atto 550	3.81 ± 0.31	1402
P3	Cy3B	2.82 ± 0.16	1117
P3	Atto 550	3.77 ± 0.3	1778

Table 4.1: Lifetime values of DNA-bound (imager) molecules measured with the LINCam.

CELLULAR LIFETIME DNA-PAINT IMAGING

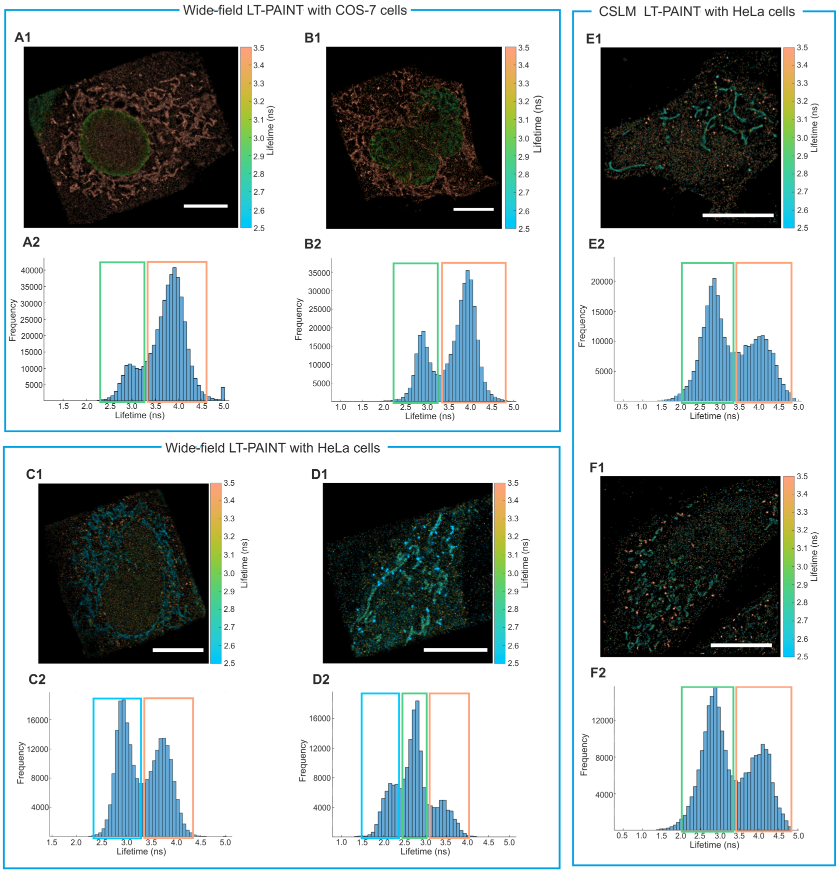

Figure 4.5: FL-PAINT images of HeLa and COS-7 cells. Scale bar is 10 μm.

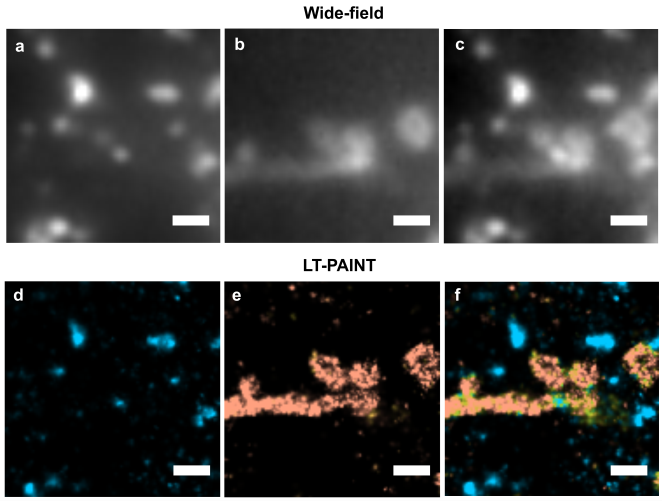

Figure 4.6: (a-c) Diffraction-limited wide-field images of individual targets: peroxisomes-mTagBFP (a) and mitochondria-EGFP (b). (c) Merged wide-field image. (d) Two-target FL-PAINT image of peroxisomes and mitochondria. Lifetimes were used to separate the targets into two images: peroxisomes (f) and mitochondria (g). Scale bar is 1 μm.

Cell	Setup	Imagers	Lifetimes (ns)	OD filter	Loc.precision (nm)
Fig. 1	LINCam25	p1-Alexa 555 p3-Atto 550	1.85 ± 0.23 3.77 ± 0.3	0.3	17.6
Fig. 2 A	LINCam25	p1-Alexa 555 p3-Cy3B	1.92 ± 0.18 2.54 ± 0.21	0.3	21.2
Fig. 2 B	LINCam25	p1-Atto 550 p3-Cy3B	3.7 ± 0.28 2.83 ± 0.18	0.6	20.8
Fig. 2 C	LINCam25	p1-Alexa 555 p2-Atto 550 p3-Cy3B	2.29± 0.2 3.42 ± 0.26 2.80 ± 0.15	0.3	22.9
Fig. 3 A	CSLM	p1-Atto 550 p3-Cy3B	3.97 ± 0.38 2.8 ± 0.3	-	10.9
Fig. S3 A	LINCam25	p1-Atto 550 p3-Cy3B	3.76 ± 0.27 2.92 ± 0.19	0.6	23.5
Fig. S3 B	LINCam25	p1-Atto 550 p3-Cy3B	3.79 ± 0.23 2.87 ± 0.18	0.6	17.5
Fig. S3 C	LINCam25	p1-Atto 550 p3-Cy3B	3.71 ± 0.22 2.91 ± 0.16	0.6	19.9
Fig. S3 D	LINCam25	p1-Alexa 555 p2-Atto 550 p3-Cy3B	2.26 ± 0.26 2.75 ± 0.13 3.36 ± 0.28	-	17.5
Fig. S3 E	CSLM	p1-Atto 550 p3-Cy3B	3.94 ± 0.3 2.79 ± 0.33	-	10.1
Fig. S3 F	CSLM	p1-Atto 550 p3-Cy3B	4.00 ± 0.32 2.87 ± 0.32	-	10.4

Table 4.2: Detailed description of setup, imagers, obtained lifetimes, neutral density filters and localization precision for each measured cell.

PATTERN MATCHING ANALYSIS

Our pattern matching analysis is a Bayesian model comparison assuming equal prior probabilities for all species. The analysis was performed as described previously [80].

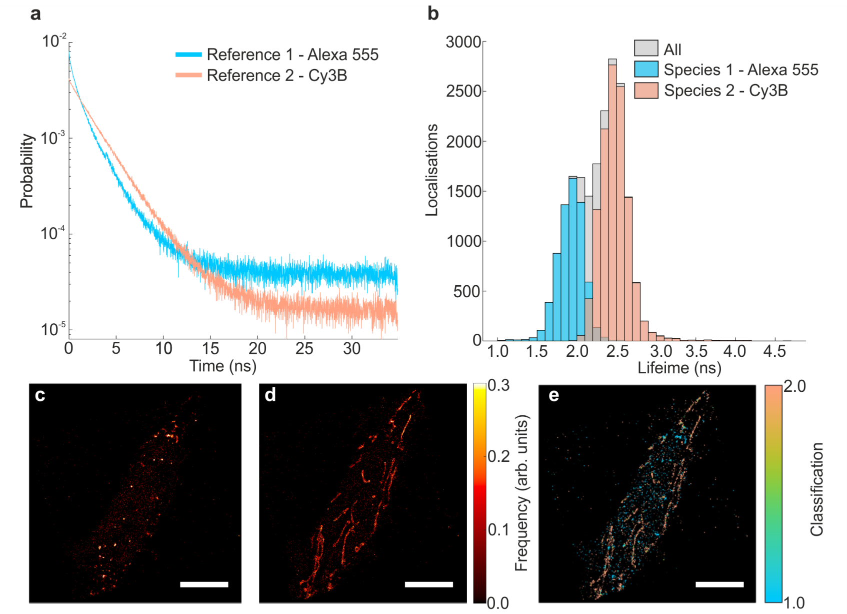

Figure 4.7: Pattern matching analysis approach. (a) Reference TCSPCs measured from samples with only one imager strand (b) Lifetime histograms obtained from individual single-molecule localisations for peroxisomes labeled with Alexa 555 and mitochondria labeled with Cy3B. (c-d) Super-resolved DNA-PAINT images of localizations classified as (c) Alexa 555 and (d) Cy3B. All images share the same intensity scale which is proportional to the local number of localizations. (e) Super-resolved probability image obtained by pattern matching analysis. Scale bar is 10 μm.

THE EFFECT OF PHOTON DETECTION COUNT-RATE ON LIFETIME DETERMINATION ACCURACY AND LOCALIZATION PRECISION

In order to evaluate the impact of decreasing photo detection count-rate on the accuracy of the lifetime determination and the resolution of final super-resolution image, we placed neutral density filters with different optical densities into the optical path of the emission. In this way, we adjusted the photon detection count-rate of the LINCam, while keeping the excitation laser and imaging parameters unchanged. Optical densities were kept in the range between 0 and 1, resulting in a transmission of 100%, 50%, 25% and 10%, respectively. Imager strand P3-Cy3b (concentration 0.5 nM) in PBS buffer (500 μL) was used for the measurement. Each FL-PAINT dataset included 13500 frames with 200 ms exposure time (corresponds to 45 min).

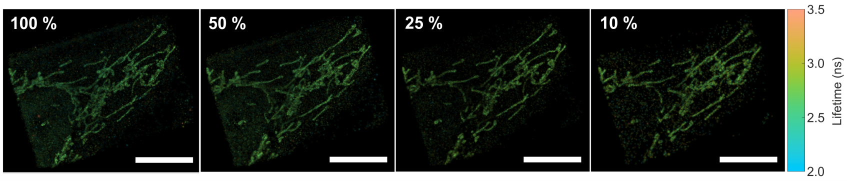

Figure 4.8: Effect of emission photon detection count-rate on lifetime accuracy and localization precision. Scale bar is 10 μm.

Optical density (OD)	0	0.3	0.6	1.0
Lifetime error (ns)	0.13	0.14	0.15	0.23
Average localization precision (nm)	16	18.9	20.2	22.4

Table 4.3: Effect of emission photon detection count-rate on lifetime accuracy and localization precision

5

DISCUSSION AND OUTLOOK

In this work, I have developed and optimized techniques for multiplexed super-resolution imaging, with the focus on DNA-PAINT, which is one of the most promising SMLM techniques.

In Chapter 2, I have presented a custom-built computer-controlled microfluidics setup, which enabled precise control of a cell's environment in a fully automated regime. The system is designed and optimized particularly for Exchange-PAINT. The setup allows the operation of a theoretically unlimited number of microfluidic channels and is capable of exchanging fluids inside the experimental chamber with adjustable flow speed. As part of this project, a versatile custom-built optical setup for multi-color detection was designed and constructed. For further improvement of the localization accuracy in DNA-PAINT imaging, single-domain antibodies were used. With these so-called nanobodies, the linkage error is significantly smaller than when using more conventional full-sized antibodies, due to the smaller size of the nanobodies. In particular, I used three specific nanobodies against three common fluorescent protein: EGFP, mCherry, and mTagBFP. I used TOM70 fused to EGFP to tag mitochondria, GalNacT was fused to mCherry to label the Golgi apparatus, and histone H2B was fused to mTagBFP to detect nuclear chromatin. I obtained super-resolved images of these three targets with an overall resolution of 20 nm, and an average localization precision of around 14 nm, within 30 minutes acquisition time per single target.

In Chapter 3, I characterized the performance of a novel, commercially available wide-field lifetime camera (LINCam25, Photonscore) for Fluorescence Lifetime Imaging Microscopy (FLIM) with single molecule sensitivity. To explore the lifetime camera's potential for imaging in a far-red spectral region, I recorded wide-field FLIM images of three commonly used fluorophores: Cy5, Atto 655 and Atto 647N. These fluorophores have similar emission spectra but differ in their lifetimes. Although the camera's quantum yield of photon detection is only about 2 % in the far-red spectral region, I was able to determine fluorescence lifetimes of individual molecules. This was performed by fitting the recorded Time-Correlated Single Photon Counting (TCSPC) data on a molecule-by-molecule basis. Using these fitted lifetime values, I successfully identified different molecular species in a mixed sample of all three fluorophores. To my knowledge, this is currently the only wide-field lifetime imaging system with single-molecule sensitivity and a sub-nanosecond temporal resolution. I compared the performance of this wide-field FLIM system with that of a conventional TCSPC-based Confocal Scanning Laser Microscope (TCSPC-CSLM). For that purpose, I conducted measurements of the same mixed fluorophore sample with TCSPC-CSLM and wide-field FLIM, and found a remarkable agreement between both cases. As compared to TCSPC-CLSM, the LINCam has the advantage of faster data acquisition. This advantage becomes even more striking in the blue and green spectral regions, due to the higher quantum efficiency of the camera in these spectral regions compared to the red spectral region. In addition, I used the LINCam for Metal-Induced Energy Transfer (MIET) imaging. MIET allows us to determine the axial positions of individual molecules with nanometer accuracy. Thus, my work is a first step towards three-dimensional single-molecule localization microscopy (SMLM) with isotropic nanometer accuracy. I did also implement an on/off-state-detection algorithm and dwell-time analysis to characterize Atto 655 blinking at low laser power conditions. The ability to detect fast blinking kinetics of single emitters makes the realization of SMLM with TCSPC-based lifetime determination attainable and leads us to the next chapter.

In Chapter 4, I developed a novel fluorescence lifetime imaging super-resolution technique, which I call Fluorescence Lifetime PAINT (FL-PAINT). The technique uses fluorescence lifetime information for multiplexed DNA-PAINT imaging. Complex environments inside cells often affect the photochemical/photophysical properties of fluorophores, making multiplexed dSTORM imaging extremely challenging. Therefore, FL-PAINT is particularly efficient for multi-target imaging of cells, due to the robustness of lifetime measurements of fluorescent dyes. Moreover, current multi-target cellular DNA-PAINT suffers both from poor control of binding kinetics, and from exceedingly long acquisition times. Multiplexing using FL-PAINT is based solely on the lifetime information and is therefore less sensitive to variations in binding kinetics, and due to parallel acquisition of multiple targets offers shorter acquisition times. In contrast to Exchange-PAINT, FL-PAINT does not require solution exchange for imaging of multiple targets. A mixture of different imagers allows for addressing multiple targets in parallel. Therefore, no flow channel or a fluidics system are required, which is advantageous for multi-target imaging of sensitive biological samples. I identified a combination of three bright fluorophores with lifetime values perfectly suited for multi-target identification in FL-PAINT imaging. The trio has similar emission spectra in the green spectral range, but exhibits different lifetimes. This makes FL-PAINT completely free from the chromatic aberration. I validated FL-PAINT with established Exchange PAINT and demonstrated FL-PAINT's capabilities by imaging two and three targets inside COS-7 and HeLa cell. I obtained super-resolved images of these three targets with an average localization precision of about 16 nm, within total acquisition time of 45 minutes. Finally, I presented a combination of FL-PAINT with CLSM for two-color 3D imaging of mitochondria and peroxisomes inside HeLA cells.

In conclusion, I presented three techniques: Exchange-PAINT with nanobodies, WF FLIM, and FL-PAINT, that all expand current multiplexing possibilities of super-resolution fluorescence microscopy. My approach to multiplexed DNA-PAINT addresses the challenges of acquisition time and linkage error in cellular super-resolution imaging. WF-FLIM and FL-PAINT offer chromatic aberration-free imaging using the novel lifetime camera. I demonstrated that FL-PAINT can be realized both with WF-FLIM and CLSM. Moreover, FL-PAINT can be readily combined with Exchange-PAINT, making highly multiplexed DNA-PAINT time-efficient while significantly simplifying the experimental procedures. I anticipate that these developments will facilitate investigations of complex biological systems using SMLM-based super-resolution techniques.

6

OTHER CONTRIBUTIONS

Throughout my PhD I have contributed to several additional projects, related to fluorescence lifetime imaging by using both time and frequency domain. These projects resulted in several publications, which are closely related to my main project. In this chapter, I will give a brief overview on these other projects.

6.1 CONFOCAL LASER-SCANNING FLUORESCENCE-LIFETIME SINGLE-MOLECULE LOCALISATION MICROSCOPY

In this work, we combined fluorescence-lifetime CLSM with SMLM (FL-SMLM) for single-molecule localization fluorescence-lifetime super-resolution imaging. This technique combines all the advantages of both CLSM and SMLM: confocal sectioning, shot-noise limited single-photon detection, pixel-free imaging, fluorescence lifetime imaging, and single-molecule sensitivity.

To demonstrate the feasibility of using CLSM for super-resolved cellular imaging, we applied the technique to DNA-PAINT. DNA-PAINT is a highly promising SMLM technique, which circumvents the basic limitation of most SMLM approaches: fluorophore photobleaching. It is achieved by replenishment of dye-labeled imager DNA-strands that reversibly bind to targets of interest, which are in turn labeled with complementary DNA-strands called docking strands. For DNA-PAINT, optical sectioning is critical for efficiently suppressing fluorescent background from freely diffusing imager strands. To demonstrate confocal laser-scanning DNA-PAINT, we imaged chromatin (histone H2B) in COS-7 cells (Figure 6.1 a-c) fused to mTagBFP, which was subsequently high-affinity labeled with DNA docking strands using anti-TagBFP nanobodies (Nanotag, FluoTag-Q). Using nanobodies for labeling minimizes the distance between dye and target, thus significantly reducing the so-called "linkage error", thus increasing the localization precision. ATTO 655 was used for DNA-PAINT because of its high brightness and low unspecific binding to both coverslip surface and cell organelles. Despite using reduced concentrations of imager strands (0.25 nM, an order of magnitude smaller than used in conventional PAINT), we accumulated a sufficiently large number of single-molecule localizations due to the dense packing of histone inside the nucleus. A typical single frame from a recorded movie is shown in Figure 6.1 a. Figure 6.1 b presents a comparison between super-resolved PAINT and conventional CLSM. The average localization precision of the reconstructed confocal laser-scanning DNA-PAINT image was 18 nm. The corresponding lifetime distribution for all localized molecules is shown in Figure 6.1 c. The lifetime value for imager-bound Atto 655 is longer than the lifetime of free Atto 655, which we attribute to a change in the local environment of the dye due to its conjugation to single-stranded DNA.

To demonstrate the optical sectioning capability as well as the fluorescence lifetime multiplexing of FL-SMLM, we recorded movies of polymer beads that were surface-labeled, via double-stranded DNA, with two different dyes: Alexa 647 and Atto 655 (Figure 6.1 d-f). In wide-field microscopy, we could not detect single molecule switching events when focusing on the center of the bead. In contrast, it was possible to detect switching events of single molecules using CLSM, to determine their fluorescence lifetimes, and to reconstruct a fluorescence-lifetime dSTORM image. It was possible to identify two beads solely based on the lifetimes of the labeling dyes: Alexa 647 having an average value of 1.4 ns and Atto 655 with 2.4 ns.

In summary, we developed confocal laser-scanning FL-SMLM. It offers both optical sectioning and lifetime information for super-resolution imaging. The technique is straightforward to implement on a commercial CLSM with TCSPC capability and fast laser scanning. We demonstrated FL-SMLM both with dSTORM and DNA-PAINT, which are the most commonly used SMLM modalities. The high lifetime resolution enables lifetime-based multiplexing within the same spectral window, allowing to distinguish different fluorescent labels solely by their lifetimes. In combination with the optical sectioning of a CLSM, this allows for chromatic aberration-free super-resolution imaging of multiple cellular structures. The additional lifetime information in FL-SMLM offers also the fascinating prospect of lifetime-based super-resolution FRET imaging, thus providing the possibility to disentangle fast dynamics from stationary intermediate states. Another potential application is to use the lifetime information for combining lateral super-resolution of SMLM with the superior axial super-resolution of Metal-Induced Energy Transfer (MIET) imaging. This could enable 3D super-resolution imaging with exceptionally high isotropic resolution for potential applications in structural biology.

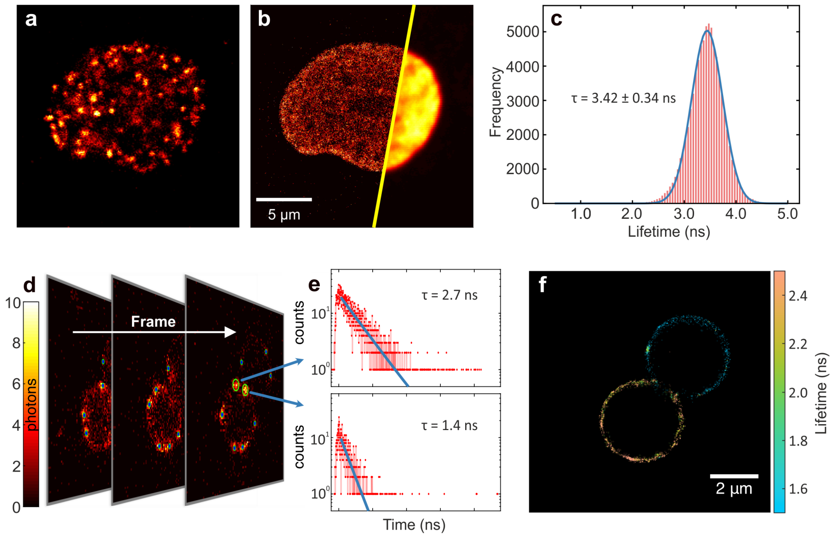

Figure 6.1: (a-c) Lifetime-based multiplexed dSTORM imaging of polymer beads labeled with two different dyes. (a) Typical frames from a recorded movie including single-molecule localizations. (b) Histogram of photon arrival times (TCSPC) for two indicated localizations. Lifetime is determined with a monoexponential fit (blue line). (c) Super-resolved image reconstruction including lifetime information. The two different lifetime values for molecules on both beads reveal that the beads are labeled with different fluorophores (Alexa 647 and ATTO 655). (d–f) Confocal laser-scanning DNA-PAINT images of cellular chromatin in COS-7 cells utilizing DNA-labeled ATTO 655. Imaging was performed at a height of around 6 μm above the coverslip surface. (d) Example of a single frame. (e) Corresponding diffraction-limited and super-resolved images. (f) Lifetime histograms, based on individual single-molecule localizations. The figure was reproduced from ref. [80].

6.2 EXFOLIATION AND OPTICAL PROPERTIES OF NEAR-INFRARED FLUORESCENT SILICATE NANOSHEETS

In this work, we investigated and characterized the optical properties of the following silicate nanosheets: Egyptian Blue ($CaCuSi_4O_{10}$, EB), Han Blue ($BaCuSi_4O_{10}$, HB), and Han Purple ($BaCuSi_2O_6$, HP). So far, the optical properties of nanosheets are poorly understood. Here, we exfoliated the bulk material into nanosheets and report their physicochemical properties. The exfoliation process included ball milling followed by tip sonication and centrifugation. The exfoliated nanosheets had a lateral size of around 16-27 nm and a thickness range of 1-4 nm. They emit photons at 927 nm (EB-NS), 953 nm (HB-NS) and 924 nm (HP-NS), while single nanosheets could be resolved in the NIR.

To confidently measure fluorescence lifetimes of nanosheets, we used both time domain and frequency domain measurements. First, we used Time-correlated Single-Photon Counting (TCSPC). Surprisingly, observed lifetime values spanned a range from microsecond to tens of microseconds. The data suggested a two-component fluorescence decay. We attributed the short lifetime component to a light scattering, which is in the same time scale as the width of Instrument Response Function (IRF). The longer lifetime components were $16.5 \pm 0.25\ \mu s$, $8.25 \pm 0.15\ \mu s$ and $9.91 \pm 0.06\ \mu s$ for EB-NS, HB-NS and HP-NS, respectively. This values are significantly shorter than the lifetimes of the bulk material: EB=130 μs, HB=60 μs, HP=25 μs, as confirmed by frequency-domain measurements (Figure 6.2). A possible explanation for the observed decrease in lifetime could be the presence of defects, or alternatively, changes in symmetry that either open new non-radiative decay channels, or increase the radiative rate constants.

The different fluorescence lifetimes observed for the different nanosheets carries great potential for multiplexed imaging. The μs lifetimes range of silicate NS are significantly longer than those of typical organic fluorophores (nanoseconds) used in FLIM. As a part of this project, our wide-field setup was extended and adapted for frequency-domain fluorescence lifetime imaging microscopy (FD-FLIM). Briefly, laser excitation was modulated by a square signal coming from the camera. The phase-shift and modulation depth change of fluorescence signal, recorded by a FLIM camera, were converted into a lifetime value. This allows to acquire an instantaneous fluorescence lifetime image, in contrast to scanning that has to measure lifetimes pixel by pixel. Before imaging, calibration with a sample of known lifetime had to be measured in order to extract absolute lifetime values from the images. Therefore, an independent lifetime measurement of a single nanosheet was required. For calibration purposes, we used TCSPC as described

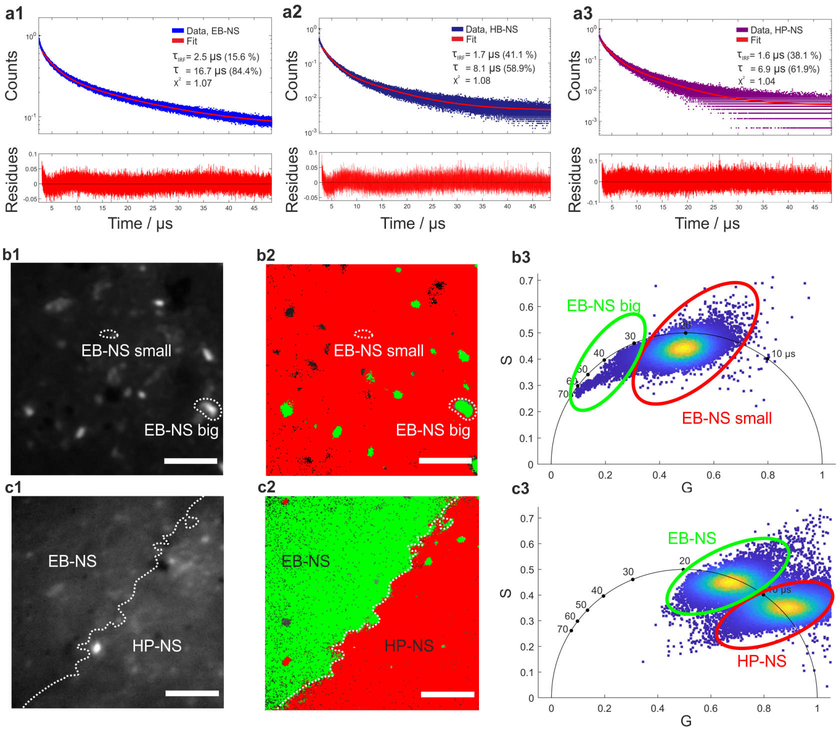

Figure 6.2: (a1-a3) Confocal time-correlated single-photon counting TCSPC-based measurements of fluorescent lifetimes of single NS diffusing freely in a solution. Exemplary decay curves of EB-NS (a1), HB-NS (a2) and HP-NS (a3), and the corresponding bi-exponential fits. Note that the short lifetime component corresponds to the instrument response function. Fit residues are given below the plot. (b1-b3) Frequency-domain fluorescence lifetime imaging microscopy (FD-FLIM) of EB-NS solution drop-casted on a glass coverslip. (b1) Intensity image of an EB-NS. (b2) Frequency-domain FLIM image of the same region as in (b1), but with a color-coding that shows two sub-populations of different lifetime. (b3) Corresponding phasor plot highlighting the two populations and the color-coding in (b2). Species with longer lifetime appear in a green color and the ones with the shorter lifetime appear in a red color. (c1) Intensity image of the border of stripes made from EB-NS and HP-NS. (c2) FLIM image of the same region as in (c1), but with a color-coding that shows the different NS according to their lifetime values. (c3) Phasor plot highlighting the color-coding of the lifetimes in (c2): EB-NS (longer lifetimes, green color) and HP-NS (shorter lifetimes, red). Scale bar is 5 μm. The figure was adapted from ref. [91].

above (Figure 6.2 a1-a3). The lifetime of drop-casted EB-NS was measured in a homogeneous layer on top of a glass coverslip. Then, we proceeded with imaging of samples with non-homogeneous layers of all NS types. The obtained average lifetimes of the nanosheets were: 17.6±2.4 μs, 7.8±1.5 μs and 4.5±0.7 μs for EB-NS, HB-NS and HP-NS, respectively. Moreover, we noticed that for each NS type, aggregates and bulky particles with bigger size exhibit significantly different lifetimes (Figure 6.2 b1-b3). Because of the difference in lifetime values of EB-NS and HP-NS, we can identify the NS type (border) based on a lifetime image of a region with both EB-NS and HP-NS (Figure 6.2 c1-c3). By looking at the intensity image alone, it was not possible to identify the border between EB-NS and HP-NS (Figure 6.2 c1). Technically, the identification was performed by using phasor plot data representation. A phasor plot represents frequency-domain lifetime data using the measured phase angle (ϕ) and the modulation ratio (M). For the specific image, phasor plot allows to separate between two sub-populations of NS (green and red ovals in Figure 6.2 c3). Then, I applied the same lifetime separation to the FLIM image (Figure 6.2 c2).

In summary, I used the fluorescence lifetime spectroscopy to characterize three types of silicate nanosheets. I found that the fluorescence lifetimes of nanosheets is shorter, as compared to bulk material. This result indicates that the lifetimes of these nanomaterials carry potential for lifetime-encoded imaging. Furthermore, the measured difference in fluorescence lifetimes of EB-NS, HB-NS and HP-NS can be used for multiplexed imaging.

BIBLIOGRAPHY

[1] Partha Pratim Mondal and Alberto Diaspro. *Fundamentals of fluorescence microscopy: Exploring life with light*. Dordrecht: Springer, 2014. ISBN: 9789400775459.

[2] T. A. Klar and S. W. Hell. "Subdiffraction resolution in far-field fluorescence microscopy." In: *Optics letters* 24.14 (1999), pp. 954–956. DOI: `10.1364/ol.24.000954`.

[3] R. M. Dickson, A. B. Cubitt, R. Y. Tsien, and W. E. Moerner. "On/off blinking and switching behaviour of single molecules of green fluorescent protein." In: *Nature* 388.6640 (1997), pp. 355–358. ISSN: 0028-0836. DOI: `10.1038/41048`.

[4] Eric Betzig, George H. Patterson, Rachid Sougrat, O. Wolf Lindwasser, Scott Olenych, Juan S. Bonifacino, Michael W. Davidson, Jennifer Lippincott-Schwartz, and Harald F. Hess. "Imaging intracellular fluorescent proteins at nanometer resolution." In: *Science (New York, N.Y.)* 313.5793 (2006), pp. 1642–1645. DOI: `10.1126/science.1127344`. URL: `https://science.sciencemag.org/content/313/5793/1642`.

[5] Rainer Pepperkok and Jan Ellenberg. "High-throughput fluorescence microscopy for systems biology." In: *Nature reviews. Molecular cell biology* 7.9 (2006), pp. 690–696. ISSN: 1471-0072. DOI: `10.1038/nrm1979`.

[6] Ralf Jungmann, Maier S. Avendaño, Johannes B. Woehrstein, Mingjie Dai, William M. Shih, and Peng Yin. "Multiplexed 3D cellular super-resolution imaging with DNA-PAINT and Exchange-PAINT." In: *Nature methods* 11.3 (2014), pp. 313–318. DOI: `10.1038/nmeth.2835`.

[7] Theodorus W.J. Gadella, Thomas M. Jovin, and Robert M. Clegg. "Fluorescence lifetime imaging microscopy (FLIM): Spatial resolution of microstructures on the nanosecond time scale." In: *Biophysical Chemistry* 48.2 (1993), pp. 221–239. ISSN: 03014622. DOI: `10.1016/0301-4622(93)85012-7`. URL: `https://www.sciencedirect.com/science/article/pii/0301462293850127`.

[8] Klaus Suhling et al. "Fluorescence lifetime imaging (FLIM): Basic concepts and some recent developments." In: *Medical Photonics* 27 (2015), pp. 3–40. ISSN: 22138846. DOI: `10.1016/j.medpho.2014.12.001`. URL: `https://www.sciencedirect.com/science/article/pii/S2213884614000033`.

[9] Joseph R. Lakowicz and Klaus W. Berndt. "Lifetime–selective fluorescence imaging using an rf phase–sensitive camera." In: *Review of Scientific Instruments* 62.7 (1991), pp. 1727–1734. ISSN: 0034-6748. DOI: `10.1063/1.1142413`. URL: `https://aip.scitation.org/doi/10.1063/1.1142413`.

[10] David W. Piston and Gert-Jan Kremers. "Fluorescent protein FRET: the good, the bad and the ugly." In: *Trends in biochemical sciences* 32.9 (2007), pp. 407–414. ISSN: 0968-0004. DOI: `10.1016/j.tibs.2007.08.003`. URL: `https://www.cell.com/trends/biochemical-sciences/fulltext/S0968-0004(07)00191-0?_returnURL=https%3A%2F%2Flinkinghub.elsevier.com%2Fretrieve%2Fpii%2FS0968000407001910%3Fshowall%3Dtrue`.

[11] Luís M. S. Loura and Manuel Prieto. "FRET in Membrane Biophysics: An Overview." In: *Frontiers in physiology* 2 (2011), p. 82. DOI: `10.3389/fphys.2011.00082`.

[12] Desmond O'Connor. *Time-correlated single photon counting*. Saint Louis: Elsevier Science, 2014. ISBN: 9780323141444.

[13] E. Gratton, D. M. Jameson, and R. D. Hall. "Multifrequency phase and modulation fluorometry." In: *Annual review of biophysics and bioengineering* 13 (1984), pp. 105–124. ISSN: 0084-6589. DOI: `10.1146/annurev.bb.13.060184.000541`.

[14] Geert Ide, Yves Engelborghs, and Andre Persoons. "Fluorescence lifetime resolution with phase fluorometry." In: *Review of Scientific Instruments* 54.7 (1983), pp. 841–844. ISSN: 0034-6748. DOI: `10.1063/1.1137488`. URL: `https://aip.scitation.org/doi/10.1063/1.1137488`.

[15] Adam J. Bowman, Brannon B. Klopfer, Thomas Juffmann, and Mark A. Kasevich. "Electro-optic imaging enables efficient wide-field fluorescence lifetime microscopy." In: *Nature communications* 10.1 (2019), p. 4561. DOI: `10.1038/s41467-019-12535-5`. URL: `https://www.nature.com/articles/s41467-019-12535-5`.

[16] X. Michalet, O. H. W. Siegmund, J. V. Vallerga, P. Jelinsky, J. E. Millaud, and S. Weiss. "Photon-Counting H33D Detector for Biological Fluorescence Imaging." In: *Nuclear instruments & methods in physics research. Section A, Accelerators, spectrometers, detectors and associated equipment* 567.1 (2006), p. 133. ISSN: 0168-9002. DOI: `10.1016/j.nima.2006.05.155`.

[17] Arin Ulku, Andrei Ardelean, Michel Antolovic, Shimon Weiss, Edoardo Charbon, Claudio Bruschini, and Xavier Michalet. "Wide-field time-gated SPAD imager for phasor-based FLIM applications." In: *Methods and applications in fluorescence* 8.2 (2020), p. 024002. DOI: `10.1088/2050-6120/ab6ed7`. URL: `https://iopscience.iop.org/article/10.1088/2050-6120/ab6ed7`.

[18] Sebastian Isbaner, Narain Karedla, Daja Ruhlandt, Simon Christoph Stein, Anna Chizhik, Ingo Gregor, and Jörg Enderlein. "Dead-time correction of fluorescence lifetime measurements and fluorescence lifetime imaging." In: *Optics express* 24.9 (2016), pp. 9429–9445. DOI: `10.1364/OE.24.009429`.

[19] Michael Wahl. "Modern TCSPC Electronics: Principles and Acquisition Modes." In: *Advanced Photon Counting*. Ed. by Peter Kapusta, Michael Wahl, and Rainer Erdmann. Vol. 15. Springer Series on Fluorescence. Cham: Springer International Publishing, 2015, pp. 1–21. ISBN: 978-3-319-15635-4. DOI: `10.1007/4243{\textunderscore}2014{\textunderscore}62`.

[20] Henryk Szmacinski, Joseph R. Lakowicz, and Michael L. Johnson. "[30] Fluorescence lifetime imaging microscopy: Homodyne technique using high-speed gated image intensifier." In: *Methods in enzymology* 240 (1994), pp. 723–748. ISSN: 0076-6879. DOI: `10.1016/s0076-6879(94)40069-5`.

[21] Klaus C. Schuermann and Hernán E. Grecco. "flatFLIM: enhancing the dynamic range of frequency domain FLIM." In: *Optics express* 20.18 (2012), pp. 20730–20741. DOI: `10.1364/OE.20.020730`. URL: `https://www.osapublishing.org/oe/fulltext.cfm?uri=oe-20-18-20730&id=240954`.

[22] Daniel C. Pease. *Histological Techniques for Electron Microscopy*. 2nd ed. Saint Louis: Elsevier Science, 2014. ISBN: 9781483263687.

[23] M. Girbradt. "Geoffrey A. Meek, Practical Electron Microscopy for Biologists. 498 S., 176 Abb. London-New York-Sydney-Toronto 1970: Wiley-Interscience 150 s." In: *Zeitschrift für allgemeine Mikrobiologie* 11.3 (1971), p. 259. ISSN: 00442208. DOI: `10.1002/jobm.19710110322`.

[24] M. G. Gustafsson. "Surpassing the lateral resolution limit by a factor of two using structured illumination microscopy." In: *Journal of microscopy* 198.Pt 2 (2000), pp. 82–87. ISSN: 0022-2720. DOI: `10.1046/j.1365-2818.2000.00710.x`. URL: `https://onlinelibrary.wiley.com/doi/full/10.1046/j.1365-2818.2000.00710.x`.

[25] Mats G. L. Gustafsson, Lin Shao, Peter M. Carlton, C. J. Rachel Wang, Inna N. Golubovskaya, W. Zacheus Cande, David A. Agard, and John W. Sedat. "Three-dimensional resolution doubling in wide-field fluorescence microscopy by structured illumination." In: *Biophysical Journal* 94.12 (2008), pp. 4957–4970. ISSN: 00063495. DOI: `10.1529/biophysj.107.120345`. URL: `https://pubmed.ncbi.nlm.nih.gov/18326650/`.

[26] E. H. Rego, L. Shao, J. J. Macklin, L. Winoto, G. A. Johansson, N. Kamps-Hughes, M. W. Davidson, and M. G. L. Gustafsson. "Nonlinear structured-illumination microscopy with a photo-

switchable protein reveals cellular structures at 50-nm resolution." In: *Proceedings of the National Academy of Sciences* 109.3 (2012), E135–E143. ISSN: 0027-8424. DOI: 10.1073/pnas.1107547108. URL: https://www.pnas.org/content/109/3/E135.

[27] Lin Shao, Peter Kner, E. Hesper Rego, and Mats G. L. Gustafsson. "Super-resolution 3D microscopy of live whole cells using structured illumination." In: *Nature methods* 8.12 (2011), pp. 1044–1046. DOI: 10.1038/nmeth.1734. URL: https://pubmed.ncbi.nlm.nih.gov/22002026/.

[28] Reto Fiolka, Lin Shao, E. Hesper Rego, Michael W. Davidson, and Mats G. L. Gustafsson. "Time-lapse two-color 3D imaging of live cells with doubled resolution using structured illumination." In: *Proceedings of the National Academy of Sciences of the United States of America* 109.14 (2012), pp. 5311–5315. DOI: 10.1073/pnas.1119262109. URL: https://www.pnas.org/content/109/14/5311.

[29] C. J. R. SHEPPARD. "Super-resolution in confocal imaging." In: *Optik (Stuttgart)* 80.2 (1988), 53–54UR –https://pascal–francis.inist.fr/vibad/index.ph
ISSN: 0030-4026.

[30] Claus B. Müller and Jörg Enderlein. "Image scanning microscopy." In: *Physical review letters* 104.19 (2010), p. 198101. DOI: 10.1103/PhysRevLett.104.198101.

[31] Olaf Schulz, Christoph Pieper, Michaela Clever, Janine Pfaff, Aike Ruhlandt, Ralph H. Kehlenbach, Fred S. Wouters, Jörg Großhans, Gertrude Bunt, and Jörg Enderlein. "Resolution doubling in fluorescence microscopy with confocal spinning-disk image scanning microscopy." In: *Proceedings of the National Academy of Sciences of the United States of America* 110.52 (2013), pp. 21000–21005. DOI: 10.1073/pnas.1315858110. URL: https://www.pnas.org/content/110/52/21000.

[32] L. H. SCHAEFER, D. SCHUSTER, and J. SCHAFFER. "Structured illumination microscopy: artefact analysis and reduction utilizing a parameter optimization approach." In: *Journal of microscopy* 216.2 (2004), pp. 165–174. ISSN: 0022-2720. DOI: 10.1111/j.0022-2720.2004.01411.x.

[33] Dominik Wildanger et al. "Solid immersion facilitates fluorescence microscopy with nanometer resolution and sub-ångström emitter localization." In: *Advanced materials (Deerfield Beach, Fla.)* 24.44 (2012), OP309–13. DOI: 10.1002/adma.201203033.

[34] Eva Wegel, Antonia Göhler, B. Christoffer Lagerholm, Alan Wainman, Stephan Uphoff, Rainer Kaufmann, and Ian M. Dobbie. "Imaging cellular structures in super-resolution with SIM, STED and Localisation Microscopy: A practical comparison." In: *Scientific Reports* 6.1 (), pp. 1–13. ISSN: 2045-2322. DOI: 10.

1038/srep27290. URL: https://www.nature.com/articles/srep27290.

[35] J. Vangindertael, R. Camacho, W. Sempels, H. Mizuno, P. Dedecker, and K. P. F. Janssen. "An introduction to optical super-resolution microscopy for the adventurous biologist." In: *Methods and Applications in Fluorescence* 6.2 (2018), p. 022003. DOI: 10.1088/2050-6120/aaae0c. URL: https://pubmed.ncbi.nlm.nih.gov/29422456/.

[36] Michael J. Rust, Mark Bates, and Xiaowei Zhuang. "Sub-diffraction-limit imaging by stochastic optical reconstruction microscopy (STORM)." In: *Nature methods* 3.10 (2006), pp. 793–795. DOI: 10.1038/nmeth929.

[37] Kim I. Mortensen, L. Stirling Churchman, James A. Spudich, and Henrik Flyvbjerg. "Optimized localization analysis for single-molecule tracking and super-resolution microscopy." In: *Nature Methods* 7.5 (2010), pp. 377–381. ISSN: 1548-7091. DOI: 10.1038/nmeth.1447.

[38] Francisco Balzarotti, Yvan Eilers, Klaus C. Gwosch, Arvid H. Gynnå, Volker Westphal, Fernando D. Stefani, Johan Elf, and Stefan W. Hell. "Nanometer resolution imaging and tracking of fluorescent molecules with minimal photon fluxes." In: *Science (New York, N.Y.)* 355.6325 (2017), pp. 606–612. DOI: 10.1126/science.aak9913.

[39] Luciano A. Masullo, Florian Steiner, Jonas Zähringer, Lucía F. Lopez, Johann Bohlen, Lars Richter, Fiona Cole, Philip Tinnefeld, and Fernando D. Stefani. "Pulsed Interleaved MINFLUX." In: *Nano Letters* 21.1 (2021), pp. 840–846. ISSN: 1530-6984. DOI: 10.1021/acs.nanolett.0c04600.

[40] Alexey Sharonov and Robin M. Hochstrasser. "Wide-field subdiffraction imaging by accumulated binding of diffusing probes." In: *Proceedings of the National Academy of Sciences of the United States of America* 103.50 (2006), pp. 18911–18916. DOI: 10.1073/pnas.0609643104. URL: https://www.pnas.org/content/103/50/18911.

[41] Ralf Jungmann, Christian Steinhauer, Max Scheible, Anton Kuzyk, Philip Tinnefeld, and Friedrich C. Simmel. "Single-Molecule Kinetics and Super-Resolution Microscopy by Fluorescence Imaging of Transient Binding on DNA Origami." In: *Nano Letters* 10.11 (2010), pp. 4756–4761. ISSN: 1530-6984. DOI: 10.1021/nl103427w. URL: https://pubmed.ncbi.nlm.nih.gov/20957983/.

[42] Joerg Schnitzbauer, Maximilian T Strauss, Thomas Schlichthaerle, Florian Schueder, and Ralf Jungmann. "Super-resolution microscopy with DNA-PAINT." In: *Nature Protocols* 12.6 (2017), pp. 1198–1228. ISSN: 1750-2799. DOI: 10.1038/nprot.2017.024.

[43] Sebastian Strauss and Ralf Jungmann. "Up to 100-fold speed-up and multiplexing in optimized DNA-PAINT." In: *Nature Methods* 17.8 (2020), pp. 789–791. ISSN: 1548-7091. DOI: 10.1038/s41592-020-0869-x.

[44] Fehmi Civitci et al. "Fast and multiplexed superresolution imaging with DNA-PAINT-ERS." In: *Nature communications* 11.1 (2020), p. 4339. DOI: 10.1038/s41467-020-18181-6. URL: https://www.nature.com/articles/s41467-020-18181-6.

[45] Florian Schueder, Juanita Lara-Gutiérrez, Brian J. Beliveau, Sinem K. Saka, Hiroshi M. Sasaki, Johannes B. Woehrstein, Maximilian T. Strauss, Heinrich Grabmayr, Peng Yin, and Ralf Jungmann. "Multiplexed 3D super-resolution imaging of whole cells using spinning disk confocal microscopy and DNA-PAINT." In: *Nature Communications* 8.1 (2017), pp. 1–9. DOI: 10.1038/s41467-017-02028-8. URL: https://www.nature.com/articles/s41467-017-02028-8.

[46] Edward C. Stack, Chichung Wang, Kristin A. Roman, and Clifford C. Hoyt. "Multiplexed immunohistochemistry, imaging, and quantitation: a review, with an assessment of Tyramide signal amplification, multispectral imaging and multiplex analysis." In: *Methods (San Diego, Calif.)* 70.1 (2014), pp. 46–58. DOI: 10.1016/j.ymeth.2014.08.016.

[47] Maureen A. Walling, Jennifer A. Novak, and Jason R. E. Shepard. "Quantum dots for live cell and in vivo imaging." In: *International journal of molecular sciences* 10.2 (2009), pp. 441–491. DOI: 10.3390/ijms10020441. URL: https://pubmed.ncbi.nlm.nih.gov/19333416/.

[48] J. R. Mansfield. "Multispectral imaging: a review of its technical aspects and applications in anatomic pathology." In: *Veterinary pathology* 51.1 (2014), pp. 185–210. DOI: 10.1177/0300985813506918.

[49] M. E. Dickinson, G. Bearman, S. Tille, R. Lansford, and S. E. Fraser. "Multi-spectral imaging and linear unmixing add a whole new dimension to laser scanning fluorescence microscopy." In: *BioTechniques* 31.6 (2001), pp. 1272, 1274–6, 1278. ISSN: 0736-6205. DOI: 10.2144/01316bt01.

[50] Franziska R. Winter, Maria Loidolt, Volker Westphal, Alexey N. Butkevich, Carola Gregor, Steffen J. Sahl, and Stefan W. Hell. "Multicolour nanoscopy of fixed and living cells with a single STED beam and hyperspectral detection." In: *Scientific reports* 7.1 (2017), p. 46492. DOI: 10.1038/srep46492. URL: https://www.nature.com/articles/srep46492.

[51] Graham T. Dempsey, Joshua C. Vaughan, Kok Hao Chen, Mark Bates, and Xiaowei Zhuang. "Evaluation of fluorophores for optimal performance in localization-based super-resolution imag-

ing." In: *Nature methods* 8.12 (2011), pp. 1027–1036. DOI: `10.1038/nmeth.1768`.

[52] Mark Bates, Graham T. Dempsey, Kok Hao Chen, and Xiaowei Zhuang. "Multicolor super-resolution fluorescence imaging via multi-parameter fluorophore detection." In: *Chemphyschem : a European journal of chemical physics and physical chemistry* 13.1 (2012), pp. 99–107. DOI: `10.1002/cphc.201100735`. URL: `https://chemistry-europe.onlinelibrary.wiley.com/doi/full/10.1002/cphc.201100735`.

[53] Pablo A. Gómez-García, Erik T. Garbacik, Jason J. Otterstrom, Maria F. Garcia-Parajo, and Melike Lakadamyali. "Excitation-multiplexed multicolor superresolution imaging with fm-STORM and fm-DNA-PAINT." In: *Proceedings of the National Academy of Sciences of the United States of America* 115.51 (2018), pp. 12991–12996. DOI: `10.1073/pnas.1804725115`.

[54] Pedro Almada et al. "Automating multimodal microscopy with NanoJ-Fluidics." In: *Nature communications* 10.1 (2019), p. 1223. DOI: `10.1038/s41467-019-09231-9`. URL: `https://www.nature.com/articles/s41467-019-09231-9`.

[55] Maja Klevanski, Frank Herrmannsdoerfer, Steffen Sass, Varun Venkataramani, Mike Heilemann, and Thomas Kuner. "Automated highly multiplexed super-resolution imaging of protein nano-architecture in cells and tissues." In: *Nature communications* 11.1 (2020), p. 1552. DOI: `10.1038/s41467-020-15362-1`. URL: `https://www.nature.com/articles/s41467-020-15362-1`.

[56] Florian Schueder, Johannes Stein, Florian Stehr, Alexander Auer, Bianca Sperl, Maximilian T. Strauss, Petra Schwille, and Ralf Jungmann. *An order of magnitude faster DNA-PAINT imaging by optimized sequence design and buffer conditions*. 2019. URL: `https://www.nature.com/articles/s41592-019-0584-7`.

[57] Orsolya K. Wade et al. "124-Color Super-resolution Imaging by Engineering DNA-PAINT Blinking Kinetics." In: *Nano letters* 19.4 (2019), pp. 2641–2646. DOI: `10.1021/acs.nanolett.9b00508`.

[58] Philip Tinnefeld, Volker Buschmann, Dirk–Peter Herten, Kyung–Tae Han, and Markus Sauer. "Confocal Fluorescence Lifetime Imaging Microscopy (FLIM) at the Single Molecule Level." In: *Single Molecules* 1.3 (2000), pp. 215–223. ISSN: 1438-5171. DOI: `10.1002/1438-5171(200009)1:3{\textless}215::AID-SIMO215{\textgreater}3.0.CO;2-S`.

[59] Bo Huang, Wenqin Wang, Mark Bates, and Xiaowei Zhuang. "Three-dimensional super-resolution imaging by stochastic optical reconstruction microscopy." In: *Science (New York, N.Y.)* 319.5864 (2008), pp. 810–813. DOI: `10.1126/science.1153529`.

[60] Manuel F. Juette, Travis J. Gould, Mark D. Lessard, Michael J. Mlodzianoski, Bhupendra S. Nagpure, Brian T. Bennett, Samuel T. Hess, and Joerg Bewersdorf. "Three-dimensional sub-100 nm resolution fluorescence microscopy of thick samples." In: *Nature methods* 5.6 (2008), pp. 527–529. DOI: `10.1038/nmeth.1211`.

[61] Gleb Shtengel et al. "Interferometric fluorescent super-resolution microscopy resolves 3D cellular ultrastructure." In: *Proceedings of the National Academy of Sciences of the United States of America* 106.9 (2009), pp. 3125–3130. DOI: `10.1073/pnas.0813131106`.

[62] Roman Schmidt, Christian A. Wurm, Stefan Jakobs, Johann Engelhardt, Alexander Egner, and Stefan W. Hell. "Spherical nanosized focal spot unravels the interior of cells." In: *Nature methods* 5.6 (2008), pp. 539–544. DOI: `10.1038/nmeth.1214`.

[63] B. P. Olveczky, N. Periasamy, and A. S. Verkman. "Mapping fluorophore distributions in three dimensions by quantitative multiple angle-total internal reflection fluorescence microscopy." In: *Biophysical Journal* 73.5 (1997), pp. 2836–2847. ISSN: 00063495. DOI: `10.1016/S0006-3495(97)78312-7`.

[64] Thomas Ruckstuhl and Dorinel Verdes. "Supercritical angle fluorescence (SAF) microscopy." In: *Optics express* 12.18 (2004), pp. 4246–4254. DOI: `10.1364/opex.12.004246`.

[65] Siddharth Sivankutty, Thomas Barroca, Céline Mayet, Guillaume Dupuis, Emmanuel Fort, and Sandrine Lévêque-Fort. "Confocal supercritical angle microscopy for cell membrane imaging." In: *Optics letters* 39.3 (2014), pp. 555–558. DOI: `10.1364/OL.39.000555`.

[66] Michael A. Partridge and Eugene E. Marcantonio. "Initiation of attachment and generation of mature focal adhesions by integrin-containing filopodia in cell spreading." In: *Molecular biology of the cell* 17.10 (2006), pp. 4237–4248. ISSN: 1059-1524. DOI: `10.1091/mbc.e06-06-0496`.

[67] Marcelina Cardoso Dos Santos, Régis Déturche, Cyrille Vézy, and Rodolphe Jaffiol. "Topography of Cells Revealed by Variable-Angle Total Internal Reflection Fluorescence Microscopy." In: *Biophysical Journal* 111.6 (2016), pp. 1316–1327. ISSN: 00063495. DOI: `10.1016/j.bpj.2016.06.043`.

[68] Dinah Loerke, Walter Stühmer, and Martin Oheim. "Quantifying axial secretory-granule motion with variable-angle evanescent-field excitation." In: *Journal of Neuroscience Methods* 119.1 (2002), pp. 65–73. ISSN: 01650270. DOI: `10.1016/S0165-0270(02)00178-4`.

[69] N. Bourg, C. Mayet, G. Dupuis, T. Barroca, P. Bon, S. Lécart, E. Fort, and S. Lévêque-Fort. "Direct optical nanoscopy with axially localized detection." In: *Nature Photonics* 9.9 (2015), pp. 587–593. ISSN: 1749-4885. DOI: 10.1038/nphoton.2015.132.

[70] Alexey I. Chizhik, Jan Rother, Ingo Gregor, Andreas Janshoff, and Jörg Enderlein. "Metal-induced energy transfer for live cell nanoscopy." In: *Nature Photonics* 8.2 (2014), pp. 124–127. ISSN: 1749-4885. DOI: 10.1038/nphoton.2013.345.

[71] Narain Karedla, Alexey I. Chizhik, Ingo Gregor, Anna M. Chizhik, Olaf Schulz, and Jörg Enderlein. "Single-molecule metal-induced energy transfer (smMIET): resolving nanometer distances at the single-molecule level." In: *Chemphyschem : a European journal of chemical physics and physical chemistry* 15.4 (2014), pp. 705–711. DOI: 10.1002/cphc.201300760.

[72] R. R. Chance, A. H. Miller, A. Prock, and R. Silbey. "Fluorescence and energy transfer near interfaces: The complete and quantitative description of the Eu +3 /mirror systems." In: *The Journal of Chemical Physics* 63.4 (1975), pp. 1589–1595. ISSN: 0021-9606. DOI: 10.1063/1.431483.

[73] Anna M. Chizhik, Carina Wollnik, Daja Ruhlandt, Narain Karedla, Alexey I. Chizhik, Lara Hauke, Dirk Hähnel, Ingo Gregor, Jörg Enderlein, and Florian Rehfeldt. "Dual-color metal-induced and Förster resonance energy transfer for cell nanoscopy." In: *Molecular Biology of the Cell* 29.7 (2018), pp. 846–851. ISSN: 1059-1524. DOI: 10.1091/mbc.E17-05-0314. URL: https://pubmed.ncbi.nlm.nih.gov/29444956/.

[74] Thilo Baronsky et al. "Cell-Substrate Dynamics of the Epithelial-to-Mesenchymal Transition." In: *Nano letters* 17.5 (2017), pp. 3320–3326. DOI: 10.1021/acs.nanolett.7b01558.

[75] Anna M. Chizhik, Daja Ruhlandt, Janine Pfaff, Narain Karedla, Alexey I. Chizhik, Ingo Gregor, Ralph H. Kehlenbach, and Jörg Enderlein. "Three-Dimensional Reconstruction of Nuclear Envelope Architecture Using Dual-Color Metal-Induced Energy Transfer Imaging." In: *ACS nano* 11.12 (2017), pp. 11839–11846. DOI: 10.1021/acsnano.7b04671.

[76] Sebastian Isbaner et al. "Axial Colocalization of Single Molecules with Nanometer Accuracy Using Metal-Induced Energy Transfer." In: *Nano letters* 18.4 (2018), pp. 2616–2622. DOI: 10.1021/acs.nanolett.8b00425.

[77] Arindam Ghosh, Akshita Sharma, Alexey I. Chizhik, Sebastian Isbaner, Daja Ruhlandt, Roman Tsukanov, Ingo Gregor, Narain Karedla, and Jörg Enderlein. "Graphene-based metal-induced energy transfer for sub-nanometre optical localization." In: *Na-*

ture Photonics 13.12 (2019), pp. 860–865. ISSN: 1749-4885. DOI: 10.1038/s41566-019-0510-7.

[78] Y. Prokazov, E. Turbin, A. Weber, R. Hartig, and W. Zuschratter. "Position sensitive detector for fluorescence lifetime imaging." In: *Journal of Instrumentation* 9.12 (2014), p. C12015.

[79] Nazar Oleksiievets, Jan Christoph Thiele, André Weber, Ingo Gregor, Oleksii Nevskyi, Sebastian Isbaner, Roman Tsukanov, and Jörg Enderlein. "Wide-Field Fluorescence Lifetime Imaging of Single Molecules." In: *The Journal of Physical Chemistry A* 124.17 (2020), pp. 3494–3500. ISSN: 1089-5639. DOI: 10.1021/acs.jpca.0c01513.

[80] Jan Christoph Thiele, Dominic A. Helmerich, Nazar Oleksiievets, Roman Tsukanov, Eugenia Butkevich, Markus Sauer, Oleksii Nevskyi, and Jörg Enderlein. "Confocal Fluorescence-Lifetime Single-Molecule Localization Microscopy." In: *ACS Nano* 14.10 (2020). PMID: 33035050, pp. 14190–14200. DOI: 10.1021/acsnano.0c07322. eprint: https://doi.org/10.1021/acsnano.0c07322. URL: https://doi.org/10.1021/acsnano.0c07322.

[81] Alex M. Valm, Sarah Cohen, Wesley R. Legant, Justin Melunis, Uri Hershberg, Eric Wait, Andrew R. Cohen, Michael W. Davidson, Eric Betzig, and Jennifer Lippincott-Schwartz. "Applying systems-level spectral imaging and analysis to reveal the organelle interactome." In: *Nature* 546.7656 (2017), pp. 162–167.

[82] Thomas Niehörster, Anna Löschberger, Ingo Gregor, Benedikt Krämer, Hans-Jürgen Rahn, Matthias Patting, Felix Koberling, Jörg Enderlein, and Markus Sauer. "Multi-target spectrally resolved fluorescence lifetime imaging microscopy." In: *Nature Methods* 13 (2016), pp. 257–262.

[83] Felipe Opazo, Matthew Levy, Michelle Byrom, Christina Schäfer, Claudia Geisler, Teja W. Groemer, Andrew D. Ellington, and Silvio O. Rizzoli. "Aptamers as potential tools for super-resolution microscopy." In: *Nature Methods* 9.10 (2012), pp. 938–939.

[84] Sebastian Strauss, Philipp C. Nickels, Maximilian T. Strauss, Vilma Jimenez Sabinina, Jan Ellenberg, Jeffrey D. Carter, Shashi Gupta, Nebojsa Janjic, and Ralf Jungmann. "Modified aptamers enable quantitative sub-10-nm cellular DNA-PAINT imaging." In: *Nature Methods* 15 (2018), pp. 685–688.

[85] Thomas Schlichthaerle, Alexandra S. Eklund, Florian Schueder, Maximilian T. Strauss, Christian Tiede, Alistair Curd, Jonas Ries, Michelle Peckham, Darren C Tomlinson, and Ralf Jungmann. "Site-Specific Labeling of Affimers for DNA-PAINT Microscopy." In: *Angewandte Chemie* 57 (2018), pp. 11060–11063.

[86] Thomas Schlichthaerle, Mahipal Ganji, Alexander Auer, Orsolya Kimbu Wade, and Ralf Jungmann. "Bacterially Derived Antibody Binders as Small Adapters for DNA-PAINT Microscopy." In: *ChemBioChem* 20 (2019), pp. 1032–1038.

[87] Shama Sograte-Idrissi, Nazar Oleksiievets, Sebastian Isbaner, Mariana Eggert-Martinez, Jörg Enderlein, Roman Tsukanov, and Felipe Opazo. "Nanobody Detection of Standard Fluorescent Proteins Enables Multi-Target DNA-PAINT with High Resolution and Minimal Displacement Errors." In: *Cells* 8.1 (2019).

[88] S.S. Agasti, Y. Wang, F. Schueder, A. Sukumar, R. Jungmann, and P. Yin. "DNA-barcoded labeling probes for highly multiplexed Exchange-PAINT imaging." In: *Chemical Science* 8 (2017), pp. 3080–3091.

[89] Jan Christoph Thiele, Dominic A. Helmerich, Nazar Oleksiievets, Roman Tsukanov, Eugenia Butkevich, Markus Sauer, Oleksii Nevskyi, and Jörg Enderlein. "Confocal Fluorescence-Lifetime Single-Molecule Localization Microscopy." In: *ACS Nano* 14.10 (2020), pp. 14190–14200. DOI: `10.1021/acsnano.0c07322`.

[90] M. Ovesný, P. Křížek, J. Borkovec, Z. Švindrych, and G. M. Hagen. "Thunderstorm: A Comprehensive Imagej Plugin for PALM and STORM Data Analysis and Super-Resolution Imaging." In: *Bioinformatics* 30 (2014), pp. 2389–2390.

[91] Gabriele Selvaggio, Milan Weitzel, Nazar Oleksiievets, Tabea A. Oswald, Robert Nißler, Ingo Mey, Volker Karius, Jörg Enderlein, Roman Tsukanov, and Sebastian Kruss. *Exfoliation and Optical Properties of Near-Infrared Fluorescent Silicate Nanosheets*. 2021. DOI: `10.26434/chemrxiv.13350728.v1`.